Semi-Solid Processing of Hypereutectic Aluminum-Silicon Alloys

by

Ittipon Diewwanit

B.Eng., Metallurgical Engineering (1990)
Chulalongkorn University, Thailand

Submitted to the Department of Materials Science and Engineering
in Partial Fulfillment of the Requirements for the Degree of

Doctor of Science in Metallurgy

at the
Massachusetts Institute of Technology

June 1996

Signature of Author .....
Department of Materials Science and Engineering
May 3, 1996

Certified by .....
Merton C. Flemings
Toyota Professor of Materials Processing
Thesis Supervisor

Accepted by .....
Michael F. Rubner
TDK Professor of Materials Science and Engineering
Chair, Departmental Committee on Graduate Students

Semi-Solid Processing of Hypereutectic Aluminum-Silicon Alloys

by

Ittipon Diewwanit

Submitted to the Department of Materials Science and Engineering
on May 3, 1996 in partial fulfillment of the requirements for the
degree of Doctor of Science in Metallurgy

ABSTRACT

Apparent viscosity of semi-solid hypereutectic aluminum-silicon alloys with silicon contents of 30, 40, and 50 wt.% was measured as the melt was continuously cooled from the liquid state. The viscosity of the slurries depended on shear rate and volume fraction solid. At a given volume fraction solid above 0.1 the slurries exhibited pseudoplasticity (shear-thinning). An empirical expression of the form:

$$\eta = A' \exp(B'' g_s) \dot{\gamma}^{(a+B' g_s)}$$

which relates the apparent viscosity to $\dot{\gamma}$, the shear rate, and g_s, the volume fraction solid, fits the experimental data very closely. In the shear rate range from 35 to 500 s^{-1} the continuous cooling viscosity was of the same order of magnitude as that of non-dendritic semi-solid metals. Primary silicon particle size in sheared samples was found to be smaller than in absence of shearing, but shearing above 100 s^{-1} had an insignificant effect on particle size. Silicon particle agglomeration, analogous to that operating in non-dendritic semi-solid slurries, was also observed.

In the second part of the study rheocast ingots of the same alloys were produced in a batch rheocasting apparatus. The cohesive network of primary silicon was broken down by agitation and the particle size was found to be much smaller than that of the samples solidified in absence of agitation. The deformation behavior of reheated rheocast ingots and ingots cast in absence of agitation were investigated by two constant force techniques: a cone penetration test and a compression test between two parallel plates. Reheated semi-solid rheocast ingots exhibited lower apparent yield strength than semi-solid ingots conventionally solidified without agitation. The resistance to deformation of the latter was so high that they could not be compressed between two parallel plates with a stress in the range of 5 to 175 kPa employed in the present work. Semi-solid rheocast Al-40 wt.% Si ingots deformed continuously under an initial stress exceeding about 40 kPa. and in a discontinuous fashion for a lower initial stress.

Thesis Supervisor: Merton C. Flemings

Title: Toyota Professor of Materials Processing

TABLE OF CONTENTS

LIST OF FIGURES

LIST OF TABLES

ACKNOWLEDGMENTS

I would like to express my sincerest thanks to the thesis supervisor, Prof. Merton C. Flemings, for the education and support and also the thesis committee, Prof. Yet-Ming Chiang and Prof. Uday B. Pal for their comments and suggestions.

I am grateful to the all members of solidification group at MIT especially Günter Arndt, Dr. Anacleto de Figueredo, Maria Due, Prof. Theo Kattamis, Prof. Su-Jien Lin, John Matz, Dr. Thomas J. Piccone, Stacey Rochford, Dr. Stian Sannes, Kazuaki Sato, Yusuf Sumartha, Peter Ragone, Dr. Yan-zong Wu, and Yin-Lin Xie.

I also would like to thank Prof. Paritud Bhandhubanyong and Prof. Wikrom Vajarakupta of Metallurgical Engineering Department, Chulalongkorn University, for their support throughout my academic life. I would like to thank Prof. Mary P. Rowe for her caring advise. Finally, I want to thank my family and Prinyanee Tanametanont for their eternal love and support.

CHAPTER ONE

INTRODUCTION

Hypereutectic Al-Si alloys with a silicon content from 12 up to 25 wt.% have been commercially cast and used in many applications, particularly in the automotive industry. The limit on the silicon content is mainly due to the relatively wide solidification range of these alloys and the size of primary silicon in the castings. There have been many efforts to overcome this barrier, ranging from simply alloying with appropriate elements to developing new processes.

Semi-solid metal processing, invented at MIT in the early 1970's, has been accepted as an economically attractive and powerful alternative to conventional casting. It consists of two steps: thixoforming and rheocasting. During thixoforming reheated semi-solid ingots which exhibit desirable microstructure are shaped into parts. The cost of handling liquid metal thus can be saved and existing forming facilities may be adapted to this process. The ingots, however, must be previously processed through rheocasting in order to generate the appropriate microstructure which allows subsequent thixoforming.

The deformation behavior or rheology of semi-solid metals is the foundation of this processing and lies between those of the solid and the liquid. Knowledge of rheological behavior is necessary to understand and control the process.

The main objectives of this thesis were to investigate:

(a) the rheological properties during, and the feasibility of, rheocasting of hypereutectic Al-Si alloys with silicon contents from 30 to 50 wt.%.

(b) the feasibility of forming the reheated rheocast ingots, as well as ingots initially cast without agitation in the semi-solid state.

(c) the effect of process parameters on cast microstructure of these alloys.

CHAPTER TWO

LITERATURE REVIEW

2.1 Introduction

In this chapter the non-linear behavior of fluids will be introduced first as a guideline. The focus will later be on the rheology of suspension, a system to which semi-solid metal slurries belong. The phenomenological behavior of semi-solids and their microstructural evolution during processing will be reviewed. Some phenomenological and hydrodynamic models describing their behavior will also be included. Although it is not the objective of this thesis to investigate time-dependent rheological properties, the author does include review sections about them for the sake of completeness. The last section is a review of hypereutectic aluminum-silicon alloy production which also includes semi-solid processing and related processes

2.2 Newtonian and Non-Newtonian Fluids

Fluids have been divided into two groups according to their flow characteristics: Newtonian and non-Newtonian. The attempt to characterize the flow behavior of these fluids results in a variety of both theoretical and empirical constitutive equations which assign values to the stress tensor, τ_{ij}, under a certain flow or deformation condition.

A fluid is said to be Newtonian when the constitutive equation describing its flow characteristics is given by:

$$\tau_{ij} = -\mu\dot{\gamma}_{ij} \tag{2.1}$$

A Newtonian fluid exhibits a constant value of viscosity, μ, at a given temperature and pressure. A complete constitutive equation of Newtonian viscosity will be discussed later in section (2.3.7).

Because the relation between the stress tensor, τ_{ij}, and the rate-of-deformation tensor, $\dot{\gamma}_{ij}$, is linear, a fluid which does not behave according to (2.1) is termed non-linear or non-Newtonian. The viscosity of such fluids is not constant and does not have an exact meaning as in the case of a Newtonian fluid. For some fluids which are grouped under the category of generalized Newtonian fluid, there is only a minor modification of the Newtonian model and, with known stress tensor and rate-of-deformation tensor, a scalar quantity termed apparent viscosity, η, is generally accepted as a quantity denoting their flow characteristics. It is given as:

$$\tau_{ij} = -\eta \dot{\gamma}_{ij} \tag{2.2}$$

Although there are various types of behaviors, the deviation from Newtonian behavior can be grouped into four broad categories:

(a) Fluids for which the rate-of-deformation tensor at any point is a function of only one variable: the stress tensor at that point. The fluids in this category are also known as time-independent fluids. There are two types of behavior: shear thinning (pseudoplastic) and shear thickening (dilatant). The apparent viscosity of a pseudoplastic fluid decreases with increasing shear rate, whereas that of a dilatant fluid increases.

(b) Fluids for which the rate-of-deformation tensor at any point is a function of both stress tensor and time. They are also termed time-dependent fluids. Two types of behaviors analogous to (a) are thixotropic and rheopectic. These behaviors will be discussed further in the rheology of suspensions section.

(c) Fluids which exhibit characteristics of both solid and fluid, and recover elastically after deformation. These are termed viscoelastic fluids. Rheology divides viscoelastic fluids into two broad types: linear and non-linear viscoelastic. Although the study of viscoelasticity is the kernel of polymer engineering, it is of very limited use in semi-solid processing of alloy slurries and will not be further discussed.

(d) Fluids which exhibit a yield point. The stress tensor has to exceed a certain amount of value in order to create a measurable deformation. Beyond this yield point, the fluids behave either as in category (a) or (b). Many researchers sometimes prefer to refer to materials which belong to this group as viscoplastic bodies or viscoplastic materials to avoid using the misleading term "fluids." Although the concept of yield stress is, in practice, very useful, its existence has been doubted by the fact that all materials, even rocks, will flow provided that one waits long enough.

2.3 Rheology of Suspensions

Intimate mixtures of coexisting solid and liquid are termed suspensions. The rheological behavior of a suspension depends strongly on properties of both liquid and solid phases. There are many classifications of suspensions. Suspensions of fine solid particles in a liquid are loosely termed as colloids whereas suspensions of larger solid particles are usually subdivided into two large groups: suspensions of non-deformable (rigid) solids and suspensions of deformable solids. Classification according to volume fraction solid of suspensions is sometimes useful when dealing with the interaction between solid particles. A suspension in which a solid particle does not "feel" the presence of other particles is termed "diluted suspension." When the volume fraction solid is high enough, interaction between particles has to be taken into consideration. For the latter case, a suspension is termed "concentrated."

In a particular suspension of solid particles in a Newtonian liquid, the nature of the solid phase greatly contributes to the deviation from the Newtonian behavior. It is generally accepted that there are three kinds of coexisting forces acting on these dispersed solid particles: repulsion-attraction force, Brownian force, and local viscous force. Since these forces differ from one system to another depending on the nature of the solid and the liquid, there is no unified treatment of the subject.

Suspensions exhibit a variety of non-Newtonian behaviors due to the existence of these internal structures. Some of the behavior encountered frequently will be described qualitatively in the following sections, according to their phenomenological characteristics.

2.3.1 Effect of Volume Fraction Solid on Viscosity of Suspensions

It was found experimentally that for a given shear rate a suspension exhibits higher viscosity as volume fraction solid, g_s, increases. EINSTEIN [1906, 1911] derived an expression for "dilute" suspensions of solid in a Newtonian liquid:

$$\mu_{suspension} = \mu[1+2.5g_s] \tag{2.3}$$

where
μ: viscosity of the liquid phase
g_s: volume fraction of the solid phase

which has been verified experimentally by many investigators. The derivation is based on the assumption that the suspended particles do not interact with each other. Because of this assumption, shape, surface chemistry, and hydrodynamic interaction between particles are not included in the derivation. The model, unfortunately, fails abruptly when the volume fraction solid exceeds 0.1 and is of very limited use in industrial practice where suspensions of much higher volume fractions solid are involved.

Many researchers have tried to extend the Einstein model to cover suspensions with higher volume fractions solid by incorporating the effect of particle shape and hydrodynamic interaction into the Einstein expression. Such a model by BATCHELOR [1977] gives the viscosity as

$$\mu_{suspension} = \mu\left[1 + 2.5g_s + 6.2g_s^2\right] \tag{2.4}$$

which has higher order terms accounting for the interaction.

Another semi-empirical model by THOMAS [1965] which fits most experimental data of suspensions with non-agglomerating mono-size spherical particles up to a volume fraction solid of 0.6 leads to

$$\mu_{suspension} = \mu\left[1 + 2.5g_s + 10.05g_s^2 + A\exp(Bg_s)\right] \tag{2.5}$$

The similarity among equations (2.3) to (2.5) is obvious and equation (2.5) is reduced to equation (2.3) when g_s approaches zero. The first three terms in the equation account for the effect of hydrodynamic interaction of spheres and particle-particle collisions. The last empirical term was originally proposed by EYRING, et al. [1964] and accounts for the rearrangement of particles in a suspension, as it is being sheared. The term is proportional to the probability of a particle's transferring from one shear plane to another. The coefficient A and B for this expression were found to be 0.00273 and 16.6, respectively, for mono-size non-agglomerating spheres.

The influence of volume fraction solid on viscosity of suspensions leads to a concept of the maximum packing fraction, g_s^*, that a suspension can carry before clogging and preventing the flow to take place, or in other words, a fraction at which the viscosity increases to infinite value. Although this concept does not appear explicitly in many models proposed by investigators to explain the effect of volume fraction solid on

viscosity of suspensions, it can be realized in many of them. For example, BALL, et al. [1980] obtained an equation of the form:

$$\mu_{suspension} = \mu(1 - Kg_s)^{-5/(2K)} \tag{2.6}$$

where K: crowding effect factor

by integrating the differential form of the Einstein equation. Equation (2.6) is valid for concentrated suspensions of solid spheres. As predicted by equation (2.6), viscosity becomes infinite when $g_s \to 1/K$ and we can consider that the inverse of the "crowding factor" is proportional to the maximum packing fraction, g_s^*. The maximum packing fraction of mono-size spheres and variables affecting it are shown in Table 2.1 and Table 2.2.

2.3.2 Effect of Particle Morphology on Viscosity of Suspensions

KRIEGER, et al. [1959] proposed an equation of the form

$$\mu_{suspension} = \mu(1 - g_s / g_s^*)^{-sg_s^*} \tag{2.7}$$

to account for the effect of volume fraction solid. The equation is very versatile because not only does it incorporate the maximum packing fraction, g_s^*, but also the "intrinsic viscosity," s, which accounts for the particle shape and crowding effect found also in equation (2.6) at the same time. Note that the term, Kg_s, in equation (2.6) transforms completely into the ratio g_s / g_s^* in this equation.

The value of g_s^* strongly depends on particle size distribution. In general the maximum packing fraction of the system increases as the size distribution becomes wider.

In order to use equation (2.7) for systems which have particle shapes other than spherical, BARNES [1981] provided a simple empirical correction for the value of intrinsic viscosity of some simple geometric shapes.

For solid spheres: $s = 5/2$

For solid discs: $s = 3(\text{axial ratio})/10$

For solid rods: $s = 7\left[(\text{axial ratio})^{5/3}\right]/100$

By adjusting the intrinsic viscosity with the corresponding value, equation (2.7) is extended to cover systems which have non-spherical particles. Table 2.3 lists various values of s and g_s^* for suspensions of asymmetric particles, and Figure 2.1 shows such an effect in aqueous suspensions. It can be explained by considering that a disc will act as if it were a sphere, because the shear flow creates an angular momentum which causes the disc to spin and sweep across the liquid medium, as shown schematically in Figure 2.2. A similar explanation can be proposed for other shapes.

2.3.3 Shear-Thinning in Concentrated Suspensions

There is no clear boundary between dilute and concentrated suspensions. It is customary to refer to a suspension as concentrated when the interactions between suspended particles become significant.

From experiment, it is observed that, for constant volume fraction solid, the apparent viscosity of some suspensions decreases with increasing shear rate. For suspensions which are composed of rigid, non-agglomerating particles, they can align themselves into a more favorable arrangement in order to reduce resistance to flow , Figure 2.3. One possibility for the particles to achieve this is to form an ordered array instead of a random three-dimensional one. Such an array is sometimes known as two-dimensional layering, as described by BARNES [1989] and FERGUSON [1992]. The

macroscopic effect is the reduction of flow resistance which is manifested by a shear-thinning response.

There are two limiting values of viscosity generally found in suspensions: one is at very low shear rate and the other is at very high shear rate. At very low shear rate, solid particles are more or less in dynamic equilibrium and the apparent viscosity of the suspension does not increase any more by lowering the shear rate. The apparent viscosity at this point is known as zero-shear-rate viscosity or η_0. The other limit is at the other end of the shear rate spectrum. The amount of particles undergoing layering phenomena increases with increasing shear rate until a point when all the particles align themselves in another dynamic equilibrium. The apparent viscosity at this point is known as infinite-shear-rate viscosity, η_∞. Both are special cases and are exceptions rather than the rules for suspensions and it is not necessary that a system possess either one of these phenomena. The value of these pseudo-Newtonian viscosity is sometimes referred to as asymptotic viscosity. Many models such as those by CROSS [1965] and CARREAU [1972], section 2.3.7, have parameters accounting for these phenomena.

2.3.4 Shear-Thickening in Concentrated Suspensions

Experimentally it is found that, following the shear-thinning range which is attributed to two-dimensional layering, the apparent viscosity of non-aggregated suspensions increases with increasing shear rate. A plot of viscosity versus shear rate is shown in Figure 2.4. BARNES [1989] explained the effect to be the result of the destruction of the layered arrangement. The layered arrangement which has been formed is in dynamic equilibrium and unstable. When the shear rate reaches a critical value, the layered arrangement breaks down and the solid phase resumes random arrangement. He also believes that given the correct conditions, all concentrated suspensions of non-aggregating solid particles will exhibit shear-thickening phenomena. The major factors

affecting the existence and severity of shear-thickening are considered to be volume fraction solid, particle-size distribution, and viscosity of the liquid.

2.3.5 Time-Dependent Phenomena in Concentrated Suspensions

For suspensions which have solid particles that are capable of forming aggregates or "structure", two time-dependent phenomena are normally associated: thixotropic and rheopectic. Both of them involve formation and destruction of such structure.

Thixotropic materials are those whose apparent viscosity depend on both duration and rate of shear. When a thixotropic material is sheared at a certain rate, it develops a certain kind of internal structure. In suspensions, this internal structure consists of solid particles forming aggregates of solid suspended and carried along with the flow of the bulk. If the shear rate is suddenly increased, this structure will gradually break down and reach another dynamic equilibrium state that is characteristic for the new shear rate, Figure 2.5. The apparent viscosity of the material is lowered by such process. In the reversed situation, the apparent viscosity increases when such structure builds up at lower shear rate. In some systems including semi-solid slurries of alloys, it may not be possible to repeat the results of previous test with the same sample after a "long" recovery time. When this is the case, the materials are termed time-dependent materials. Another way to identify them is to perform hysteresis loop deformation.

Another time-dependent behavior is known as rheopectic. It is the case when the internal structure builds up with increasing shear rate causing the apparent viscosity to increase. Few cases of suspensions possess this behavior; an example is the aqueous suspension of bentonite clay.

2.3.6 Concentrated Suspensions with Viscoplastic Behavior

Concentrated solid-liquid suspensions have particularly strong particle interactions and often exhibit a viscoplastic behavior over a certain observation time period. Under application of a small stress, these systems deform elastically with finite rigidity to some extent. When the applied stress exceeds a certain value, continuous deformation occurs and the materials flow as normal viscous fluids. The yield stress, as a result, is regarded as one of the material rheological properties signifying the critical point of transition from solid-like to liquid-like behaviors.

2.3.7 Phenomenological Models

Because the deformation and flow response of materials can be completely described when their constitutive equations are exactly known, there have always been attempts to characterize these equations, which are also termed as rheological models. Some models are empirical, resulting wholly from observation and data fitting, while others are derived using hydrodynamics and fluid mechanics. Many models are found to be sufficient for representing flow response of liquids and suspensions encountered in engineering practice. Following are such models which are grouped according to their deviation from the Newtonian behavior. Later on in the section 2.4.3, some suspensions models which are derived from internal structure will be introduced.

Models for Viscous Materials

(a) Newtonian Model

It has been established experimentally that in a unidirectional simple shear motion, as shown in Figure 2.6, the three velocity components in Cartesian coordinates are

$$\begin{aligned} v_x &= v_x(y) \\ v_y &= 0 \\ v_z &= 0 \end{aligned} \tag{2.8}$$

and the flux of x-momentum in the positive y-direction is given by "Newton's law of viscosity," as

$$\tau_{yx} = -\mu \frac{dv_x}{dy} \tag{2.9}$$

where μ is the viscosity of the fluid.

The generalized form of the Newtonian viscosity for arbitrary flow is

$$\sigma_{ij} = p\delta_{ij} - \mu\left[\nabla v_i + (\nabla v_i)^t\right] + \left(\frac{2}{3}\mu - \kappa\right)(\nabla \cdot v_i)\delta_{ij} \tag{2.10}$$

where κ is known as dilatational viscosity. The third term on the right-hand side of the equation (2.10) is identically zero for ideal gases and incompressible fluids for which $(\nabla \cdot v_i) = 0$, by definition.

All kinds of structurally simple fluids including gases, gaseous mixtures, low-molecular-weight polymers, water, molten metals, and even suspensions or mixtures of these liquids at low volume fraction solid behave according to this expression.

(b) Power-Law (Ostwald-de Waele) Model

In practical situations involving various kinds of materials ranging from single-phase polymeric liquid to suspensions with moderate volume fraction solid, there is at least one region in which the apparent viscosity follows a simple mathematical expression

$$\eta = m\dot{\gamma}^{n-1} \tag{2.11}$$

The model contains two parameters. One is known as the power-law constant or m with units of Pa·s^n. The other is known as the power-law exponent or n. When $n = 1$

the model reduces to that of Newtonian fluids. Care must be taken in referring to the power-law constant because many investigators write equation (2.11) as

$$\eta = k\dot{\gamma}^m \tag{2.12}$$

and the exponent m is equal to $n-1$ in the equation (2.11) which is used here.

The power-law model is particularly useful because it can represent either the pseudoplastic or the dilatant behavior. When the exponent $n<1$, the fluid is said to be pseudoplastic or shear-thinning and the apparent viscosity decreases with increasing shear rate. When the exponent $n>1$, the fluid is said to be dilatant or shear-thickening and the apparent viscosity then increases with increasing shear rate. In systems which exhibit asymptotic behavior there is a region between the two extreme limits where the apparent viscosity is a function of shear rate. This region is usually in the range found in industrial processes and fitted well with the power-law model. This helps make it the most well-known and widely-used non-Newtonian empirical model in engineering work because a wide variety of flow problems have been solved analytically for it.

(c) Cross Model

The Cross model (CROSS [1965]) was originally derived from particle interaction in disperse systems. The apparent viscosity is given by

$$\eta = \eta_\infty + \frac{(\eta_0 - \eta_\infty)}{(1+m\dot{\gamma}^{n-1})} \tag{2.13}$$

It indicates a finite value, η_0, for the zero-shear-rate viscosity and η_∞ for the infinite-shear-rate viscosity. The other two parameters are the power-law exponent, n, and the power-law constant, m. Power-law behavior, as predicted by the model, exists in the transition region between the two asymptotic viscosities.

In most cases, the infinite-shear-rate viscosity cannot be approached due to mechanical limitation of the apparatus or the thermal dissipation of energy and it is normally dropped from the expression. The reduced form of the Cross model is then given by

$$\frac{\eta}{\eta_0} = \frac{1}{(1+m\dot{\gamma}^{n-1})} \tag{2.14}$$

(d) Carreau-Yasuda Model

The Carreau-Yasuda model (CARREAU [1972]) has five parameters and is sufficient to fit a wide variety of experimental curves. Similar to the Cross model, the Carreau-Yasuda model permits the zero-shear-rate viscosity and the infinite-shear-rate from experiments viscosity to be incorporated. The apparent viscosity is given by

$$\frac{\eta - \eta_\infty}{\eta_0 - \eta_\infty} = \left[1+(\lambda\dot{\gamma})^a\right]^{(n-1)/a} \tag{2.15}$$

Here, η_0 is the zero-shear-rate viscosity, η_∞ is the infinite-shear-rate viscosity, λ is a time constant, n is the "power-law exponent", and a is a dimensionless parameter describing the transition region between the zero-shear-rate region and the power-law region. Since it has one more parameter than the Cross model, the Carreau-Yasuda model can fit experimental data better. As in the Cross model, the infinite-shear-rate is sometimes dropped from the expression. The reduced form of the Carreau-Yasuda model leads to the expression:

$$\frac{\eta}{\eta_0} = \left[1+(\lambda\dot{\gamma})^a\right]^{(n-1)/a} \tag{2.16}$$

Models for Viscoplastic Materials

(a) Bingham Model

The Bingham model represents an ideal case of viscoplastic behavior. When the shear stress is lower than a certain value, the material behaves as if it were a rigid solid and there is no deformation. With shear stress higher than this value, it deforms in the same way as a Newtonian fluid does. The expression governing the behavior of Bingham materials is given by

$$\eta = \frac{\tau_0}{\dot{\gamma}} + \mu \qquad (\tau \geq \tau_0) \tag{2.17}$$

and $$\eta = \infty \qquad (\tau \leq \tau_0) \tag{2.18}$$

Common examples are both materials which have an "internal" structure, such as drilling mud, concentrated suspension, semi-solid alloy slurries with high volume fraction solid, and materials such as grease and butter. A qualitative explanation accounting for this phenomenon is that the material at rest has a three-dimensional structure of sufficient rigidity to resist a stress below a certain value. When stress exceeds this value, the structure disintegrates and the material deforms, as if it were a Newtonian fluid. It is very important to stress that the Bingham model and the following Herschel-Bulkley model are time-independent. In many materials the recurrence of a yield point after deformation has stopped requires a certain amount of time because the internal structure does not reform instantaneously. To refer these materials as "having yield points" is more appropriate than to refer to them as exhibiting Bingham or Herschel-Bulkley behaviors.

(b) Herschel-Bulkley Model

The Herschel-Bulkley model is an extension of the Bingham model, as the power-law is of the Newtonian model. In the Herschel-Bulkley model, when the applied stress exceeds the yield point the material deforms as if it were a power-law fluid; the generalized expression is given by

$$\eta = \frac{\tau_0}{\dot{\gamma}} + m\dot{\gamma}^{n-1} \qquad (\tau \geq \tau_0) \tag{2.19}$$

and $$\eta = \infty \qquad (\tau \leq \tau_0) \tag{2.20}$$

As in the case of the power-law model, the Herschel-Bulkley model is compatible for both shear-thickening and shear-thinning behaviors depending on the exponent n.

2.4 Rheology of Semi-Solid Metals

In the late 1960's the interest in deformation behavior of metals in the mushy state began. The pioneering work by METZ, et al. [1969] and [1970] showed that semi-solid dendritic aluminum alloys develop strength to a certain extent when the volume fraction solid is as low as 0.2. It was confirmed later in the work by SPENCER, et al. [1972] in which he used a concentric cylinder rheometer to shear semi-solid Sn-15 wt.% Pb at various volume fraction of solid. It was also during this study that SPENCER, et al. [1972] sheared the solidifying Sn-Pb sample during cooling from above the liquidus temperature. The morphology of the primary phase was changed from the normal dendritic to non-dendritic by the effect of shearing. The rheological behavior of non-dendritic slurries was found to be drastically different from that of a dendritic one. Not long after this discovery, many ideas on processing in the semi-solid state were generated mainly by the Solidification group at the Massachusetts Institute of Technology.

Since then semi-solid metals processing has been the topic of many studies and enjoys its status today a status of a fundamental complement to solidification processing. There have been many good reviews of the topic of both theoretical and practical points of view but the most comprehensive one is that by FLEMINGS [1991].

As mentioned in the appendices, there are various techniques to characterize the rheological behavior of semi-solid metals. The concentric cylinder rheometer is often

preferred because it allows a direct interpretation of the data; on the other hand the compressive and extruding techniques closely resemble the actual forming process. Since most investigators have used concentric cylinder rheometers, the experiments reported below, unless otherwise stated, were carried out in them.

2.4.1 Semi-Solid Metals with Dendritic Primary Phase

Almost all of metallic alloys solidify with a dendritic primary phase under normal conditions. Deformation characteristics in semi-solid state were thought to be critical to many macroscopic phenomena, such as hot-tearing found in castings. METZ, et al. [1969] and [1970] using block shearing technique and SPENCER, et al. [1972] using concentric cylinder technique carried out shearing experiments on semi-solid alloys with volume fractions solid up to about 0.5 at deformation rates of 0.01 and 0.16 s^{-1}, respectively. The results are shown in Figure 2.7. It was concluded that during solidification there is a certain point when the dendrites form a cohesive network and the semi-solid develops strength. The stress required to shear the sample at constant rate increases until it reaches the maximum point (the "apparent yield stress"), which is shown as a function of volume fraction solid in Figure 2.8. Deformation up to this point is believed to consist of grain-boundary sliding together with dendrite distortion. Further deformation creates fissures at which the shearing is localized and the shear stress drops drastically.

The effect of observation time mentioned earlier in section 2.2 is demonstrated in the work by LAXMANAN, et al. [1980]. Their experiments were conducted at extremely low deformation rate using a compressive plastometer and they found that semi-solid Sn-15 wt.% Pb with a dendritic structure at volume fractions solid from 0.35 up to 0.5 exhibit a pseudoplastic behavior without any yield point. Also reported was the apparent viscosity ranging from 10^7 Pa·s at a shear rate of 10^{-2} s^{-1} to 10^{10} Pa·s at a shear rate of 10^{-5} s^{-1} . Figure 2.9 demonstrates compression tests of dendritic specimens at two

different loads. A power-law model was fitted with the results and showed relatively good agreement. PINSKY, et al. [1984] reported the power-law shear-thinning response in a set of experiments with a parallel plate viscometer. It is still important from an engineering point of view that semi-solid metals with a dendritic structure exhibit "apparent" yield points under relatively high deformation rate.

Although semi-solid metals with a dendritic structure behave like highly viscous fluids, they have a certain limit of deformation. LAXMANAN, et al. [1980] found that the samples cracked at a moderate strain. PINSKY, et al. [1984], by using the same technique as LAXMANAN, et al. [1980], observed similar results. They also arranged their experimental setup to simulate the situations encountered in applications, such as extrusion, and concluded that the deformation occurs in two distinct stages. The first stage is the compaction of solid during which the liquid is squeezed out without any significant flowing of the solid phase. The second stage follows when the stress reaches a value that remains stable thereafter. SUERY, et al. [1982] investigated deformation of Sn-15 wt.% Pb at rates ranging from 10^{-3} to 10^{3} s^{-1} and reported that, in the range of low deformation rate, there is extensive segregation of the liquid phase. At higher deformation rate, on the contrary, the flow is more or less homogeneous. Given enough time as in the slow deformation, the interdendritic liquid flows readily and the deformation is controlled by that of the primary solid and the bulk semi-solid exhibits a pseudoplastic behavior described by power-law model, as assumed by Laxmanan.

Viscoelastic response is usually considered insignificant in semi-solid metal processing. However, a recent hot cracking study by QINGCHUN, et al. [1991] established that semi-solid Al-5 wt.% Cu exhibits a viscoelastic behavior that are in agreement with the basic Kelvin model.

2.4.2 Semi-Solid Metals with Non-Dendritic Primary Phase

Effect of Agitation on Microstructure of Semi-Solid Metals.

In 1972, while investigating the deformation behavior of a dendritic semi-solid Sn-Pb alloy with a Couette-type rheometer, SPENCER, et al. [1972] found that, with imposed shearing during continuous cooling from above liquidus, the primary dendrites gradually evolved into spheroidal fragments. The evolution was found to be enhanced by increasing the speed of rotation and consisted in the dendrites transforming into transient rosette-shaped particles and finally into spherical particles.

JOLY, et al. [1976] observed that, besides speed of rotation, non-dendritic evolution during continuous cooling of Sn-15 wt.% Pb is also enhanced by decreasing cooling rate. Since the non-dendritic evolution occurs over a certain period of time, many investigators eliminated the effect of solidification on the rate of evolution by holding the semi-solid at constant temperature and under constant shearing. The technique is termed as isothermal shearing (or holding) experiment and it was observed that during such an experiment the primary dendrites further evolved with time.

Not only does agitation change the primary phase morphology, it also affects the particle size of the primary solid. VOGEL, et al.[1979], MIWA, et al. [1981], ICHIKAWA, et al. [1987], and KATTAMIS, et al. [1991] observed the effect on the morphology and size in continuous cooling experiments and found that, at a given cooling rate, an increase in speed of rotation resulted in a smaller particle size. MORI, et al. [1984] used a concentric cylinder rheometer and stirring paddle with various gap distances and found that the particle size of rheocast Al-5 wt.% Cu decreases with increasing shear rate and smaller annular gap.

Another way of documenting the particle size change is to use surface area per unit volume (specific surface area) instead of average particle size. TAHA, et al. [1987] measured the interfacial area between the solid primary phase and the liquid of samples

which were cooled continuously under various shear rates and found that it decreased with increasing shear rate. KATTAMIS, et al. [1991] also found that, during isothermal holding, it decreased with holding time. The effect of decreasing specific area is complicated by the fact that the solid phase also undergo simultaneous coalescence and Ostwald ripening.

Many explanations have been given to account for the evolution of the structure. VOGEL, et al. [1979] proposed that high-angle grain boundaries are formed within dendrites due to the bending of dendrite arms during shearing. The grain boundaries are then wetted by liquid film leading to dendrite arm fragmentation. Experiments by LEE, et al. [1980], APAYDIN, et al. [1980], and CHENG, et al. [1986] are in agreement with the proposed theory which became known later as "strain-induced recrystallization and sintering."

The non-dendritic evolution is also accompanied by cluster formation, or agglomeration. It is usually referred to as "internal structure" or merely "structure" mostly by investigators with continuum mechanics background. Many investigators attribute this phenomenon to the collision and coalescence of solid particles due to random movement within the flowing liquid. The coalescence is thought to be highly dependent on crystallographic orientation and surface energy (LEE, et al. [1980]). APAYDIN, et al. [1980] studied the microstructure of rheocast Al-10 wt.% Mg under electron microscope equipped with Laue X-ray microbeam analyzer. They found that the boundaries between coalesced particles are low angle and special grain boundaries (high angle grain boundaries which have an unusually low surface energy). They concluded that these boundaries may be formed either by sintering after collision of these particles or by twinning growth. The degree of coalescence depends on shear rate and is characteristic of that particular shear rate.

Structural break-up and coalescence are believed to be concurrent phenomena . A dynamic equilibrium between the two opposing processes is established if the slurry is sheared at constant temperature for a long enough time (ICHIKAWA, et al. [1978] JABRANE, et al. [1992]). When this is the case, the slurry is said to reach steady-state and the apparent viscosity at this point is also known as steady-state viscosity.

An experimental technique known as shear rate jump or step test consists of shearing a semi-solid at a constant shear rate for a "long" time until the structure is fully developed and is characteristic of that particular shear rate. The apparent viscosity at this point is termed steady-state value. The shear rate is then changed suddenly to another value and the structure changes to another which is characteristic of the new shear rate. When the new shear rate is higher, the agglomerates are found to undergo structural break-up. If the new shear rate is lower, the degree of coalescence increases. The rates at which the structure changes are not equal, the structural break-up is found to occur faster than the structural build-up.

An extensive study on particle size and morphology by JABRANE, et al. [1992] revealed that volume fraction solid is also a major factor determining the particle size in rheocast Al-5.2 wt.% Si. The experiment consisted in continuous cooling the sample at constant speed of rotation of 60 rpm. The sample was let to cool down to a desired temperature and then sheared at various rates under isothermal conditions. At a volume fraction solid of 0.2, increasing shear rate yielded rheocast alloy of finer particle size. At volume fraction solid of 0.5, contrary to previous belief, it was found that particle size increases with increasing shear rate. The number of the particles per agglomerate was found to be decreasing with increasing shear rate.

Liquid entrapment by the primary phase has also been reported. Two different kinds of liquid entrapment exist. During structural evolution, dendritic primary phase is broken up and transforms into transient rosette-shaped particles. These transient particles

entrap and incorporate liquid whose amount is reduced during the evolution (JOLY, et al. [1976]). Another type of liquid entrapment associated with coalescence was suggested by ITO, et al. [1992]. Inside a group of solid particles forming an aggregate liquid may be trapped, Figure 2.10, and move along with the aggregate, causing the system to behave as if it had a higher volume fraction solid.

Effect of Agitation on Mass Transport in Liquid Phase

Mass transport phenomena are also inherent to semi-solid metal slurries. It has long been known that surface energy provides a driving force for structural coarsening (Ostwald ripening). It is believed to play an important role in semi-solid metal slurries due to the relatively fast mass transport in the liquid phase. In both dendritic and non-dendritic systems, primary solid phase is found to coarsen over a period of time. OBLAK, et al. [1976] observed the effect in reheated non-dendritic ferrous alloys and found a good correlation with the cubic law predicted by the Liftshitz-Slyozov-Wagner (LSW) coarsening theory.

In rheocasting, the mass transport in the liquid phase is, no doubt, enhanced by the convective movement of liquid due to shearing (VOGEL, et al. [1979], MOLENAAR, et al. [1986], and WAN, et al. [1990]) analyzed the flow around a spherical particle in a concentric cylinder rheometer using dimensionless numbers and concluded that for a dendritic primary phase cellular growth prevails due to the convection controlled mass transport ahead of the solid/liquid interface. For non-dendritic spherical particles under shearing flow, as in a concentric cylinder rheometer, WAN, et al. [1990] extended the LSW theory and concluded that:

$$r^{7/3} - r_0^{7/3} = kt \tag{2.21}$$

where

r: particle radius at $t = t$

r_0: particle radius at $t = 0$

in which the exponent of the radius is equal to 7/3 instead of 3, which is predicted by LSW theory. The rate constant k for diffusion-controlled coarsening is shown to be proportional to the shear rate and solute diffusivity according to:

$$k = \frac{1.56 D^{2/3} \dot{\gamma}^{1/3} \sigma V_m c_l (1 - c_l)}{RT(c_s - c_l)^2} \tag{2.22}$$

where

D = diffusion coefficient (independent of concentration)
σ = interfacial energy
c_s = concentration in the solid
c_l = bulk concentration of the melt
V_m = molar volume

In another paper WAN, et al. [1990] studied the effect of mass transport on the coarsening of Pb-37 wt.% Sn under isothermal shearing. He proposed two mechanisms which are thought to be governing the particle size. One is Ostwald ripening which was previously analyzed and can be represented by equations (2.21) and (2.22). The other is coalescence of particles, schematically demonstrated in Figure 2.11, which is borrowed from a model for liquid phase sintering derived by TAKAJO, et al. [1984]. Particles are thought to coalesce and form "necks". These necks grow with time due to the presence of a curvature-induced concentration gradient. The derivation combines both mechanisms and leads to a similar equation as (2.21) but with a new rate constant:

$$d^{7/3} - d_0^{7/3} = k't \tag{2.23}$$

and

$$k' = k'_{\text{coalescence}} + k'_{\text{Ostwald}}$$

$$k'_{\text{coalescence}} = \frac{1.96 v q_c k}{\varepsilon Q^{7/3}}$$

$$k'_{\text{Ostwald}} = 2.39k$$

where

$\nu =$ the average number of necks per particle

$q_c =$ the fraction of low - energy grain boundaries

$Q = \bar{r} / r$ at steady state

$$\varepsilon = \int_{a_{N_1}}^{a_{N_2}} \left[\frac{1}{2} \left(a_N^2 - a_{N_1}^2 \right) \right]^{4/3} da_N$$

The neck radius $= a_N r$

2.4.3 Rheological Behavior of Semi-Solid Metals with Non-Dendritic Structure at High Strain Rate

It was reported by SPENCER, et al. [1972] that non-dendritic semi-solid slurries of Sn-15 wt.% Pb exhibit more fluidity than dendritic ones. This fluidity, even at high volume fractions solid, makes it possible to process alloys in the semi-solid state.

Effect of Volume Fraction Solid

All investigators agree that increasing volume fraction solid increases the apparent viscosity of semi-solid slurries. In a continuous cooling experiment SPENCER, et al. [1972] found that the apparent viscosity of semi-solids increases with decreasing temperature due to the increasing volume fraction of primary phase. JOLY, et al. [1976] also found that at high shear rates the apparent viscosity of continuously cooled slurries of Sn-15 wt.% Pb alloy can be described by an equation of the type:

$$\eta = A \exp(B g_s) \tag{2.24}$$

The coefficients A and B are found to be functions of shear rate and cooling rate. They also stressed the similarity between the above expression and the equation proposed by THOMAS [1965] in which the last term has the same exponential relation.

The effect of volume fraction solid on the apparent viscosity of semi-solid Al-6.5 wt.% Si slurries and composite slurries were systematically reported by MOON [1990]. It was found that the Thomas equation fits experimental measurements well in both systems. The *A* and *B* coefficients were also found to be dependent on shear rate and cooling rate. The coefficient *B* was strongly dependent on shear rate, while the effect on coefficient *A* was rather insignificant.

Since agglomerates also have the tendency to entrap liquid inside them, the semi-solid slurry behaves as if it contained less liquid. ITO, et al. [1992] carefully studied and measured the amount of liquid entrapped inside agglomerates after successive polishing of quenched samples. He suggested that the effective volume fraction solid, i.e. volume fraction of solid plus volume fraction of entrapped liquid, be used if one attempts to correlate the volume fraction solid to the apparent viscosity.

Effect of Particle Size and Shape

Investigators found that, during continuous cooling, a higher cooling rate yields a higher apparent viscosity. The effect is explained by considering the microstructure. At higher cooling rate, primary dendrites do not have enough time to evolve into spheroidal particles. The deformed dendritic and transient rosette-shaped structures cause more resistance to the flow than the spheroidal one. Another possible explanation is that a high cooling rate yields finer particles. ICHIKAWA, et al. [1978] carried out experiments on Al-Cu alloys at various compositions up to 20 wt.% Cu and found that, as primary solid becomes finer, the apparent viscosity of the slurry increases. The effect, however, is very complicated to study.

MOON [1990] reported the difference between the apparent viscosity of semi-solid Al-6.5 wt.% Si and that of composite slurries consisting of liquid metal and SiC particulates. At the same volume fraction solid viscosity of the semi-solid metal slurries

is lower than that of the composite system. He concluded that semi-solid slurries with a solid phase having a high specific surface area (high aspect ratio particles) exhibits higher apparent viscosity than slurries with a solid phase of lower specific surface area.

An isothermal holding experiment consists of interrupting the cooling of the melt at a temperature in the semi-solid range and holding the sample at that temperature for a certain period of time while the shearing continues at a constant speed. During holding the structure breaks up and becomes non-dendritic while the apparent viscosity decreases with holding time as established by JOLY, et al. [1976], MOON [1990], and KATTAMIS, et al. [1991]. With long enough holding time, a more or less constant value of apparent viscosity is reached, commonly known as "steady-state viscosity" at that particular shear rate and volume fraction solid. For a given cooling rate and a shear rate, the time required to reach this steady state decreases with decreasing volume fraction and is usually of the order of 10^3 s (MOON [1990] and KATTAMIS, et al. [1991]).

Viscosity during Continuous Cooling

Many investigators have observed the apparent viscosity of semi-solid alloy slurries and fitted the experimental data with rheological models. There seem to be two different trends in these studies. Some investigators have prime interest in viscosity at conditions which are useful for processing, while others have a theoretical interest. In continuous cooling experiments, structural evolution does not reach the steady state and to model the rheological behavior at that state is virtually prohibited. One has to incorporate both solidification theory, heat and mass transport, hydrodynamics, all at transient state. Thus, investigators who have interest in processing parameters collect data and fit them with simple, empirical models. The relation between shear rate and apparent viscosity seems to be of most interest. JOLY, et al. [1976], LEHUY, et al. [1985] and TAHA, et al. [1987] found that the viscosity of semi-solid metals during

continuous cooling at a certain volume fraction solid between 0.1 and 0.5 fits the power-law equation

$$\eta = m\dot{\gamma}^{n-1} \tag{2.11}$$

Equation (2.11) is a phenomenological model and describes the apparent viscosity during continuous cooling only; it does not imply the time-independent nature of the materials. Table 2.4 shows power-law parameters from various works on non-dendritic semi-solid metal systems. All of them exhibit shear-thinning behavior and have power-law exponents ranging from 0.6 to -0.9. The pre-exponent m was found by many investigators to be an exponential function of volume fraction solid of the form:

$$m = A\exp(Bg_s) \tag{2.12}$$

Besides the hydrodynamic interaction the pseudoplasticity of these semi-solid metals can also be partly explained by considering the ability of a non-dendritic solid phase to form aggregates. At low shear rate viscosity is high due to agglomeration. At higher shear rate agglomeration decreases resulting in the decrease of the apparent viscosity (FLEMINGS [1991]). The situation is more complicated when structural evolution is concurrent, as in the case of high cooling rate, and it is extremely difficult to establish a theoretical model for such dynamic phenomena.

Some investigators incorporate other parameters into the correlation. Such parameters are volume fraction solid and cooling rate. MORI, et al. [1984] studied Al-5 wt.% Cu alloy and proposed a correlation equation between apparent viscosity, shear rate, solidification rate, volume fraction solid, and geometry of the rotor. The equation is given by:

$$\eta = A\left(n^{-1.8}\right)\left(\frac{dT}{dt}\right)^{0.6} e^{(13g_s)} \tag{2.25}$$

where dT/dt is cooling rate, n is rotation speed in s^{-1}, g_s is volume fraction solid, and A is a geometric constant (equals to 1.8 for paddle and 0.9 for cylinder rotor).

Steady-State Behavior: Pseudoplasticity

Some investigators have focused their interest on the systems that fully develop their structure and steady-state (dynamic equilibrium) values of viscosity have been reached in isothermal holding experiments. A plot of these steady state values of viscosity vs. the corresponding shear rate is commonly known as steady-state response.

There is a variety of time-independent models based on suspensions of rigid solid spheres. These models are derived by considering hydrodynamic interaction between solid spheres and are valid only for non-agglomerating systems. Many investigators measured steady state viscosity of semi-solid slurries and fitted the data with such models. All of the proposed models indicate that semi-solid metal slurries with volume fractions solid from 0.1 to about 0.5 exhibit pseudoplastic behavior.

Similar to the continuous cooling viscosity, many investigators found that at a certain volume fraction solid (from 0.1 to 0.5) steady-state viscosity values of the semi-solid metal slurries can also fit, with good correlation factors, the power-law model prediction (JOLY, et al. [1976], MOON [1990], and ITO, et al. [1992]).

More complicated empirical correlations exist such as one by KATTAMIS, et al. [1991]. They found a correlation of the form:

$$\eta_{relative} = \frac{\eta}{\mu_0} = 1 + \frac{K g_s (S_v / S_{v0})(\bar{d} / \bar{d}_0)}{K - g_s} + 2.03 \times 10^4 g_s \dot{\gamma}^{-0.727} \qquad (2.26)$$

where η is apparent viscosity, μ_0 is the viscosity of liquid, K is a constant, S_v and $\bar{d}$ are the steady state value of the specific solid-liquid interface area and average particle

size, S_{v0} and $\bar{d}_0$ are corresponding values at the beginning of the isothermal holding, and g_s is volume fraction solid.

Another model proposed by TURNG, et al. [1991] is also an empirical model based on their steady-state measurement of Sn-15 wt.% Pb which has the form:

$$\eta = \eta_{\infty}\left[1-\left(g_s / g_s^*\right)\right]^{-m}\left[1+\left(\dot{\gamma}^* / \dot{\gamma}\right)^a\right]^{n/a} \tag{2.27}$$

where

η_{∞} = "asymptotic" viscosity at very high shear rate dependent on volume fraction solid
g_s^* = critical volume fraction solid
$\dot{\gamma}^*$ = critical shear rate dependent on volume fraction solid
n = power – law constant
m = parameter dependent on shear rate
a = constant describing the transition region

It is the first model describing viscosity of alloy slurries which incorporates the asymptotic (infinite-shear-rate) viscosity at very high shear rate as described in section 2.6.1. The critical parameters are associated with the transition from power-law to this pseudo-Newtonian behavior at high shear rate. Although the measurement was done at relatively high shear rates (up to 1200 s^{-1}), the infinite-shear-rate viscosity was not fully achieved and the lowest ratio of η / η_{∞}, about 1.2, was obtained. The equation also applies to continuous cooling data provided that proper modifications be made for some parameters in the equation.

Dilatant (Shear Rate Thickening) at Constant Structure

Shear thickening is observed in shear rate jump experiments. The experiment consists of continuously cooling the sample under a constant shear rate to a certain temperature in the semi-solid range. The sample is then held at that condition for a certain period of time until the structure attains steady state. Once this state is reached

the shear rate is abruptly changed to a new value and the new value of apparent viscosity is read immediately. The concept of measurement is that the shear rate change occurs abruptly so that the structure does not have time to develop and the new viscosity is the viscosity of that particular structure. By carrying out many experiments at various new shear rates, viscosity may be plotted versus the new shear rate. Such a plot is known as constant structure response flow curve. It was shown by KUMAR [1994] that constant structure response of non-dendritic Sn-15 wt.% Pb is shear-thickening which is opposite to the shear-thinning response of steady-state viscosity.

Time-dependent Materials: Thixotropy

As early as its discovery, non-dendritic semi-solid metal slurries were found to be thixotropic. SPENCER, et al. [1972] discovered that semi-solid Sn-15 wt.% Pb slurries exhibit a thixotropic behavior. In experiments in which shear rate was increased from one value to another, measured torque increased abruptly and then decreased to a new steady state value. JOLY, et al. [1976] measured the hysteresis loop of semi-solid Sn-15 wt.%Pb and found the thixotropic behavior. The area inside the hysteresis loop represents the energy spent in breaking up the structure.

Although, all investigators agree that semi-solid metal slurries are highly time-dependent materials, there is very limited work on the subject. One of the few is by BROWN, et al. [1992] and KUMAR [1994] who proposed an internal variable model for rapid transient experiment and later developed a constitutive equation from hydrodynamic models. The internal variable equation is stated as:

$$\tau_{ij} = \hat{f}_{ij}\left(\dot{\gamma}_{mn}, T, s_1, s_2, \ldots, s_k\right) \text{ and}$$

$$\frac{ds_p}{dt} = \dot{s}_p = \hat{g}_p\left(\dot{\gamma}_{mn}, T, s_1, s_2, \ldots, s_k\right) \qquad 1 \le p \le k \tag{2.28}$$

where

$\dot{\gamma}_{mn}$ = shear rate,

$\hat{f}_{ij}(\dot{\gamma}_{mn}, T, s_1, s_2, \ldots, s_k)$ = flow equation,

τ_{ij} = shear stress,

T = temperature,

$s_1, s_2, \ldots, s_k$ = set of k internal variable that characterize the state of the material, and

$\hat{g}_p(\dot{\gamma}_{mn}, T, s_1, s_2, \ldots, s_k)$ = evolution equation for internal variable p.

From the internal variable framework, KUMAR [1994] developed a flow equation for semi-solid with spherical non-dendritic structure of volume fraction up to 0.5 in the form of scalar constitutive equation. The equation has the form:

$$\tau = A\frac{(c/c_{max})^{1/3}}{1-(c/c_{max})^{1/3}}\mu_f\dot{\gamma} + (n+1)Csf_s\mu_f^{n+1}\dot{\gamma}^n \qquad (2.29)$$

where

$A = A(s)$ = hydrodynamic coefficient which is a function of particle size and shape

c = packing fraction

c_{max} = maximum packing fraction

$C = C(T)$ = geometric constant which is a function of temperature

s = internal variable representing degree of agglomeration

μ_f = fluid viscosity

n = exponent constant

The flow equation was derived by combining Frankel-Acrivos' hydrodynamic interaction between particles in the slurry and deformation at the neck of bonding particles. The model is capable to explain shear rate thickening (constant structure response) and shear thinning (steady-state response) behaviors observed in experiments on Sn-15 wt.% Pb.

Viscoplastic: Semi-Solid with Yield Point

Non-dendritic semi-solid metals with a volume fraction solid exceeding about 0.5 are found to be viscoplastic. It is generally agreed that at such a high volume fraction the spherical particles come into contact with each other and form a three-dimensional continuous network. AHMED, et al. [1992] proposed an empirical model in tensorial form which is similar to Herschel-Bulky with shear thickening flow.

$$\tau_{ij} = \left\{ \eta + \tau_0 \frac{\left(1 - \exp\left(-m' \left| \sqrt{I_2 / 2} \right| \right)\right)}{\left(I_2 / 2\right)} \right\} \dot{\gamma}_{ij} \qquad (2.30)$$

where the viscosity term is assumed to obey a shear-thickening power-law, $\eta = m\dot{\gamma}^{n-1}$

The model was used in computer simulation of forging of semi-solid Sn-15 wt.% Pb and results were in agreement with experimental measurement. Recently, SANNES, et al. [1994] used a vane shear plastometer to measure yield points of reheated semi-solid magnesium alloys with non-dendritic structure and found that they also exhibit yield phenomena when the volume fraction solid is about 0.6. A reconstruction of their result is shown in Figure 2.12. It is concluded that the solid necks interconnect and form a three dimensional network.

2.4.4 Rheological Behavior of Semi-Solid Metals with Non-Dendritic Structure at Low Strain Rate

Rheological properties of semi-solid metals with non-dendritic structure can be investigated in a compression test between two parallel plates. The rate of deformation is, however, much lower than that obtained in concentric cylinder setup and usually in the range from 10^{-5} to 10^{-1} s^{-1}. Experiments of this kind usually involves reheating rheocast specimens to a semi-solid temperature and compressing them according to a desired experimental technique.

LAXMANAN, et al. [1980] also conducted a series of constant-force compression experiments with non-dendritic semi-solid Sn-15 wt.% Pb. Their results are displayed in Figure 2.13 in which non-dendritic specimens were compressed at various loads and engineering strains were measured as a function of time. It was found that non-dendritic semi-solid obeyed the power-law model, equation (2.11), in the volume fraction solid range of 0.3 to 0.6. An empirical expression of the form:

$$\eta = a\exp(bg_s)\dot{\gamma}^{(cg_s+d)} \tag{2.31}$$

where

η: apparent viscosity
g_s: volume fraction solid
$a = 10.5$
$b = 20.6$
$c = 1.78$
$d = -1.39$ for non - dendritic semi - solid Sn - 15 wt.% Pb

was obtained by carrying out compression tests at various volume fractions solid and using equation (A.11) to estimate the apparent viscosity at a certain shear rate and volume fraction solid. The non-dendritic specimens deformed homogeneously up to $e = -0.8$ without cracking and required much less loads than dendritic ones.

PINSKY, et al. [1984] carried out a similar series of experiments on the same alloys using constant velocity cross-head to compress the specimens. The friction between the specimen and the plates was found to affect the stress-strain curve and liquid-solid segregation. The stress-strain dependence was found to be the power-law expression:

$$\sigma \propto \dot{\varepsilon}^n \tag{2.32}$$

where

σ: normal compressive stress

$\dot{\varepsilon}$: linear strain rate

SUERY, et al. [1982] investigated deformation behavior of Sn-15 wt.% Pb using a constant velocity compression technique. Figure 2.14 shows the fraction liquid of a non-dendritic specimen after compression as a function of radial distance from center. Non-dendritic specimens can be deformed up to $e = -0.7$ before massive segregation occurs.

2.5 Semi-Solid Processing

The interest in processing metals and alloys in the semi-solid state covers a broad range of systems from low melting point alloys such as zinc, magnesium alloys, aluminum alloys to high melting point alloys such as steels and high performance nickel-based alloys (CHENG, et al. [1986]). With an increasing concern about energy consumption, semi-solid forming is gaining industrial favor because it requires less force and a lower temperature. When compared to liquid-state processing, semi-solid forming is preferable because laminar flow is enhanced by the relatively higher viscosity, and the amount of shrinkage cavities and other casting defects is substantially reduced compared to conventional castings. The concept of forming in the semi-solid state became known as "thixoforming," whereas the production of starting non-dendritic material is known as "rheocasting."

2.5.1 Rheocasting

The major purpose of rheocasting is to obtain material with a non-dendritic structure for subsequent processing. Most of the processes are included in the review by FLEMINGS [1991]. Batch rheocasting usually employs mechanical agitation obtained by immersing a stirrer into semi-solid slurries while the same agitation may be supplied via electromagnetic force or cylindrical rotor in continuous rheocasting. There are other

variations of the process. KIUCHI, et al. [1992] proposed a method consisting of water-cooled drum crushing the semi-solid after the molten metal is poured on the top and partially solidified.

2.5.2 Thixoforming or Semi-Solid Metal Forming

The term was first used to describe any process involving forming of semi-solid metals with a non-dendritic structure. Presently, it is more general to refer to the process as semi solid metal forming. It usually involves reheating non-dendritic ingots into the semi-solid state and "deforming" them at that temperature. SSM forming has the advantage of a laminar mold-filling characteristic due to its higher viscosity compared to liquid metals. In any constrained flow pattern the stability of the flow is raised by a higher viscosity and this can reduce several defects generated during conventional liquid metal processing. There are also variations, such as thixocasting, thixoforging, thixomolding, and thixoextrusion. Interest in SSM forming also extends to forming of semi-finished product. One SSM process for producing metal strip was proposed by MATSUMIYA, et al. [1981]. The process consists of forming thin slab by squeezing SSM between two rolls.

2.6 Hypereutectic Aluminum-Silicon Alloys

Silicon has been widely used as an alloying element in almost all commercial aluminum alloys. Although most of the alloys being used are hypoeutectic, aluminum alloys with silicon content more than the eutectic composition, 12.6 wt.%, known as hypereutectic alloys, have been gaining in popularity during the past twenty-five years. Being one of a few alloying elements that do not increase the density of aluminum alloys, silicon in hypereutectic aluminum alloys also imparts to them a unique wear resistance due to the very high hardness of solid silicon crystals dispersed in the matrix. Besides the lightness and wear resistance, silicon also yields the hypereutectic alloys excellent

castability. The peculiar nature of the alloys makes them attractive to the automotive industry and desirable for wear resistant applications, where strength and weight saving are also required. Such applications are automobile engine blocks, air compressor cylinders, brake cylinders, to name but a few. It is expected that these alloys will gain more popularity with applications that do not require mechanical strength or toughness but rather lightness, such as housings or bodies Registered hypereutectic alloys are shown in Table 2.5 with their corresponding composition and casting methods.

2.6.1 Phase Equilibrium and Solidification of Hypereutectic Al-Si Alloys

Aluminum and silicon constitute a simple binary eutectic system with the eutectic point at about 12 wt.%Si and 577°C. The binary phase equilibrium diagram of aluminum and silicon from MURRAY, et al. [1984] is shown in Figure 2.15. Two solid phases are face-centered-cubic aluminum, α, and diamond-cubic silicon. With silicon content more than 12.6 wt.% the alloy solidifies with silicon as the primary phase. The maximum solubility of aluminum in silicon is 0.016±0.003 at.% at 1190°C, this temperature being the retrograde point of the Si solidus. The solubility at 577°C is less than 0.001 at.% and, for practical purpose, it can safely be neglected. The molten alloys are found to solidify with some degree of undercooling. Another deviation from equilibrium during solidification is also observed as the molten alloy undergoes eutectic transformation. The transformation temperature is suppressed below the equilibrium eutectic temperature at 577°C. The size and morphology of primary silicon vary with composition and cooling rate, as investigated by KOBAYASHI, et al. [1975], [1976], [1979], [1985], ATASOY, et al. [1984], and WEST, et al. [1985]. In conventional castings solidifying at moderate cooling rates primary silicon crystallizes as hexagonal plates joined together at a center and appear in a cross-sectioning as star-shaped particles.

Segregation of primary silicon is common in hypereutectic alloys. The effect is more pronounced at higher silicon content. TENEKEDJIEV [1989] observed the

microstructure of 17 wt.% Si alloy without refiner and reported heavy gravity-segregation in alloys cast in sand molds. Primary silicon was also found to nucleate preferentially at the mold wall causing silicon-depleted zone at the inner region of the casting.

The effect of vibration on solidification of hypereutectic alloys was studied by CLARO, et al. [1970]. In their experiment liquid melt was solidified in a crucible while being subjected to vibration via an immersed copper tube, which was also acting as heat sink for solidification. It was found that vibration enhanced precipitation of primary silicon around the copper tube, and heavy segregation was observed.

Aluminum-silicon alloys with silicon content from about 12 to 18 wt.% have excellent casting characteristics compared to other aluminum alloys. Fluidity of binary alloys, as measured by COLLIGAN [1973] in the AFS sand mold spiral test, increases with increasing silicon content up to a maximum at 18 wt.% Si. Relatively high heat of fusion allows the molten metal to flow and fill the mold. Beyond this composition, however, the castability decreases with increasing silicon content because of the high melting point of the alloys which increases rapidly due to the steep slope of the liquidus on the silicon-rich side. Primary silicon crystals also coarsen substantially due, in part, to the wide solidification range of these alloys, and impair mechanical properties of the castings such as fracture toughness and ductility. Only a small volume of alloys with a silicon content above 18 wt.% are being used since this situation worsens abruptly. It is almost impossible to obtain good quality castings of such alloys at conventional foundry solidification rates and many methods for producing high silicon alloys with good characteristics ranging from alloying to new fabrication techniques are being developed.

2.6.2 Effect of Microstructure on Mechanical Properties and Wear Resistance

Silicon crystals possess very high hardness (12,000 MPa Vickers) and contribute the abrasive wear resistance to the cast parts of the alloys. Wear resistance of the alloys

depends highly on the size and amount of primary silicon. It was found that increasing silicon content in hypereutectic alloys can improve the wear resistance of the castings. Another advantage of increasing the silicon content is that the casting can be lighter due to the lower density of this element (2.33 g/cm^3) compared to that of aluminum (2.70 g/cm^3).

The tensile strength of A390 alloy is found by TENEKEDJIEV [1989] to be dependent on the size of primary silicon and also on the fineness of the eutectic silicon. The tensile strength of test specimens increases with decreasing silicon particle size. MANDAL, et al. [1991] measured tensile strength in hypereutectic alloys with silicon content from 17 to 27 wt.% and found that beyond 22 wt.% the average hardness of the castings reaches a plateau at about 120 BHN and the tensile strength-particle size correlation is:

$$\text{Tensile Strength (in MPa)} = 252.8 - 3.73\bar{d}$$

where average particle size, $\bar{d}$, is in μm. The alloys in the test were refined with phosphorus and had a particle size ranging from 13 to 30 μm.

Ductility of hypereutectic aluminum-silicon alloys is poor and decreases with increasing silicon content. There is no report on the ductility of alloys with silicon higher than 22 wt.% Si, but it is expected to be lower than 0.5% which is the value of Al-22 wt.% Si alloy. As in the case of ductility, the toughness of the alloys with higher silicon is expected to be lower.

2.6.3 Semi-Solid Metal Processing of Hypereutectic Al-Si Alloys

ICHIKAWA, et al. [1987] studied the effect of shearing and phosphorus treatment on particle size of silicon. The solidifying alloys were sheared in a concentric cylinder rheocaster at ultra high speed and a fixed cooling rate of 3°C/ min. The result indicates

that silicon particle size in the untreated alloys up to 21 wt.% Si can be refined by shearing. Particle size slightly decreases with increasing shear rate. However, no significant refining effect was obtained in alloys with phosphorus addition.

SMITH, et al. [1991] used a graphite paddle to stir solidifying Al-19 wt.% Si and observed the microstructure. They concluded that agitation can either refine or coarsen the primary silicon. At the early stage of solidification when volume fraction solid is low coalescence of primary silicon crystals is the dominating mechanism. Fragmentation of primary crystals, however, becomes the dominating mechanism at higher volume fraction solid. The aggregates of silicon crystals were also found to be more spheroidal at lower cooling rates. Figure 2.16 is a schematic representation of such aggregate at an early stage and the corresponding microstructure evolution during continuous cooling under agitation.

Recently ARAKANE, et al. [1995] studied the effect of rotation speed and gap width (concentric cylinder rheocaster of 50 mm diameter inner cylinder) on the primary silicon particle size in Al-20 wt.% Si alloy. The speed of rotation varied from 8 to 167 rev/second and the gap varied from 2.5 mm to 7.5 mm. Figure 2.17 shows their results together with an adaptation of their results in terms of shear rate. It is clear that particle size becomes smaller at higher speeds of rotation and at smaller gap width.

The thermal spraying process, developed in the 1980's, was applied to the production of hypereutectic aluminum-silicon alloys by WARD, et al. [1992] and HENDERSON, et al.[1992]. The process included production of starting material having fine, uniformly distributed, equiaxed primary silicon embedded in an α-aluminum matrix. The starting material was then ready for thixoforming process. The major drawback of the process is the inherent porosity that is detrimental to the mechanical properties. In one part of their study, spray-formed Al-20 wt.% Si ingots were reheated into semi-solid state inside a Searle-type rheometer. The ingots contained angular

primary silicon of the size about 80 μm with aspect ratio about 2. Steady-state viscosity at shear rate ranging from 2 to 30 s^{-1} was measured as a function of cooling rate and fitted well with power-law equation with exponent n ranging from -0.3 to -0.9.

2.6.4 Other Processes Related to Production of Hypereutectic Al-Si Alloys

Because of the limitation encountered in the conventional process, many researchers have been trying to find alternative routes to produce fine-particle size, high silicon content hypereutectic aluminum-silicon alloys. SKELLY, et al. [1971] produced rapidly solidified hypereutectic alloy powder with silicon content from 22 to 45 wt.% Si. The powder was then hot pressed at a temperature around 560°C and was subsequently thermo-mechanically treated. The samples still exhibited very fine microstructure after being compacted and sintered. Mechanical properties were found to be tremendously improved. Yield points were in the range of 110 MPa to 180 MPa in 22 wt.% Si and 35 wt.% Si, respectively. Ductility was raised from 0.5 % in conventional Al-22 wt.% Si to 3 wt.% at the same composition. Parts that were made by this process had much better wear resistance and superior mechanical properties than conventionally cast parts of identical alloy composition due to the finesse and uniform dispersion of primary silicon.

In Japan, a solidification process called Duplex casting was introduced by OHMI, et al. [1992] which, it is claimed, substantially refines primary silicon. In the process, two kinds of alloy melts, i.e. "the first alloy" with a relatively low liquidus temperature and "the second alloy" with a relatively high liquidus temperature, were cast into a mold in sequence at various given time interval. A similar process consisting of mixing a cooler hypoeutectic melt with hotter phosphorus containing hypereutectic melt was also proposed. The process was termed slurry-melt mixing (SMM) process. It was proposed by OHMI [1994] that very fine primary silicon in the hypereutectic melt precipitate at high cooling rate due to the quenching effect created by mixing the two melts.

Recently, PARK, et al. [1995] developed a technique using electromagnetic force to attract silicon particles to a desired surface during isothermal holding in semi-solid state. Silicon crystals have a lower electrical conductivity compared to the molten alloy, hence, the electromagnetic force on these crystals is virtually zero and they move in a direction opposite to that of the imposed electromagnetic force.

CHAPTER THREE

EXPERIMENTAL PROCEDURE

3.1 Alloys Preparation

Hypereutectic Al-Si alloys with silicon contents of 30, 40, and 50 wt.% were prepared from pure 99.9% aluminum in the form of pellets and pure 99.999% silicon in the form of chips. Both were supplied by Johnson and Matthey Co. The starting materials were weighed and melted in a preheated graphite-clay crucible inside an Inductotherm 75 kW induction furnace. Melts were brought to 100°C above their liquidus temperature to ensure dissolution of the silicon and facilitate melt homogenization. Besides the electromagnetic stirring resulting from induction, melts were also vigorously agitated by a graphite paddle to guarantee the chemical homogeneity before casting into a twin-cylinder graphite mold. The mold has two cylindrical cavities of 2.54 cm diameter and 20.32 cm length, surface-coated with boron nitride. A typical cooling rate of the mold was 40°C/s.

3.2 Rheological Measurement with a Concentric Cylinder Rheometer

3.2.1 Apparatus

A vacuum induction furnace was modified to incorporate a Searle-type concentric cylinder rheometer, as shown in Figure 3.1. The furnace consisted of a vacuum chamber equipped with a 12.7 cm diameter water-cooled copper coil and an Inductotherm 15 kW induction power unit providing the current. The chamber was filled with argon to provide protective atmosphere during each experiment.

The dimensions of the rheometer are indicated in the Figure 3.2. The rotating and measurement unit was mounted on the top port of the vacuum chamber. A 1.27 cm case-hardened stainless steel shaft connected the graphite inner cylinder to a permanent magnet motor. The motor had a capability of reaching a maximum speed of 2,400 rev/min providing the minimum and maximum theoretical shear rate of 30 s^{-1} and 1,800 s^{-1}, respectively.

An optical torque transducer (Vibrac model TQ32) was installed in series with the drive shaft in order to monitor the torque necessary to maintain a constant speed of rotation during experiments. The calculated sensitivity of the instrument at this configuration is shown in Figure 3.3. At the lowest shear rate of 30 s^{-1} the rheometer has a sensitivity range from about 1 Pa·s to 100 Pa·s, while at a shear rate of 300 s^{-1}, the range is from about 0.1 Pa·s to 10 Pa·s.

The torque transducer was connected to the power supply unit which also amplified the signal from the transducer into standard 10 VDC. This amplified signal was logged by an IBM 486DX2 personal computer equipped with OMEGA digital data acquisition board model WB-Flash12-1 and OMEGA Quicklog software.

The temperature of the semi-solid was monitored by two type-K thermocouples which were inserted into the chamber via a feedthrough. The temperature difference between point A and B in Figure 3.2 was found to be less than four degrees during a continuous cooling experiment. Typical average cooling rates achieved in continuous cooling experiments were 35, 38, and 41°C/min for Al-30, 40, and 50 wt.% Si samples, respectively.

Average shear rate was calculated from the following expression (see Appendix):

$$\dot{\gamma}_{average} = \frac{2W_1}{(R_2 - R_1)\left(\frac{1}{R_1} + \frac{1}{R_2}\right)} \tag{3.1}$$

where W_1 is the angular velocity of the inner cylinder, R_1 is the radius of the inner cylinder, and R_2 is the radius of the crucible.

The apparent viscosity was calculated from a formula (see Appendix):

$$\eta = \frac{T}{4\pi H W_1}\left(\frac{1}{R_1^2} - \frac{1}{R_2^2}\right) \tag{3.2}$$

where T is the torque on the inner cylinder and H is the height of the liquid in the annulus.

At moderate and high speeds of rotation, slippage of the rotor may become a serious problem. In order to validate the equation (3.1) and (3.2) used in the calculation of apparent viscosity two non-slip boundary conditions has to be satisfied at the contact surface (inner and outer cylinder). To prevent this slippage at the inner rotating cylindrical surface, 24 grooves 0.127 cm deep were machined on that surface.

3.2.2 Apparent Viscosity Measurement during Continuous Cooling

The hypereutectic aluminum-silicon alloy ingot prepared as described in section 3.1 with a particular composition was remelted in the rheometer and maintained at a temperature 100°C above the corresponding liquidus for 5 minutes. The rotating cylinder assembly was then lowered down via the mechanism described in the preceding section until it immersed properly into the position, as shown in Figure 3.2. The motor was then turned on and the cylinder rotated at constant speed throughout the experiment. The system was cooled to the target starting temperature of 50°C above the corresponding liquidus, and held there for another 5 minutes. The continuous cooling experiment was

then started by shutting off the induction power. The sample cooled through the semi-solid range until it reached 585°C while the torque required to shear the alloy at a constant shear rate was recorded. The rotating cylinder was stopped at this temperature and the sample was allowed to cool down to room temperature before being taken out.

3.3 Batch Rheocasting

3.3.1 Apparatus

An apparatus for producing materials for subsequent testing was modified from the concentric rheometer setup and is shown schematically in Figure 3.4. The inner cylinder was replaced by a stirring unit consisting of two stainless steel rods 0.318 cm in diameter attached to a stainless steel disk-shaped holder. Because of the corrosive nature of liquid melts, graphite sleeves were put on the two stainless steel rods to prevent them from coming into contact with the melt. Because of the offset from the centerline, the stirring rods provide vigorous agitation when the drive shaft rotates. The crucible used in the rheocasting has the same dimensions as the one used in the concentric rheometer. Although the sample size in rheocasting experiments is larger than that used in the concentric cylinder experiment the typical cooling rate in rheocasting experiments is still of the same order of magnitude as that in the latter.

3.3.2 Rheocasting Procedure

The starting materials were prepared as described in section 3.1. A 180 g sample was cut from a cylindrical ingot and put in the graphite crucible. The sample was heated by induction until it reached 50°C above its corresponding liquidus. The stirrer was then lowered down and the stirring rods immersed properly in the melt, as shown in Figure 3.4. The melt was kept at this temperature for 5 minutes. The melt finally cooled down by shutting off the power supply, while the rods were rotating, providing the necessary vigorous agitation. The stirrer unit was stopped at 590, 700, and 850°C for Al-30, 40,

and 50 wt.% ingots, respectively, and the rheocast ingot was taken out when it cooled down to room temperature. The speed of rotation was 550 rpm for all alloys.

3.4 Rheological Measurement of Reheated Materials

3.4.1 Apparatus

The apparatus is shown in Figure 3.5. It consisted of two case-hardened stainless steel shafts aligned with the same centerline. The linear movement was provided by four linear motion bearings (two for each shaft). The displacement of the upper shaft was monitored by a linear voltage displacement transducer (LVDT) model LD200-10 supplied by OMEGA. A power supply unit model LDX-3A was connected to this LVDT and amplified the signal from the LVDT to standard 5 VDC. The same computer in section 3.2.1 was connected to it. Also on the upper shaft a tray made of aluminum was attached to provide space for placing standard weights. In the middle part of the setup where the specimen was located, there was a resistance-heating furnace composed of two semi-circular heating elements which were connected to an OMEGA temperature controller model CN7002 and solid state relay.

At the end of both shafts in the furnace, there were two adapters attached to both of them. Each adapter was secured to the shaft by a split-hub shaft collar. There were two types of adapters for each experiment. The one for compression test had dimensions as shown in Figure 3.6 (a). The other was a 60° cone which is shown in Figure 3.6 (b) for a yield stress measurement.

3.4.2 Experimental Procedure

Compression between Two Parallel Plates at Constant Force

Compression test samples were prepared from two types of specimens: rheocast ingots and conventionally cast ingots of the above three compositions. The ingots, due to

their extremely high hardness, were cut by an abrasive cutting wheel into test specimens with a shape of a hexagonal prism. The specimen whose dimensions are displayed in Figure 3.7 was assumed to have a circular cross section, with an apparent radius defined as:

$$\bar{r} = 0.52504\bar{d} \tag{3.3}$$

where
$\bar{r}$: apparent radius
$\bar{d}$: distance between two parallel hexagonal sides

At the beginning of the test a specimen was placed between the two parallel compression plates. It was then heated to 600°C at a typical rate of 9°C/min. The temperature difference between the upper and lower plates was maintained at less than 4°C. The locking collar was released when the target temperature was reached and the upper shaft transmitted to the compression plates a force equal to the weight on the tray. The differential vertical displacement of the upper plate, equal to $d(h/2)$ in equations (A.11) to (A.19), was monitored by the LVDT. The lower shaft remained stationary throughout the test.

Cone Penetration at Constant Force

A penetrator with the shape of a 60° cone replaced the upper compression plate. A 1.5 cm cubic specimen was placed on the lower plate and heated up to a desired testing temperature. Once it reached the target temperature, the locking collar was released in the same way as in the previous test and allowed the penetrator to pierce the specimen. The displacement was monitored, as previously described.

The yield stress in shear was calculated from the expression (see Appendix):

$$\tau_0 = K\frac{F}{h^2} \tag{3.4}$$

$$\text{where} \quad K = \frac{1}{\pi}\cos^2\alpha\cot\alpha \tag{3.5}$$

where F is the compressive force and h is the depth of penetration. The geometric constant for a 60° angle cone is equal to 0.214.

3.5 Image Analysis and Metallography

Metallographic specimens of both conventionally cast and rheocast samples were prepared for observation under optical and scanning electron microscopes (SEM).

For an optical microscope observation the samples were sectioned as shown in Figure 3.8, mounted in Bakelite, and polished. Photomicrographs were taken and quantitative metallographic evaluation was performed by computerized image analysis. The equipment for such an analysis is an Apple Macintosh IIsi computer with NIH Image Analysis software which is capable of measuring particle size and volume fraction.

Some specimens were deep-etched with concentrated hydrofluoric acid for 12 hours to remove the aluminum matrix. The procedure can reveal the morphology of primary silicon when observed by scanning electron microscope. Experiments are summarized in Figure 3.9.

CHAPTER FOUR

CONTINUOUS COOLING EXPERIMENTS IN A CONCENTRIC CYLINDER RHEOMETER

4.1 Introduction

The work described in this chapter is on the rheological properties and microstructural evolution of semi-solid hypereutectic Al-Si alloys during continuous cooling and solidification. The apparent viscosity of the solidifying semi-solid alloys is measured in a concentric cylinder rheometer at various shear rates. Microstructure of the sheared samples is compared with that of unsheared samples solidified at the same rate.

4.2 Apparent Viscosity during Continuous Cooling

The objective of this part of the work is to study the effect on apparent viscosity of two experimental variables: the shear rate and volume fraction solid. The lists of alloy compositions and corresponding shear rates are shown in Table 4.1. Typical solidification curves of 30, 40, and 50 wt.% Si alloys in the experiments are shown in Figure 4.1. They indicate that the samples were solidified with an undercooling of 10 to 20°C. The undercooling was also detected indirectly by the sudden increase in measured torque. In Figure 4.2 an alloy with 30 wt.%Si develops such an increase at a temperature of 795°C when the primary silicon crystals crystallize from the recalescing liquid. Further cooling under shearing breaks down these primary crystals and the torque decreases. It builds up again when the volume fraction sold silicon increases, as the temperature approaches the eutectic point.

Volume fraction solid silicon is a function of both alloy composition and temperature. Calculated plots of volume fraction solid versus temperature for various

hypereutectic Al-Si alloys are shown in Figure 4.3 in which equilibrium concentration of both phases is assumed. The effect of volume fraction solid on apparent viscosity of continuously cooled samples is shown in Figures 4.4 and 4.5, where apparent viscosities of Al-40 and Al-50 wt.% Si, respectively, are plotted versus g_s, the volume fraction solid. The abscissas are constructed by converting temperature to volume fraction solid using Figure 4.3. Viscosity values when the samples are still liquid and below g_s=0.1 are under the 1% accuracy limit of the transducer. Although the absolute values are not reliable, the operation of mechanisms, such as the initiation of crystallization of the undercooled melt and solid fragmentation can be observed from relative values.

For a given alloy composition and solidification rate, there are two independent variables: shear rate and volume fraction solid. The following analysis is to find the effect of these variables on apparent viscosity, mathematically expressed by:

$$\eta = \eta(\dot{\gamma}, g_s) \tag{4.1}$$

A plot of apparent viscosity versus volume fraction solid at a fixed shear rate, such as in Figures 4.4 and 4.5, indicates that at $0.1<g_s<0.3$ the apparent viscosity follows a simple exponential function of the form:

$$\eta = A\exp(Bg_s) \tag{4.2}$$

which is identical to the last term of equation (2.5), the Thomas expression.

A pair of A and B constants for each continuous cooling experiment may be obtained in this manner. Figure 4.6 is the plot of A versus shear rate, for Al-40 and Al-50 wt.% Si, and Figure 4.7 is the plot of B versus shear rate, for Al-40 and Al-50 wt.% Si slurries. Assuming that both constants are functions of only shear rate, they can be mathematically expressed as:

$$A = A(\dot{\gamma}) \tag{4.3}$$

$$\text{and} \qquad B = B(\dot{\gamma}) \tag{4.4}$$

The equations that fit them best are found to be:

$$A = A'\dot{\gamma}^{a} \tag{4.5}$$

$$\text{and} \qquad B = B'\ln(\dot{\gamma}) + B'' \tag{4.6}$$

where a, B', and B'' are constants

which, replaced into (4.2) yield:

$$\eta = A'\dot{\gamma}^{a}\exp\left(\left[B'\ln(\dot{\gamma}) + B''\right]g_s\right)$$

and after rearrangement:

$$\eta = A'\dot{\gamma}^{a}\dot{\gamma}^{B'g_s}\exp(B''g_s)$$

and finally:

$$\eta = A'\exp(B''g_s)\dot{\gamma}^{(a+B'g_s)} \tag{4.7}$$

The constants for Al-40 and 50 wt.% Si slurries obtained in this work are shown in Table 4.2.

Equation (4.7) can also be transformed to the more familiar power-law expression:

$$\eta = m\dot{\gamma}^{n-1} \tag{2.11}$$

which is widely used to described the apparent viscosity in terms of shear rate at a given volume fraction solid. Power-law constants, m and n, can be related to the empirical constants in equation (4.7) by:

$$m = A' \exp(B'' g_s) \tag{4.8a}$$

$$n - 1 = (a + B' g_s) \tag{4.8b}$$

Table 4.3 shows the values of m and n calculated from equation 4.8 for Al-40 and Al-50 wt.% Si slurries obtained in this work. Figure 4.8 is a plot of the apparent viscosity versus shear rate for Al-40 wt.% Si at various volume fraction solid and Figure 4.9 is a similar plot for Al-50 wt.% Si. For comparison purposes these figures exhibit also plots of equation (4.7) with values of constants from Table 4.3.

Apparent viscosity of semi-solid Al-50 wt.% Si from this work and that of some hypoeutectic aluminum alloys having a non-dendritic structure are plotted for comparison purposes as a function of shear rate at the same volume fraction solid of 0.4 in Figure 4.10.

Although the viscometer used in this experiment can achieve shear rates up to 1,800 s^{-1}, radial and vertical segregation in Al-50 wt.% Si slurries become significant above 400 s^{-1}, resulting in a sharp decrease of measured torque. In the samples with lower shear rates, however, only insignificant vertical segregation can be detected at the upper part and the corner bottom of the crucible, where flow is discontinuous.

4.3 Microstructure

4.3.1 Microstructure of Continuously Cooled Samples without Shearing

Primary silicon in the control samples solidified without shearing at the same cooling rate grows as hexagonal plates radiating from a common center and forming clusters of platelets, as shown in Figure 4.11. The sites of nucleation are on the walls of the crucible and rotor. This morphology predominates in all samples containing silicon from 30 to 50 wt.%. The average particle size is 840, 1420, and 1640 μm for Al-30, 40,

and 50 wt.% Si, respectively. The thickness of the crystals increases with increasing alloy silicon content.

4.3.2 Microstructure of Continuously Cooled Samples under Shearing

The morphology of primary silicon in sheared samples differs from that in conventionally cast samples. Most of the silicon clusters were broken down into individual plates due to shearing, forming roughly elongated or rounded crystals with rounded edges, Figure 4.12. Entrapped liquid pockets inside the crystals are also observed.

The effect of shearing on the primary silicon particle size is shown in Figures 4.13 and 4.14. Primary silicon particle size is plotted versus shear rate for alloys with 30, 40 and 50 wt.% Si. Since the shape of primary silicon in sheared samples is rather irregular, the particle size is defined as the length of the particle, whereas the particle thickness is the width perpendicular to its elongation. Primary silicon particle size in sheared samples was found to be smaller than those in conventionally cast samples. The particle size of the primary silicon in the sheared samples, however, did not change much over the range of shear rate used in this study. The average particle sizes of sheared Al-30, 40, and 50 wt.% Si are 170, 240, and 290 μm, respectively. The particle thickness of the rheocast samples is slightly larger than those observed in conventionally cast samples and shows a slight increase with increasing shear rate.

Six samples from continuous cooling experiments having compositions of 30, 40, and 50 wt.% Si, and sheared at typical rates of 38 and 380 s^{-1} were deep-etched with hydrofluoric acid and observed by scanning electron microscopy. Figure 4.15 shows an agglomerate of two silicon crystals joined along what is believed to be one of the {111} planes. Similar agglomerates were also found in all the observed samples.

4.4 Discussion

4.4.1 The Effect of Shear Rate and Volume Fraction Solid on Apparent Viscosity

Apparent viscosity of Al-40 wt.% Si slurries follows equation (4.2) well at $g_s > 0.1$, Figure 4.4. Below this value it is unstable due to the combination of undercooled crystallization and fragmentation of the silicon which causes it to increase and decrease, respectively. The apparent viscosity of Al-50 wt.% Si, however, start to deviate from equation (4.2) at $g_s \approx 0.3$, Figure 4.5, and is the major cause for the disagreement between the model and experimental data in Figure 4.9. This deviation occurs at a volume fraction solid close to the maximum packing fraction, at which phase saturation occurs for angular plates, Table 2.3.

The empirical model, equation (4.7), contains two independent variables: shear rate and volume fraction solid. A plot of apparent viscosity versus shear rate at a given volume fraction solid is, however, more popular and useful because it clearly shows the shear-thinning behavior of the slurries. The dependence of shear rate exponent n of equation (2.11) on g_s is explicitly reported in equation (4.8b). The fact that any suspension must be Newtonian when $g_s \to 0$ requires that, for power-law suspensions, $n \to 1$ when $g_s \to 0$. It also implies that, in the low volume fraction solid range, the degree of deviation from Newtonian behavior should increase as g_s increases.

The empirical equation (4.7) proposed in this work is identical in form to that proposed by LAXMANAN, et al. [1980] for semi-solid Sn-15 wt.% Pb with $0.3 < g_s < 0.6$, under constant-force compression between parallel plates:

$$\eta = a\exp(bg_s)\dot{\gamma}^{(cg_s+d)} \tag{4.9}$$

where

η: apparent viscosity
g_s: volume fraction solid
$a = 10.5$
$b = 20.6$
$c = 1.78$
$d = -1.39$ for non - dendritic semi - solid Sn - 15 wt.% Pb

Although the final forms of equations of both models are identical, the analytical methods and implications are different. Laxmanan model predicts an increasing shear rate exponent (positive c) with an increasing g_s, implying that the slurries behave more Newtonian-like as g_s increases. In the present work, the shear rate exponent is a decreasing function of g_s (negative B') and Newtonian behavior is predicted at low g_s.

4.4.2 The Effect of Solid Phase Morphology on Apparent Viscosity

The apparent viscosity of hypereutectic Al-Si alloys is of the same order of magnitude as for other non-dendritic slurries at the same volume fraction solid. Their behavior is also shear-thinning and can be explained by considering the potential ability of solid primary silicon to align itself in the liquid in order to reduce flow resistance, as described qualitatively in section 2.3.2. In non-dendritic systems which have spheroidal solid phase particles the flow resistance cannot be reduced by alignment, due to the isometricity of the particles.

Another phenomenon contributing to the observed pseudoplasticity of the semi-solid is the agglomeration of silicon crystals which is not systematically investigated in this work, but is believed to be operating here in the same way as in the non-dendritic semi-solid slurries. Although silicon has a diamond cubic structure and has a lower anisotropy factor than metals it is capable of having various special low mismatch-angle boundaries with extremely low grain boundary energy. At low shear rates these silicon agglomerates can be formed resulting in higher apparent viscosity to the flow. The

degree of agglomeration decreases at a higher shear rate, thus reducing the resistance to the flow. A silicon agglomerate is illustrated in Figure 4.15 and appears to resemble that observed in non-dendritic slurries, as described in section 2.4.2. Agglomerates of these crystals which are formed at high temperature grow larger as the temperature decreases during continuous cooling and appear different from single crystals that grow into oblate spheroids.

The combining effect of particle alignment and migration to low shear rate region creates a non-homogeneous flow and is highly pronounced when the volume fraction solid reaches the maximum packing fraction. This non homogeneous flow results in a deviation from Thomas expression and is shown in Figure 4.16 which is a photomicrograph of a Al-50 wt.% Si sample sheared at 550 s^{-1}. Fine silicon crystals are pushed to the crucible wall leaving large spheroidized agglomerates in the bulk of the annulus. The degree of non-homogeneous flow is also found to be a function of shear rate and is observed only in Al-50 wt.% Si samples in which has a maximum g_s of 0.44.

4.4.3 Microstructure of Continuously Cooled Samples under Shearing

Primary silicon nucleates preferentially on the walls of the crucible and rotor. This is confirmed by the photomicrographs of samples solidified without shearing. For samples solidified with shearing these silicon crystals are swept into the bulk of the liquid due to the imposed flow. Figure 4.2 indicates that the apparent viscosity increases suddenly when the clusters of silicon are introduced into the flowing liquid. Fragmentation of these clusters into individual platelets occurs at the early stage as implied by the drop of apparent viscosity after the sudden increase. This phenomenon agrees with the results of SMITH, et al. [1991] who concluded that the fragmentation mechanism dominates at the early stage of continuous cooling. The microstructure of rheocast Al-30 wt.% Si is also similar to that which they reported for Al-20 wt.% Si.

The results of ARAKANE, et al. [1995], Figure 2.14, indicate that, above a certain shear rate, silicon particle size is independent of shear rate and is a function of mold length and concentric gap. Results from this work exhibit the same trend, implying that, above a certain shear rate, silicon crystals are completely broken and any further increase in shear rate does not yield more fragmentation. The only factor remaining is the concentric gap which constrains the maximum possible particle size Unfortunately, due to instability of mechanical parts, data at shear rate below 40 s^{-1} cannot be obtained in the present apparatus. This is precisely the region where the silicon particle size was shown, in Figure 2.14, to be a function of shear rate.

CHAPTER FIVE

DEFORMATION BEHAVIOR OF REHEATED ALLOYS IN THE SEMI-SOLID STATE

5.1 Introduction

In this part of the investigation rheocast ingots are prepared by a batch rheocasting process taking into account the implications of previous apparent viscosity measurements. Their microstructure is compared with that of ingots solidified in absence of agitation at the same cooling rate. Both types of ingots are, subsequently, reheated to semi-solid temperature of 595°C and their deformation behavior investigated using the cone penetration technique, which provides an apparent yield stress measurement, and a constant-force compression test between two parallel plates.

5.2 Microstructure of Rheocast Alloys

The photomicrographs of rheocast Al-30, 40, and 50 wt.% Si are displayed together with those of corresponding alloys solidified without shearing in Figures 5.1 to 5.3, respectively. The primary silicon in rheocast ingots is substantially refined and changes its morphology from large plates to angular oblate spheroids. The particle size of each ingot is shown in Table 5.1 which indicates that the effect of the agitation during rheocasting on particle size increases with increasing silicon content.

Typical solidification rates of each alloy are shown in Figure 5.4. The average cooling rates are 35, 42, and 51°C/min for Al-30, 40, and 50 wt.% Si, respectively, and are of the same order of magnitude as those in the concentric cylinder experiments.

Figure 5.5 shows the microstructure of Al-40 wt.% Si ingot solidified at 42°C/min. without agitation. It can be seen that primary silicon nucleates preferentially at the wall of the crucible which has the lowest temperature during solidification. The plates grow into the bulk of the sample and coarsen substantially as they reach the center. Figure 5.6 is a photomicrograph of rheocast Al-50 wt.% Si taken near the crucible wall. Primary silicon segregation occurs heavily due to the combined effects of a long solidification time and migration of the silicon to the lowest shear rate region. However, the inner part of the ingot has silicon uniformly distributed and is the region where test specimens are prepared from.

5.3 Yield Stress Measurement of Reheated Alloys by the Cone Penetration Technique

Hypereutectic Al-Si ingots of compositions 30, 35, 40, and 50 wt.% Si solidified without agitation and rheocast ingots of compositions 30, 40, and 50 wt.% Si were sectioned into cubic specimens and tested at 595±5°C. Tables 5.2 and 5.3 show alloy compositions and the corresponding test conditions. Their apparent yield stresses are shown in Figure 5.7 where it was plotted versus volume fraction solid.

Since the cone penetration technique is used here for the first time in the study of semi-solids, results may be different from those observed by other techniques. Direct shear data of Al-4 wt.% Cu by METZ, et al. [1969] are compared with the current cone penetration data of semi-solid Al-4.5 wt.% Cu, in order to validate the latter technique. Figure 5.8 indicates that both data almost coincide with one another.

5.4 Constant-Force Compression Test between Two Parallel Plates

A test specimen was reheated to 595±5°C and compressed between two parallel plates under a constant force. Semi-solid specimens from the ingots solidified without agitation, Table 5.4, remained rigid throughout the 5 min testing time. Fourteen rheocast

specimens of three compositions were compressed under a constant force from 125 and 4000 g, as shown in Table 5.5. The rheocast Al-30 wt.% Si samples were completely crushed between the plates and, thus, results are invalid.

Figure 5.9 is a plot of engineering strain versus time for a semi-solid Al-40 wt.% Si specimen under a constant load of 500 g. Figures 5.10, 5.11, and 5.12 exhibit plots for specimens of the same composition under loads of 1000, 1500, and 4000 g, respectively. The arrows indicate the time when the loads were applied to the specimens. The strain was discontinuous and relatively small under 500 g and lower loads, whereas it was continuous and increased abruptly when the loads exceeded this value. Figure 5.11 is a representation of strain versus time for a test under a load exceeding 500 g. The strain rate was low just after an application of the load. It soon increased significantly only to decrease again to zero a fraction of second later. The specimens were rigid at this point and further holding yielded negligible deformation.

A plot of the ultimate strain, i.e. where the deformation stopped, versus initial stress for Al-40 wt.% is shown in Figure 5.13. For the specimens which exhibited a series of discontinuous stepwise deformation, the values were taken from each step.

The effect of volume fraction solid on deformation is displayed in Figure 5.14 which is an overlay plot of engineering strains versus time for Al-40, and 50 wt.% Si semi-solids under a load of 3000 g. The deformation is slower as the volume fraction solid increases.

The homogeneity of deformation was investigated metallographically on compressed specimens. Although the initial shape of the specimens was that of a hexagonal prism the final shape of specimen with a final strain lower than -0.5 was that of a disk with negligible bulging. Cross-sections at the center of a compressed specimen are shown in Figure 5.15. Volume fraction of silicon in two compressed specimens was

measured and plotted in Figures 5.16 and 5.17 as a function of normalized distance from the center. The plots reveal some radial and vertical segregation of primary silicon.

5.5 Discussion

5.5.1 Primary Silicon Size and Morphology of Rheocast Ingots

Rheocasting is highly effective in refining the primary silicon in hypereutectic alloys up to 50 wt.% Si. The micrograph of an ingot solidified in absence of agitation (Figure 5.5) reveals that silicon nucleates on the wall of the crucible, which is the coolest region, forming clusters of silicon plates which grow into the bulk of the melt. These plates are substantially longer than those observed in the unsheared concentric cylinder specimens for the same compositions and solidification rates, where the silicon growth is constrained by the container configuration. With agitation, these silicon crystals are swept into the bulk of the melt, where they find themselves in a superheated liquid. This may stop the growth of the crystals and cause remelting, as suggested by the roundness of the silicon particles.

Solidification of Al-50 wt.% Si is extremely slow due to its high liquidus temperature. This gives silicon crystals enough time to migrate to the wall and the circular corner at the bottom of the crucible where shear rate is the lowest. Further cooling under agitation cannot remove these segregated crystals and they bond together forming an almost solid network as more silicon is added. The agitation enhances convective transport to this area of silicon which already has a high diffusivity in the liquid phase.

5.5.2 Deformation Behavior of Reheated Ingots in the Semi-Solid State

The appearance of an apparent yield stress in a semi-solid is attributed to the presence of a cohesive network; hence it strongly depends on morphology and volume

fraction solid. Figure 5.8 indicates that reheated hypereutectic Al-Si ingots, solidified in absence of agitation, develop a measurable strength at a volume fraction solid of about 0.2 which is approximately the same as for semi-solid dendritic systems. The effect of solid phase morphology on the onset of plasticity is also demonstrated in Figure 5.8. Non-dendritic semi-solids with smooth spherical particles develop an apparent yield stress when the volume fraction solid reaches about 0.6, the random maximum packing fraction for solid spheres. Semi-solid hypereutectic Al-Si alloys and dendritic alloys solidified without agitation have a more open-structured solid phase and develop such a network at a much lower volume fraction solid.

From the processing point of view, the presence of the yield point in semi-solid metals allows the material to be handled easily during the reheating and charging steps in thixoforming. However, the required flow stress also creates a non-homogeneous flow in the formed parts, especially along the mold wall which is commonly known as stagnant region. The reheated samples with very high yield strength also require more deformation energy than materials with lower yield strength.

Results from cone penetration tests of Al-40 wt.% Si and Al-4 wt.% Cu are compared in Figure 5.18. The deformation mechanism of hypereutectic Al-Si alloys is somewhat different from that of dendritic semi-solid metals. The latter can accommodate strain by both plastic deformation of the solid phase and expulsion of squeezed interdendritic liquid. Silicon in hypereutectic Al-Si semi-solids has a very high strength and virtually no ductility. This explains the steepness of the curve for hypereutectic Al-Si in Figure 5.8 and the discontinuity of the strain observed in compression tests, Figure 5.9, where silicon crystals fracture to accommodate the imposed strain. The breakdown of this cohesive network results in the sudden deformation, as found in a specimen which was compressed with an excessive force.

The highly angular morphology is also potentially responsible for the observed discontinuous deformation. In order to accommodate the imposed strain, the silicon particles have to either slide over each other or break the "necks" that join them. Both are achieved with difficulty compared to the relatively easy plastic deformation and liquid squeezing in rheocast non-dendritic semi-solids. Unlike the case of non-dendritic semi-solid metals which exhibit continuous deformation, continuum mechanics cannot be used to analyze the actual deformation, due to the presence of this discontinuity.

The early deformation stage during a compression test involves breaking of such network. The compression continues, for a specimen with a load under about 500 g, for a very short time and comes to a stop when a new network is built up again. This new network forms when angular and open-shaped silicon particles come into contact with one another during the flow. For a specimen with a load exceeding 500 g the resulting shear stress is sufficient to overcome such friction and a relatively easy flow occurs in the intermediate stage.

The last stage of compression in every specimen consists of a deceleration of the rate of deformation to zero. Specimens with a relatively small load came to a stop when the stress is not sufficient to break the network, while those under an excessive stress stopped when the stagnant zones overlapped with each other. This is confirmed in Figures 5.13 and 5.19 which indicate that the final stress and strain are almost constant at a load exceeding 500 g. The slight increase of the final stress might be due to the inertia effect of the upper plate. The phenomenon is analogous to systems with a metallic primary phase, both dendritic and non-dendritic, in which the deformation stops or proceeds only under extremely high stress when solid phase is compacted.

The uniformity of deformation is illustrated in Figures 5.15 to 5.17. At both $\tilde{h} = 0$ and $\tilde{h} \approx 1$ the primary silicon volume fraction increases after compression for a radius in the range of $0 < r < r_0$, Figure 5.16. At $r > r_0$ the volume fraction solid

decreases with the distance from the center and is the region where radial flow occurred. The result is confirmed with visual inspection of the specimen after compression; traces of oxide skin remained intact on both sides of the specimens implying a non-slip boundary condition. The compression, thus, consists of both radial flow and the compaction of the stagnant central region. A deformation at lower final strain is shown in Figure 5.17 in which Al-50 wt.% Si specimen was compressed to $e = -0.535$ for comparison purposes. The uniformity of deformation is comparable to that observed in non-dendritic Sn-15 wt.% Pb at the same strain (SUERY, et al. [1982]). Specimen bursting and liquid exudation, as reported by LAXMANAN, et al. [1980], was not observed.

CHAPTER SIX

SUMMARY AND CONCLUSIONS

The rheological properties of Al-30, 40, and 50 wt.% Si alloys were investigated in a Searle-type rheometer simulating continuous cooling in rheocasting. Process variables in the investigation were alloy composition and shear rate. The microstructure after shearing was observed and interpreted in comparison with that of specimens which were similarly solidified, but without shearing.

A rheocasting apparatus was used to cast ingots of compositions 30, 40, and 50 wt.% Si. The rheocast ingots were then reheated into the semi-solid range and evaluated using both the constant-force cone penetration and the parallel plate methods. Their deformation behavior and microstructure were compared with those of ingots solidified without agitation.

The conclusions are the following:

(1) Apparent viscosity of solidifying semi-solid hypereutectic aluminum-silicon alloys having volume fractions solid from 0.1 to 0.4 depends on shear rate and can be represented by a pseudoplastic power-law. Apparent viscosity at a given shear rate increases with increasing volume fraction solid and can be represented by the last term of the Thomas expression. An empirical equation relating viscosity to both $\dot{\gamma}$, the shear rate, and g_s, the volume fraction solid is:

$$\eta = A' \exp(B'' g_s) \dot{\gamma}^{(a+B' g_s)}$$

where A', a, B', and, B'' are constants.

(2) Viscosities at a given shear rate and fraction solid are closely comparable for the two aluminum-silicon alloys studied, although the higher silicon alloy appears to have a slightly higher shear rate dependence at higher fractions solid.

(3) The pseudoplasticity observed is due to a combination of increasing particle alignment and decreasing particle agglomeration at higher shear rates.

(4) Shear rates up to 100 s^{-1} reduce primary silicon particle size by about an order of magnitude; higher shear rates have little further effect.

(5) Viscosities of hypereutectic Al-Si slurries at a given fraction solid and shear rate are closely comparable to those obtained in a wide range of hypoeutectic aluminum alloys. It is thus concluded that these hypereutectic alloys can be cast commercially by processes, now used to "rheocast" semi-solid hypoeutectic alloys.

(6) A "cone method" used by others to measure the "yield stress" of materials such as butter and grease was adopted to study semi-solid alloys. Test results show a large difference in yield stress in the semi-solid state of the alloy studied, depending on whether or not the alloy was sheared during solidification. It is also found that results for a semi-solid hypoeutectic alloy are quantitatively similar to those from an earlier, more difficult experiment to perform.

(7) Deformation of reheated semi-solid Al-Si under compression proceeds in a manner quite different from that of hypoeutectic alloys, presumably because of the hard non-deformable nature of silicon. On application of a given load, rapid deformation take place to a final strain, with little further deformation thereafter. Strain increases linearly with initial applied load up to about one kilogram.

(8) Deformation is found to be relatively homogeneous (i.e. solid silicon particles, as well as the liquid moved during deformation); cracking did not occur and macrosegregation

was low. Thus, "thixoforming" of this alloy should be possible, although probably more difficult than of the semi-solid hypoeutectic alloys.

(9) Hypereutectic Al-Si alloys up to about 22 wt.% Si are employed in limited amounts for applications where improved wear resistance, low thermal expansion, and weight saving are desired. These alloys are difficult to cast because of their high liquidus temperature and wide solidification range. This thesis demonstrates the practicality of forming hypereutectic Al-Si alloys with silicon content at least up to 50 wt.% Si at a temperature as low as the Al-Si eutectic temperature.

CHAPTER SEVEN

SUGGESTIONS FOR FUTURE RESEARCH

(1) Isothermal experiment:

Behavior of the semi-solid slurries during isothermal holding is critical in understanding the nature of semi-solid metals. In the present work there is a limitation due to the heating source. Induction heating creates unwanted secondary flow which complicates the analysis. A resistance heating furnace should be used for the isothermal investigation.

(2) Rheocasting experiment:

The effect of variables on the microstructure of the rheocast alloys is proposed. The possible variables are the solidification rate, agitation speed, and the temperature at which agitation stops. The effect of some elements such as phosphorus on the microstructure should also be investigated.

(3) Constant- or prescribed-speed compression test:

The present setup can provide data only for a constant-force compression condition. The data at higher compression strain can only be obtained by compression under constant speed or constant strain rate. The apparent yield stress can also be obtained directly from stress-strain curve under such experiments.

APPENDICES

APPENDIX 1. VISCOMETRY

A.1.1 Rotating Concentric Cylinders

Figure A.1 shows a typical concentric cylinder rheometer. The flow in its annulus is termed steady tangential annular flow because it is unidirectional and velocity vector, v_i, has only one component in the tangential direction. When secondary flow is absent, the velocity vector is described by:

$$\begin{aligned} v_\theta &= v_\theta(r) \\ v_r &= 0 \\ v_z &= 0 \end{aligned} \qquad \text{(A.1)}$$

Secondary flow known as Taylor vortex can occur at high angular velocity. This flow is the result of inertia effect and can occur in any material even Newtonian-fluids. For concentric cylinder geometry with rotating inner cylinder the stability criterion is given by TAYLOR [1923] as:

$$\mathrm{Re}_{critical} = 41.3\left\{\frac{R_2}{(R_2 - R_1)}\right\}^{1/2} \qquad \text{(A.2)}$$

When the Reynolds number for the flow in concentric rheometer, Re, which is given as:

$$\mathrm{Re} = WR_1\frac{(R_2 - R_1)}{\eta} \qquad \text{(A.3)}$$

is more than the critical value, equation (A.1) is no longer valid and the velocity vector has three non-zero components. The flow pattern is demonstrated in Figure A.2. The

effect, in any case, is an increase in applied torque at a given rate of rotation (SCHLICHTING [1979]).

Special case occurs when the ratio of inner radius to outer radius, $\beta = R_1 / R_2$, is close to 1. The flow between this narrow gap is similar to the flow between two flat plates when one is moving parallel to the other and is also termed Couette flow. The effect at the ends of the cylinder may be neglected for a set-up which have relatively long cylinder. When these conditions are satisfied, it can be shown that the apparent viscosity is equal to

$$\eta(\dot{\gamma}) = \frac{T(R_2 - R_1)}{2\pi R_1^3 H |W_2 - W_1|} \tag{A.4}$$

and the shear rate is expressed as

$$\dot{\gamma} = \frac{|W_2 - W_1| R_1}{R_2 - R_1} \tag{A.5}$$

Two extreme cases are Couette rheometer and Searle rheometer. The Couette rheometer has a rotating crucible with a stationary inner cylinder while vise-versa in the Searle rheometer. There are concentric cylinder rheometers that both cylinders are rotating. There is no difference as far as the secondary flow is neglected, only the relative angular velocity term enters into the above equation. The Couette type has a higher stability limit but is more difficult to construct than the Searle type. The Searle rheometer which has a torque measuring device attached on the inner cylinder side is also suffered from the stability of mechanical parts because the torque measuring device has to be connected in series with the rotating shaft. This impairs the sensitivity at low torque level.

In the absence of secondary flow, the flow inside the annulus is uniform and the velocity is only a function of radius only. This is true as long as the interested region is

far from the bottom end and the free surface opening on the top. In order to correct this end effect, it is common that the end of the inner rotor assumes cone-shaped end as in Figure A.3. When the outer cylinder is stationary and the cone angle is satisfied with the condition:

$$\vartheta_0 = \frac{R_2 - R_1}{R_1} \tag{A.6}$$

the shear rate will be uniform throughout the bottom end. The expression for apparent viscosity is modified into

$$\eta(\dot{\gamma}) = \frac{T(R_2 - R_1)}{2\pi R_1^3 H\left[1 + (R_1 / 3H)\right] W_1} \tag{A.7}$$

Equations (A.4) to (A.7) are valid only for an ideal concentric rheometer with "very narrow gap". For rheometer with a finite gap width, it is possible to determine the flow curve using derivations by one of three existing solutions proposed by MOONEY [1931], KRIEGER, et al. [1953], and THORNTON [1953]. However, these solutions are extremely complex and usually have the form of convergent series. To obtain a single value of the apparent viscosity, a large number of experiments must be carried out to determine various correction terms.

Solutions for known forms of the flow curve also exist for materials with a simple behavior, such as Newtonian and power-law. Even for power-law behavior, the solution is still complicated and requires correction terms unavailable from such data as continuous cooling curve, when viscosity varies with time of solidification. In order to circumvent this, investigators usually neglect this "facts" and use a set of equations derived for a Newtonian fluid in finite gap concentric rheometer which has the form:

Viscosity:

$$\mu = \frac{T}{4\pi H W_1}\left(\frac{1}{R_1^2} - \frac{1}{R_2^2}\right) \tag{A.8}$$

Shear rate at arbitrary radius r:

$$\dot{\gamma} = \frac{2/r^2}{(1/R_1^2)-(1/R_2^2)} W_1 \tag{A.9}$$

Average shear rate:

$$\dot{\gamma}_{average} = \frac{2W_1}{(R_2 - R_1)\left(\frac{1}{R_1} + \frac{1}{R_2}\right)} \tag{A.10}$$

A.1.2 Constant Force Compression

The compressive plastometer or sometimes known as parallel plates viscometer is very versatile in handling fluids which have relatively high viscosity. Its history deals with the measurement of unvalcanized rubber stocks and asphaltic materials and has been finally adopted to polymeric liquids. The major drawback of this viscometer is that the flow is not homogeneous and a constitutive model must be presumed. Exact solutions relating stress tensor to shear rate are available for few time-independent basic models such as Newtonian, power-law and some viscoelastic fluids. Another serious drawback is that the deformation rate has to be very slow.

The test material is in the form of a thin disk sitting between parallel plates. There are two configurations. In one configuration, the test sample is smaller than the plates and remains inside the gap throughout the test, as shown in Figure A.4. Another configuration has smaller plates and the test sample completely fills the gap. The test material is allowed to be squeezed out of the gap since the beginning of the test, as shown in Figure A.5.

Solutions for Newtonian Fluids

A sample is placed in the gap separated by a distance $2h_0$. A constant force F is applied to each plate. If the plates squeeze the test sample very slowly, the inertia effect can be neglected. For Newtonian fluids, it can be shown that

(a) Test sample is smaller than the plates

The compressive force acting on each plates can be represented by

$$F = \frac{3\pi R^4 \mu\left(-\dot{h}\right)}{2h^3} \tag{A.11}$$

By integrating the above expression, an equation relating the height of the sample as a function of time and the Newtonian viscosity is obtained:

$$\frac{1}{h^4} - \frac{1}{h_0^4} = \frac{8\pi Ft}{3\mu\left(\pi R_0^2 h_0\right)^2} \tag{A.12}$$

(b) Test sample completely fills the gap

The compressive force acting on each plate is also related to the compression speed by equation (A.11):

$$F = \frac{3\pi R^4 \mu\left(-\dot{h}\right)}{2h^3} \tag{A.11}$$

Solve this differential equation for $h(t)$ and the expression for h as a function of force and time is obtained as:

$$\frac{1}{h^2} - \frac{1}{h_0^2} = \frac{4Ft}{3\pi R^4 \mu} \tag{A.13}$$

The common way to obtain the viscosity is to plot the first term on the left-handed side of equation (A.12) or (A.13) versus time. The viscosity can be calculated from the slope of the plot.

Solution for Power-Law Fluids

The compressive force acting on each plate at any moment is given as (SCOTT [1931]):

$$F = \frac{(-\dot{h})^n}{h^{2n+1}} \left(\frac{2n+1}{2n} \right) \frac{2\pi m R^{n+3}}{(n+3)} \tag{A.14}$$

There are two cases, as with Newtonian fluids. One is when the sample is smaller than the gap, the other is when the test sample completely fills the gap.

(a) Test sample is smaller than the plates

Equation (A.14) is solved and, after integration, an expression relating the height of the sample to power-law parameters is obtained as (LEIDER, et al. [1974]):

$$\left(\frac{1}{h} \right)^{(3n+5)/2n} - \left(\frac{1}{h_0} \right)^{(3n+5)/2n} = \left(\frac{3n+5}{2n} \right) k t h_0^{-[(n+3)/2n]} \tag{A.15}$$

$$\text{where} \quad k = \left[\left(\frac{2n}{2n+1} \right)^n \frac{4F}{\pi (2R_0)^{n+3} m} (n+3) \right]^{1/n} \tag{A.16}$$

(b) Test sample completely fills the gap

The equation (A.14) is integrated from $t = 0$ to $t = t_{1/2}$, the half time for the sample to be compressed to half of its initial height, which is given as:

$$\frac{t_{1/2}}{n} = K_n \left(\frac{\pi R^2 m}{F} \right)^{1/n} \left(\frac{R}{h_0} \right)^{1+(1/n)} \tag{A.17}$$

where $K_n = \left(\frac{2^{1+(1/n)}-1}{2n}\right)\left(\frac{2n+1}{n+1}\right)\left(\frac{1}{n+3}\right)^{1/n}$ (A.18)

APPENDIX 2. PLASTOMETRY: CONE PENETRATION

Whether materials really have yield point or not is currently under debate. The Bingham model which is regarded as the basic model for viscoplastic materials has been questioned for the past 30 years (BARNES, et al. [1985], CHENG [1986], HARNETT, et al. [1989], and SCHURZ [1990]) with the increasing improvement in measuring techniques. Modern apparatus that can detect stress at very low shear rate (lower than $10^{-4}\ s^{-1}$) reveals decreasing values of yield points when shear rate decreases to such value. It is, however, indispensable from the engineering point of view to consider that some materials possess yield points with respect to the time scale of observation.

There are many techniques available for viscoplastic materials. Reviews on the subject can be found in NGUYEN, et al. [1983] and [1992], KEENTOK [1982], and YOSHIMURA, et al. [1987]. As in the case of viscous materials, only some techniques are acceptable for suspensions and mixtures. Segregation and non-uniformity are the major factors determining the test methods.

The cone penetration technique is based on the immersion of a cone into a viscoplastic material under a constant force as in Figure A.6. REBINDER [1941] and [1944] derived a pressure distribution function along the surface of the cone after the immersion is complete and in equilibrium. By integrating this function, the yield stress is given by

$$\tau_0 = K\frac{F}{h^2} \tag{A.20}$$

$$\text{where} \quad K = \frac{1}{\pi}\cos^2\alpha\cot\alpha \tag{A.21}$$

AGRANAT, et al. [1957] later modified the geometric constant K by using slip-line field method to find more accurate pressure distribution and arrived at

$$\begin{aligned}\frac{1}{K} = \pi\tan^2\alpha\Bigg\{&2\alpha - 2(\sin\alpha+1)^2\ln\frac{\sin\alpha}{\sin\alpha+1} + \\ &+\left[1-\cot\left(\frac{\pi}{4}+\frac{\alpha}{2}\right)\right](2\sin\alpha+1)^2\ln\frac{2\sin\alpha}{2\sin\alpha+1} + \\ &+\left[\cot\left(\frac{\pi}{4}+\frac{\alpha}{2}\right)-\cot\left(\frac{\pi}{4}+\alpha\right)\right]\cot^2\left(\frac{\pi}{4}-\alpha\right)\ln\frac{2}{\cot\alpha+1} + \\ &+\cot\left(\frac{\pi}{4}+\frac{\alpha}{2}\right)\left[\cot\left(\frac{\pi}{4}-\alpha\right)-(2\sin\alpha+1)\right]\Bigg\}\end{aligned} \tag{A.22}$$

This method has an advantage over other techniques because it can be performed on specimens of any sizes and geometry as long as the surface is flat and the sizes is large enough compared to the deformation field. It has been widely used in characterization of food products such as butter DIXON, et al. [1979] due to its simplicity. It is, however, considered by many theoreticians to be very crude and unreliable, because the cone takes a certain amount of time to reach equilibrium and the incorrect depth of penetration can be measured in this manner. When the test specimen is an ideal viscoplastic material, the cone should reach the equilibrium and stop there. When the displacement sensor has high resolution, the cone can sometimes be detected continuing the immersion into specimen and the equilibrium is hardly reached. This effect is more pronounced when the specimen is not truly viscoplastic or when it is only "viscous."

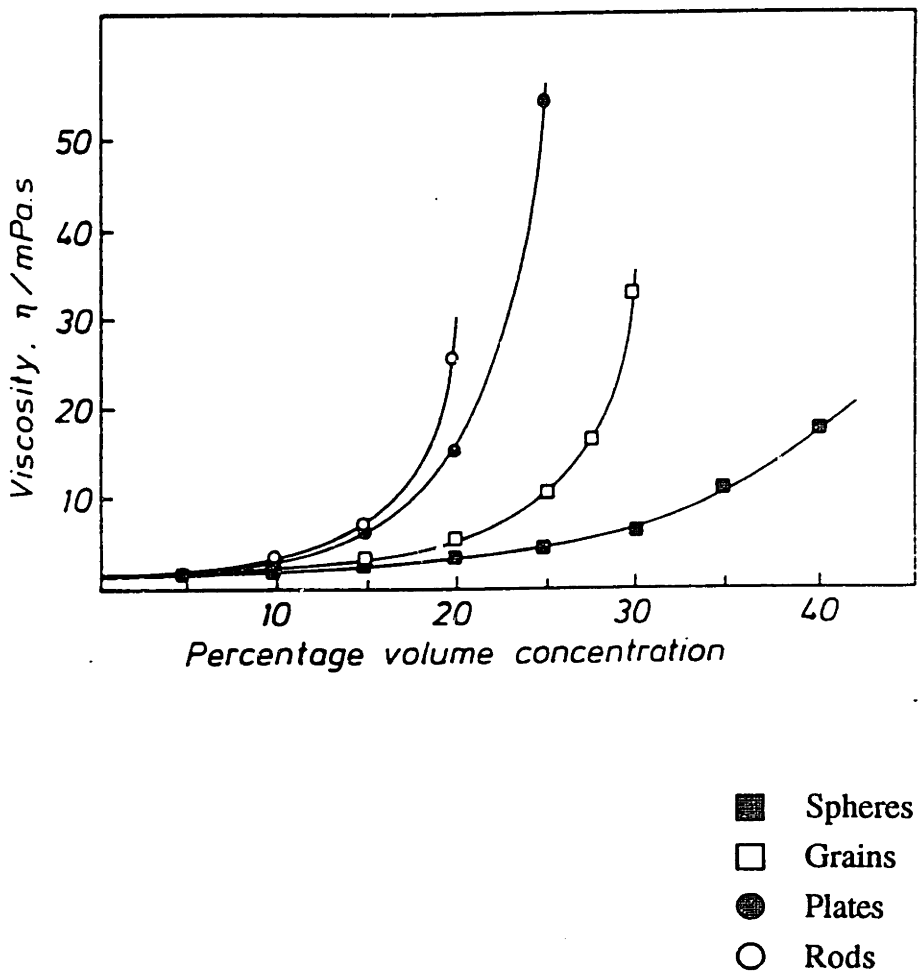

Figure 2.1 Dependence of the apparent viscosity of differently shaped particles in water on volume fraction solid at a shear rate of $300s^{-1}$ from BARNES, et al. [1981]

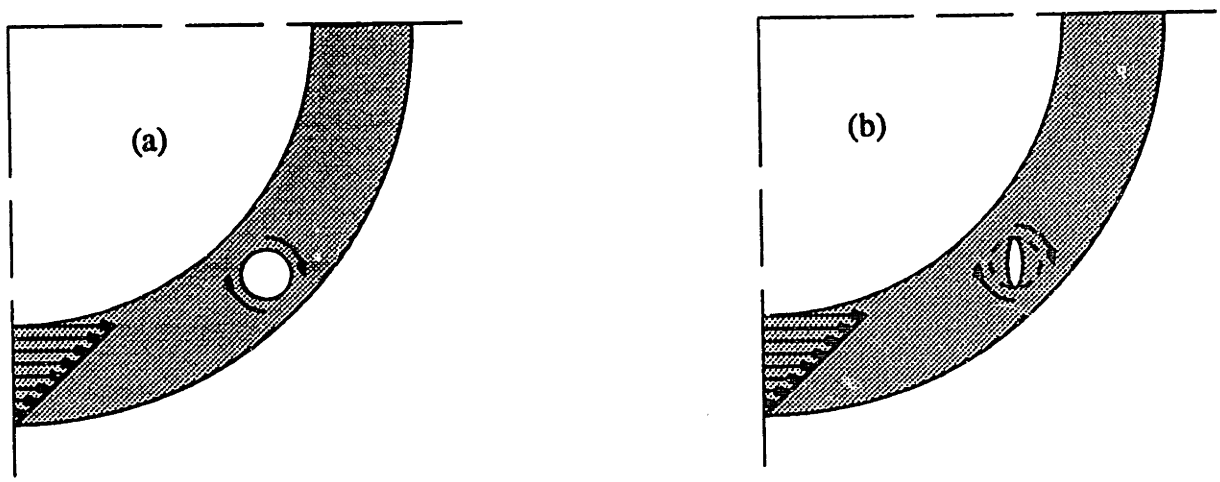

Figure 2.2 Schematic representation of the angular momentum on a particle suspended in the annulus of concentric cylinder rheometer. (a) Spheroidal particle. (b) Disc-shaped particle.

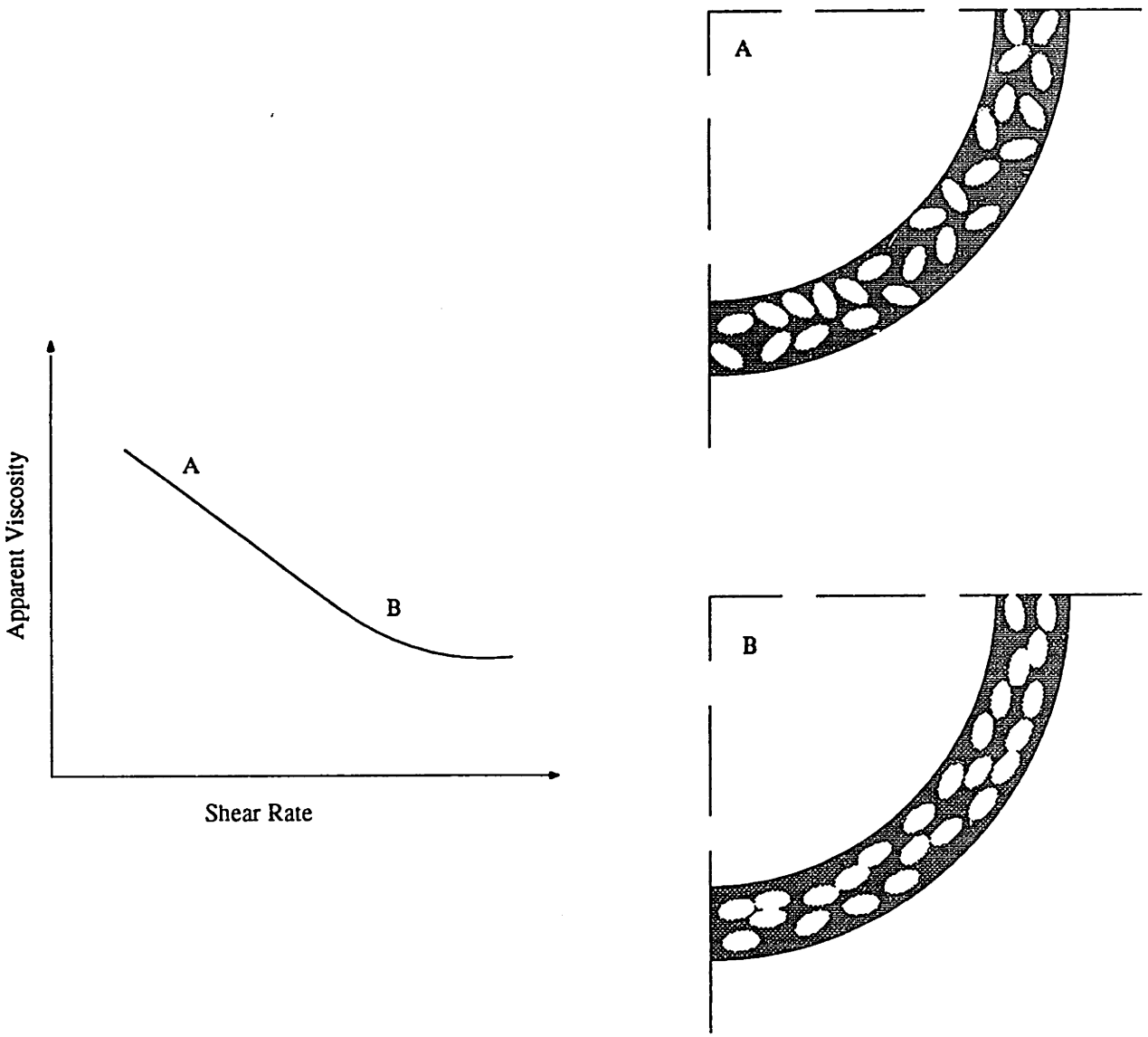

Figure 2.3 Schematic representation of viscosity versus shear rate and its corresponding microstructure with shear-thinning response.

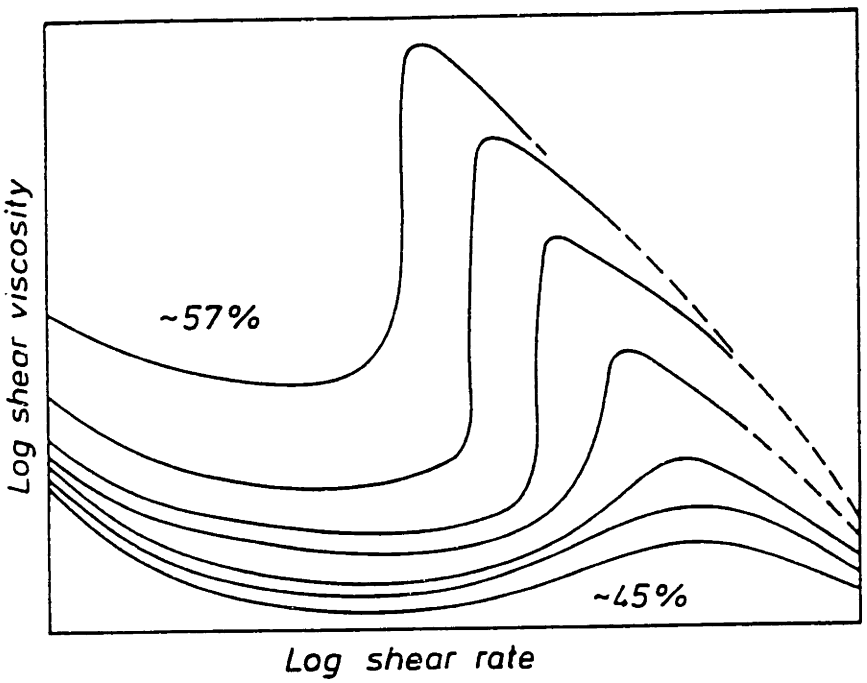

Figure 2.4 Schematic representation of viscosity versus shear rate for shear-thickening systems, with volume fraction solid as parameter from BARNES, et al. [1989]

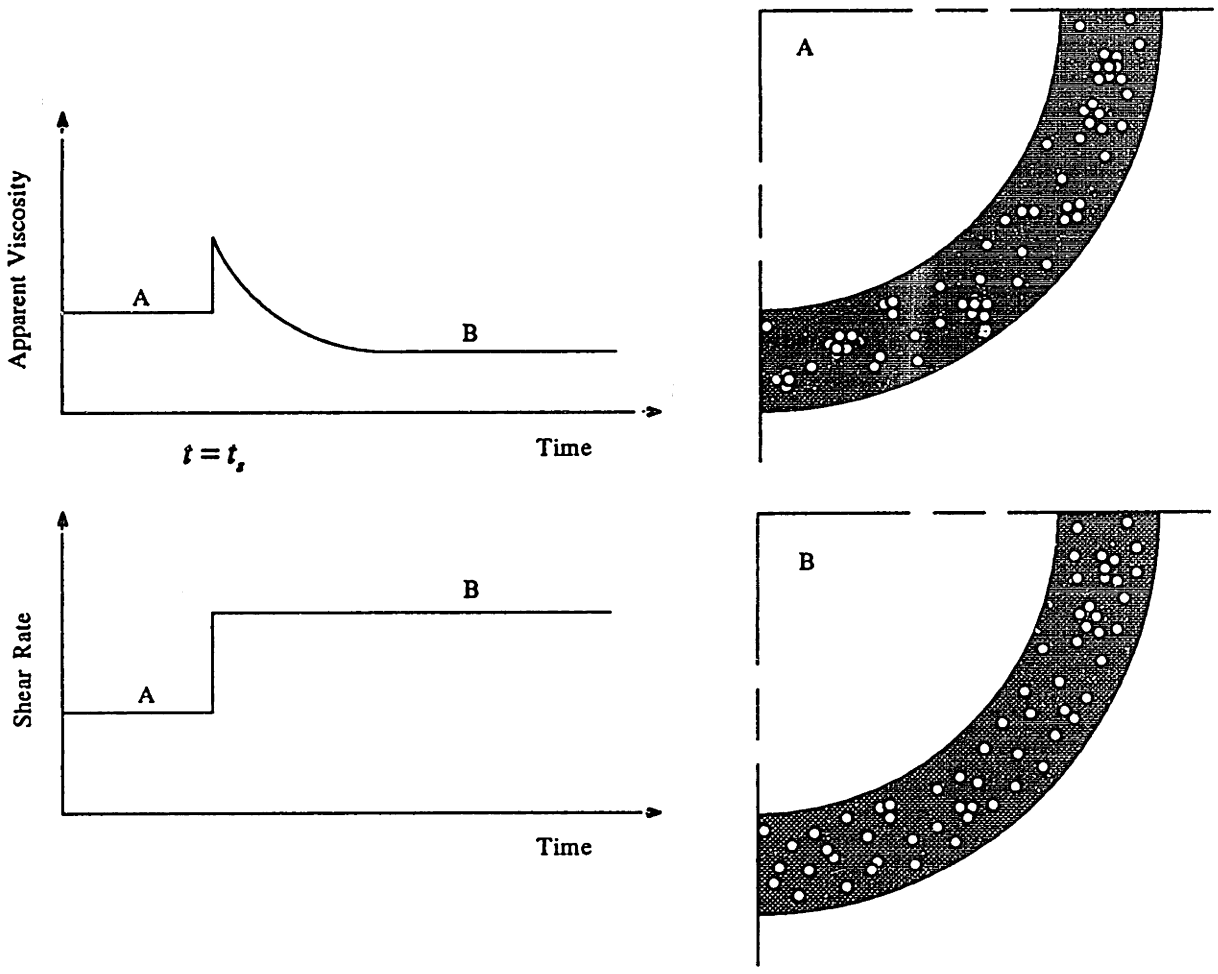

Figure 2.5 Schematic representation of viscosity versus time for a thixotropic system with corresponding microstructure. Shear rate is changed abruptly to higher rate at $t=t_s$.

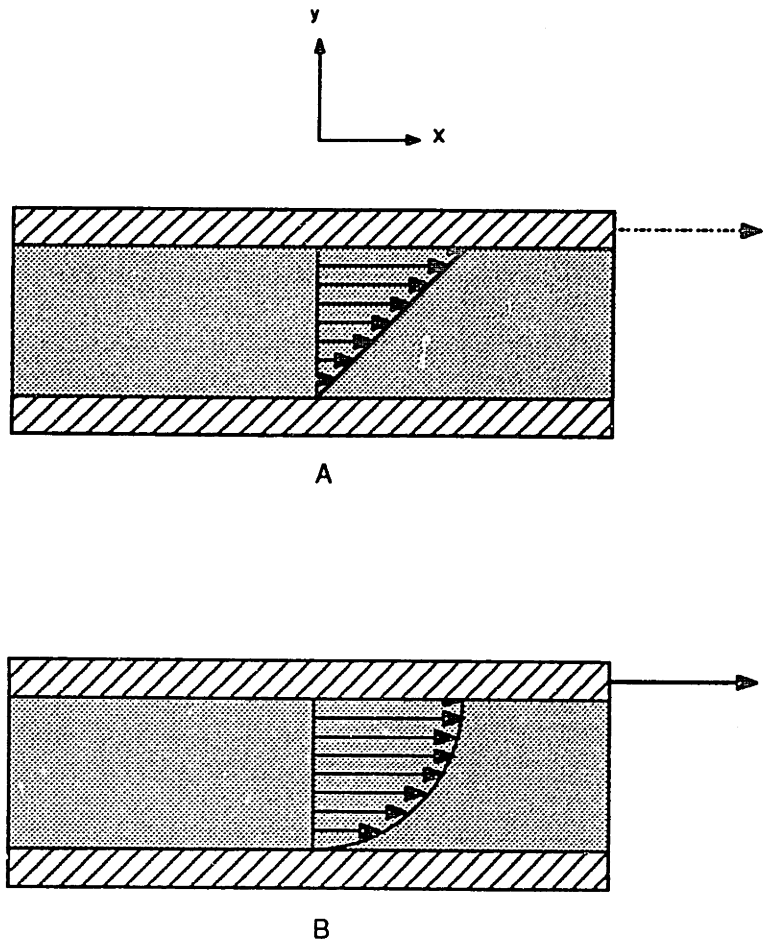

Figure 2.6 Velocity field of fluids when the upper plate is moving at a constant velocity. (a) Newtonian fluid. (b) Non-linear fluid.

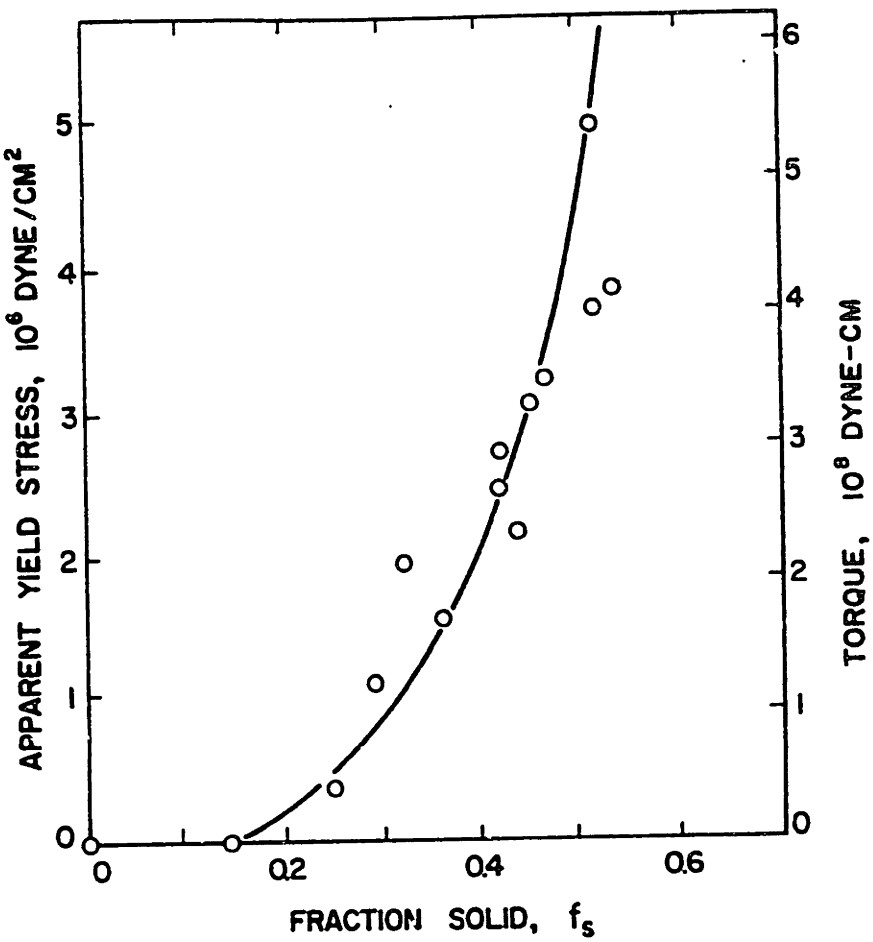

Figure 2.7 Apparent yield stress and torque versus volume fraction solid. Samples were cooled to f_s before shearing. Cooling rate was 20°C/hr. Rotation speed was 0.16 rpm (From SPENCER, et al. [1972].)

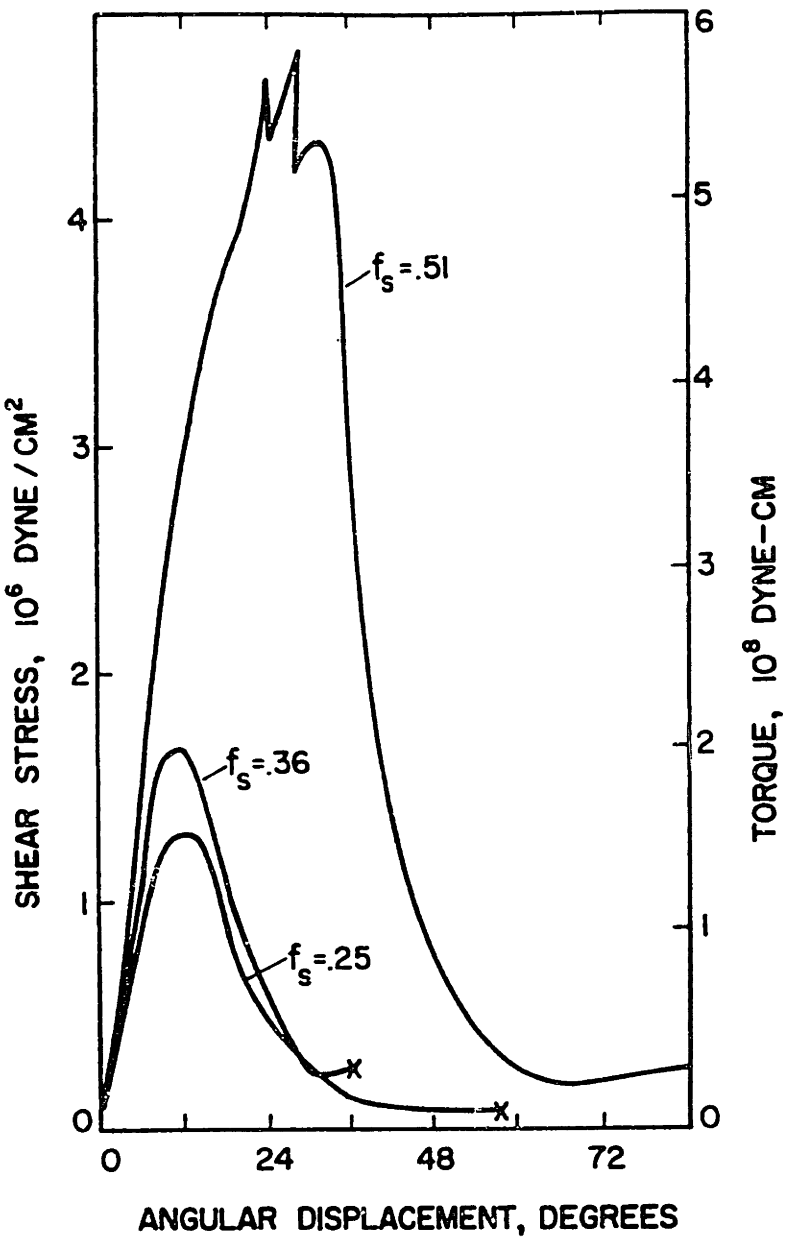

Figure 2.8 Shear stress and torque versus angular displacement for various volume fraction solid. Samples were cooled to f_s before shearing. Cooling rate was 20°C/hr. Rotation was 0.16 rpm (From SPENCER, et al. [1972].)

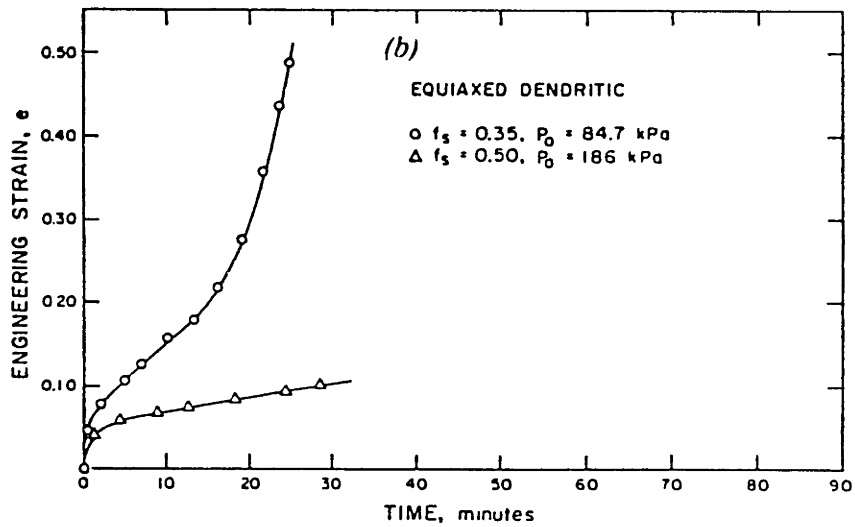

Figure 2.9 Engineering compressive strain versus time for two equiaxed dendritic Sn-15 wt.% Pb specimens at different loads (from LAXMANAN, et al. [1980]).

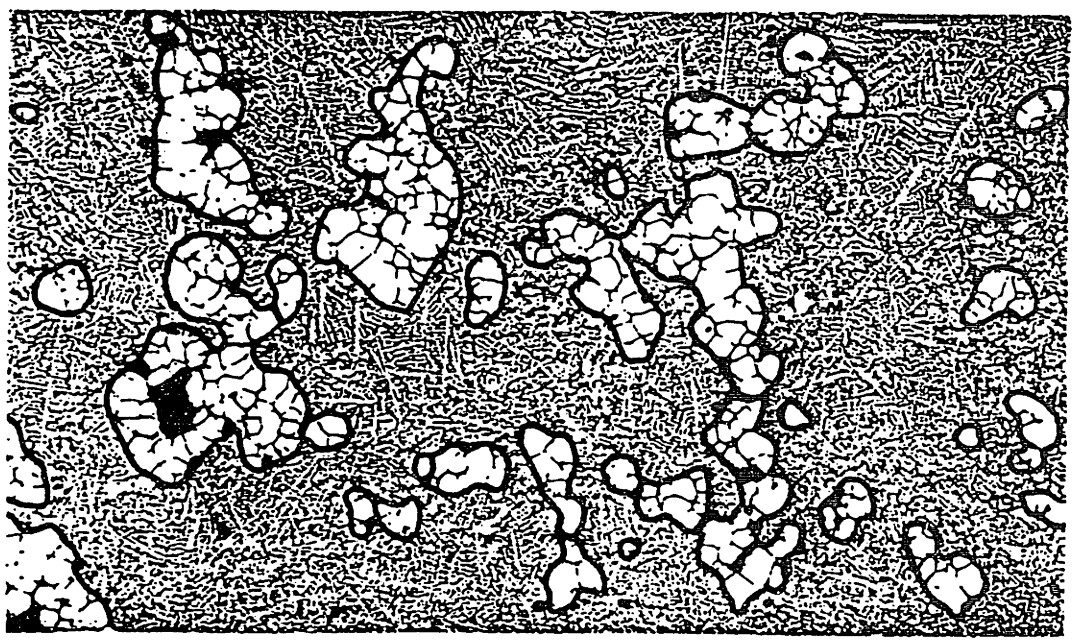

Figure 2.10 Photomicrograph of Al-6.5 wt.% Si continuously cooled at 4.5°C/min under shearing at $900s^{-1}$. Primary solid phase forms agglomerates.

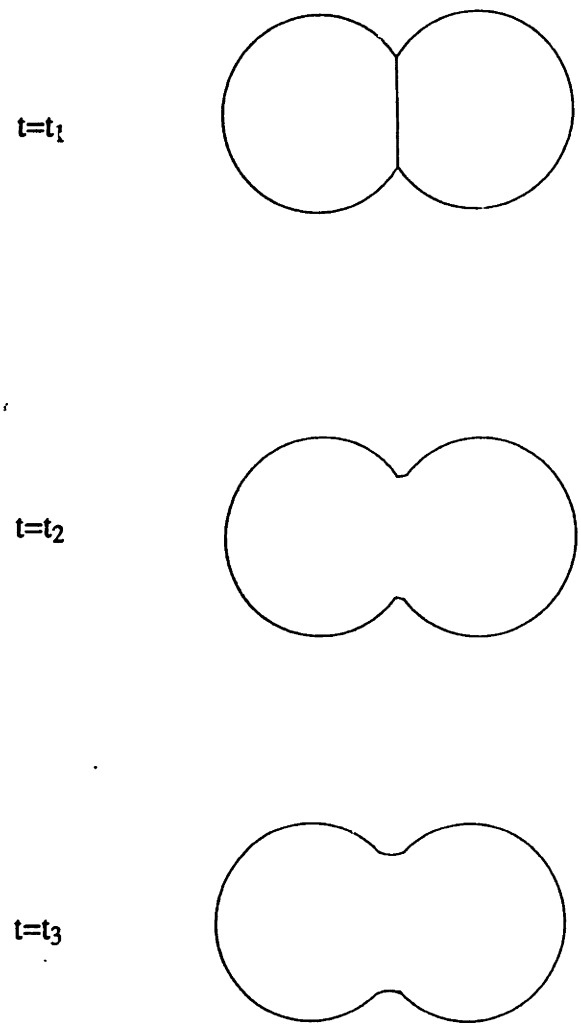

Figure 2.11 A schematic representation of the coalescence of two particles forming a "neck." The neck region becomes larger with time ($t_3>t_2>t_1$.)

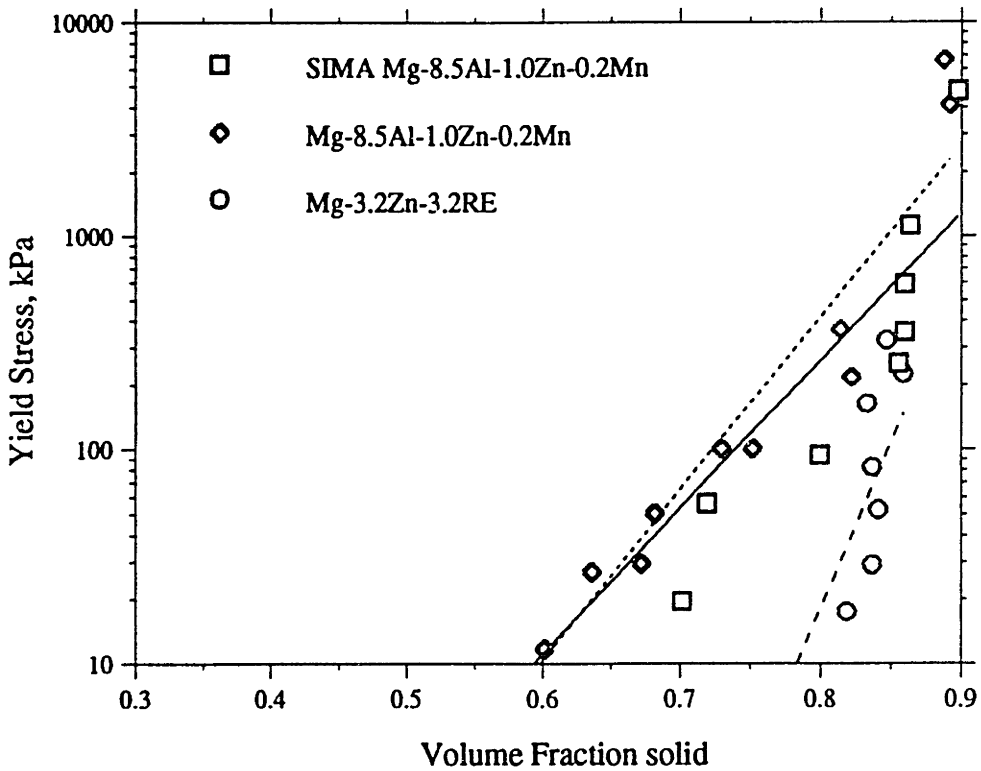

Figure 2.12 Yield stress of three semi-solid magnesium alloys with a non-dendritic structure versus volume fraction solid (from SANNES, et al. [1994]).

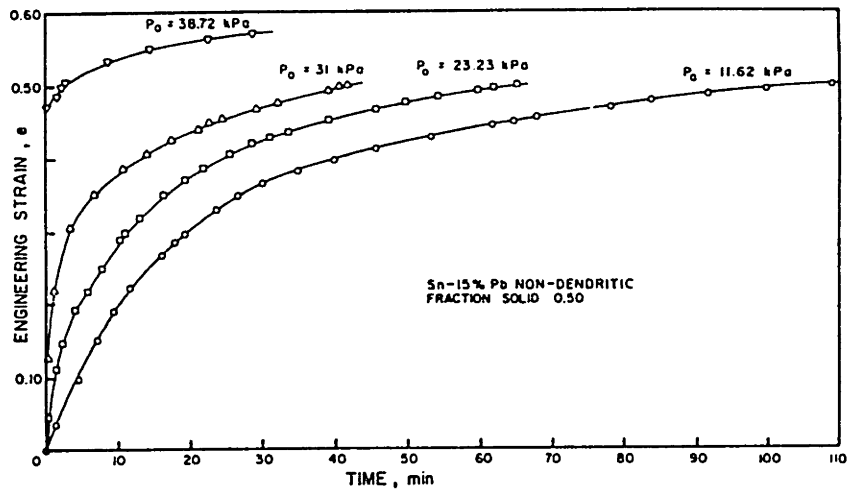

Figure 2.13 Engineering compressive strain versus time for four non-dendritic Sn-15 wt.% Pb specimens at various loads (from LAXMANAN, et al. [1980]).

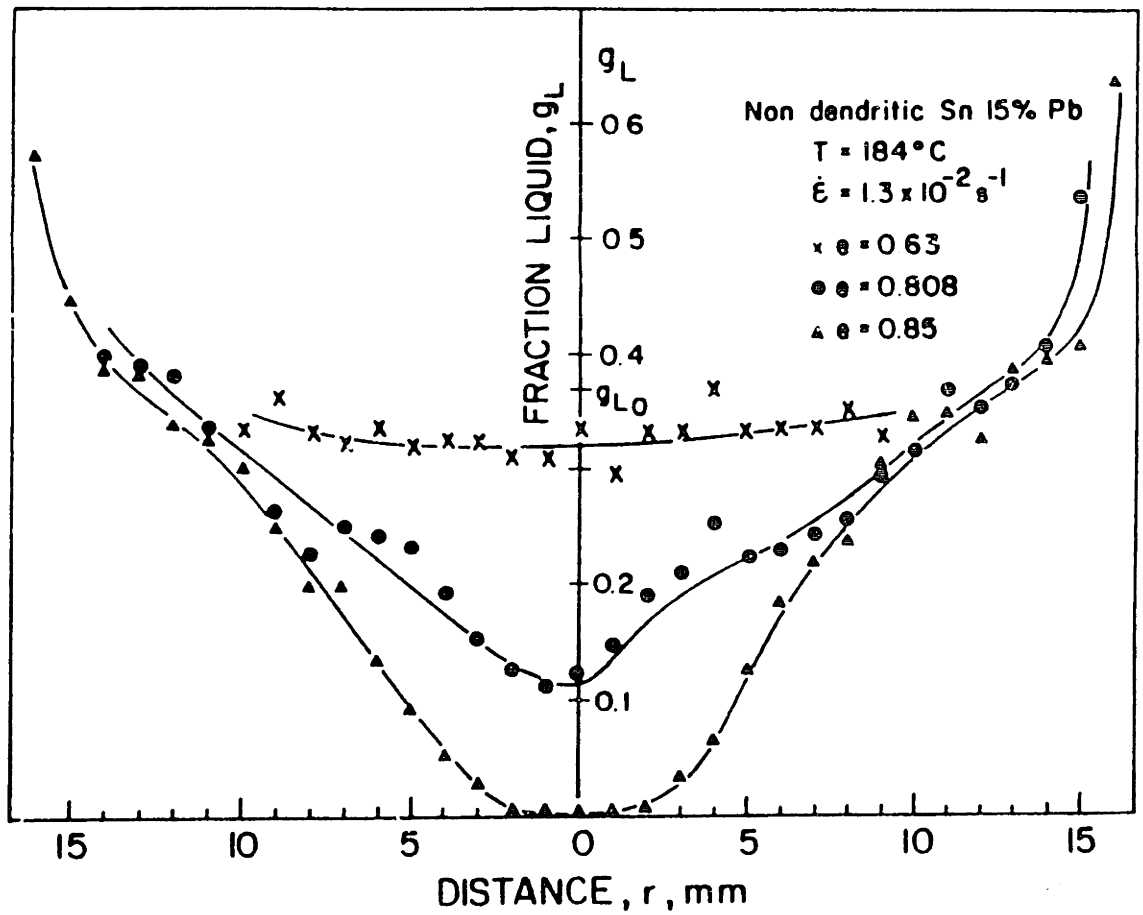

Figure 2.14 Volume fraction liquid versus distance along the radius of a non-dendritic Sn-15 wt.% Pb specimen after compression at various engineering strain (from SUERY, et al. [1982]).

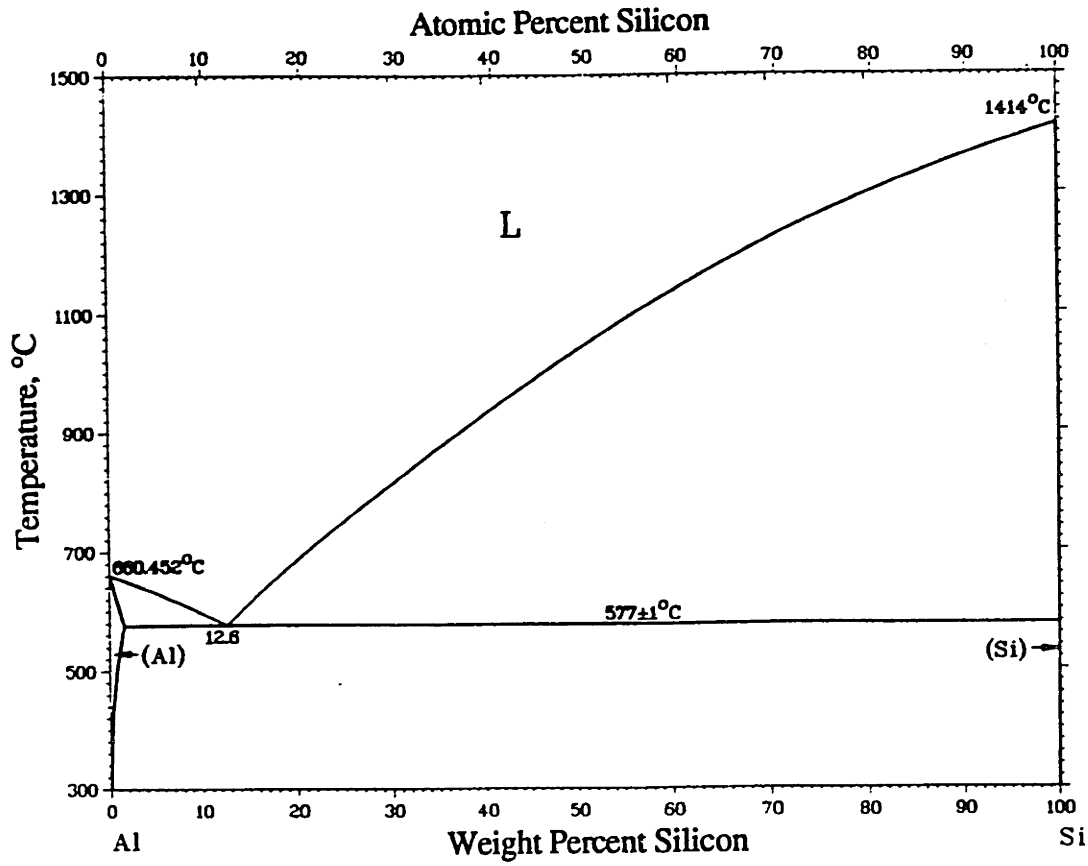

Figure 2.15 Phase equilibrium diagram for Al-Si system from MURRAY, et al. [1984].

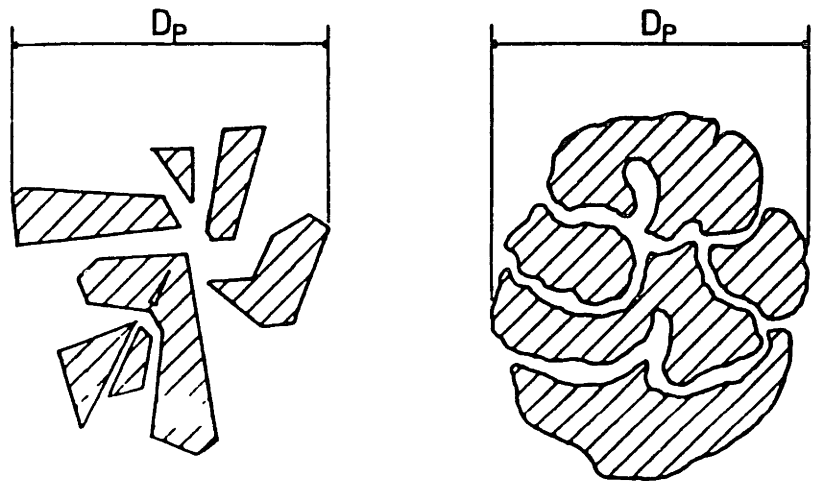

Fig. 8—Typical shapes of primary silicon particles in stirred slurry (*a*) at an early stage of solidification and (*b*) at a later stage, near the eutectic temperature. Volume, V_p, calculated from D is slightly overestimated in (b) but substantially in error in (a).

Figure 2.16 Schematic representation of microstructural evolution of Al-19 wt.% Si after solidified in the present of vigorous agitation from SMITH, et al. [1991].

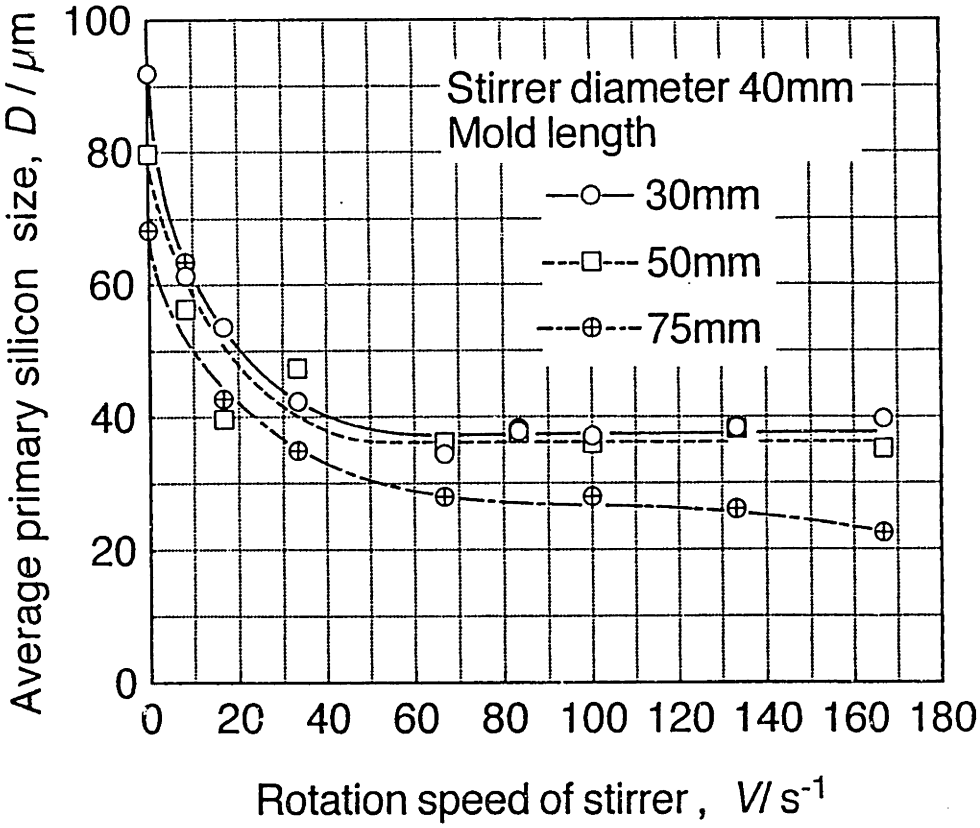

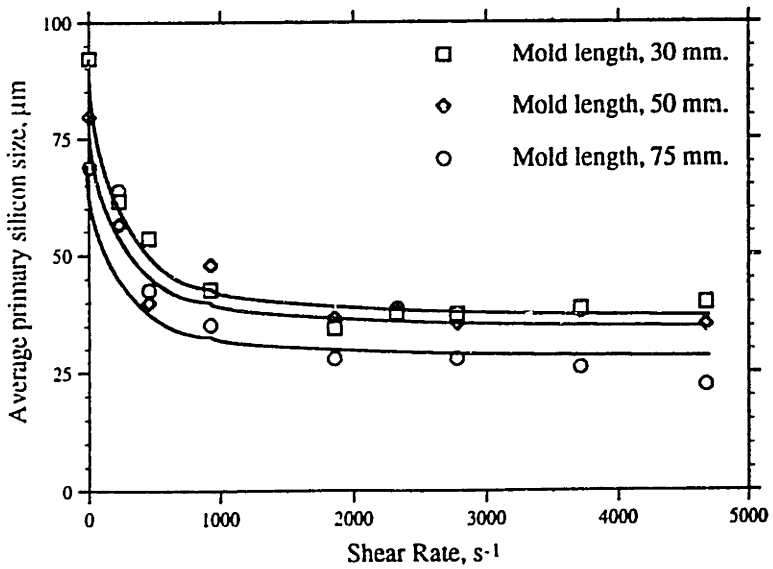

Figure 2.17 (a) Average primary silicon size of Al-20 wt.% Si versus rotation speed of stirrer from ARAKANE, et al. [1995]. (b) A reconstructed plot in terms of shear rate.

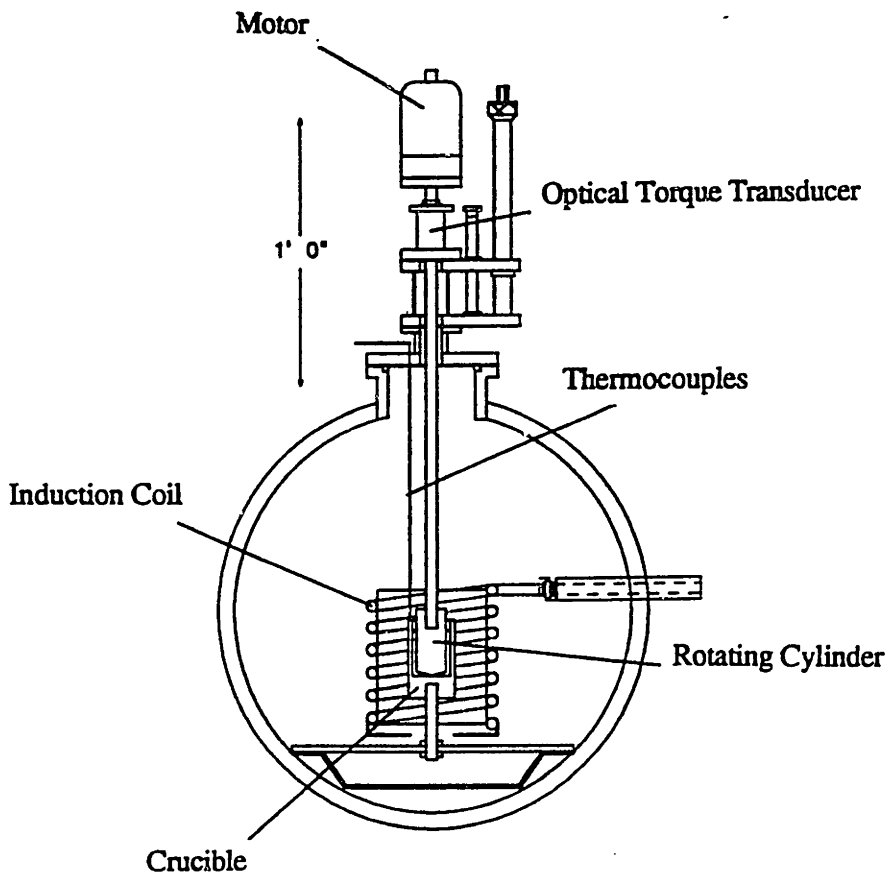

Figure 3.1 Rotating concentric cylinder rheometer mounted inside an induction furnace.

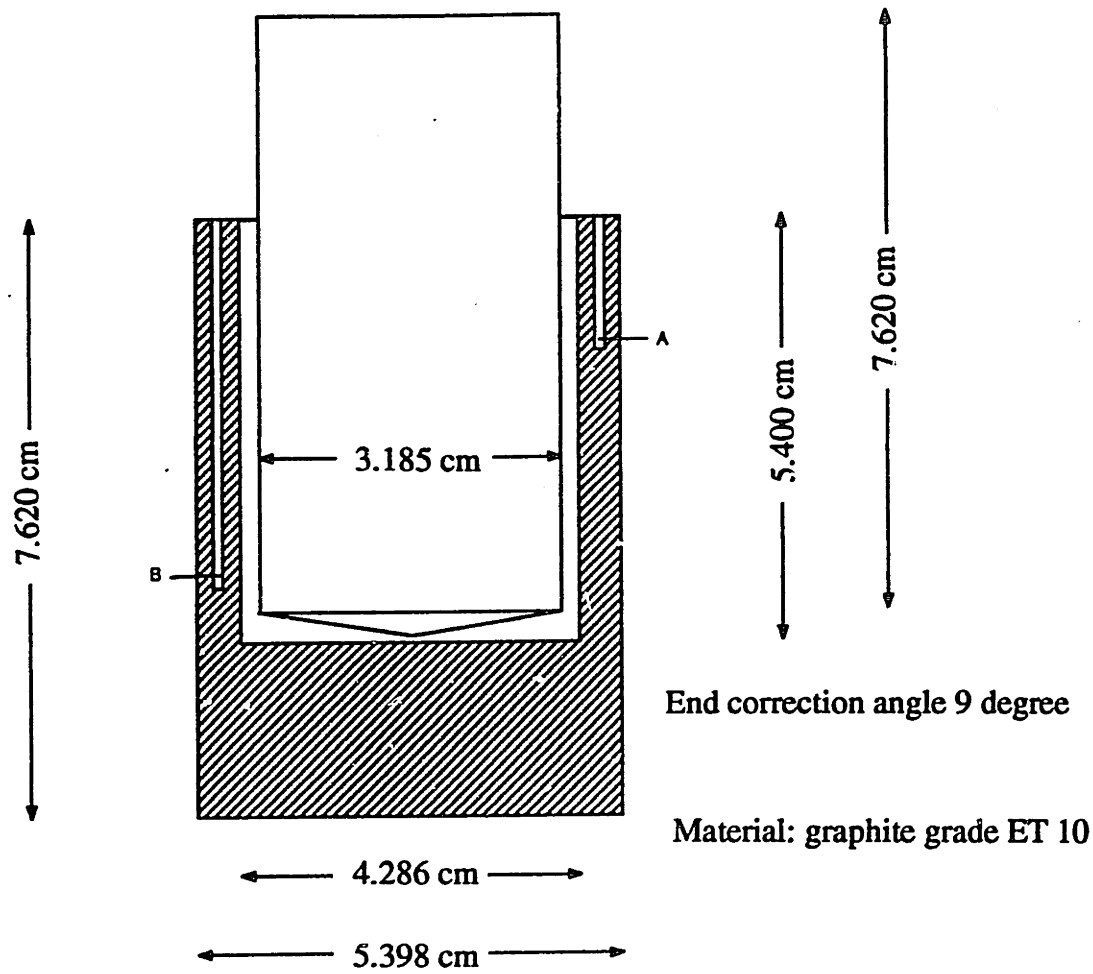

Figure 3.2 Crucible and rotor used in concentric cylinder measurement. Point A and B are where two type-K thermocouples were inserted to monitor the temperature.

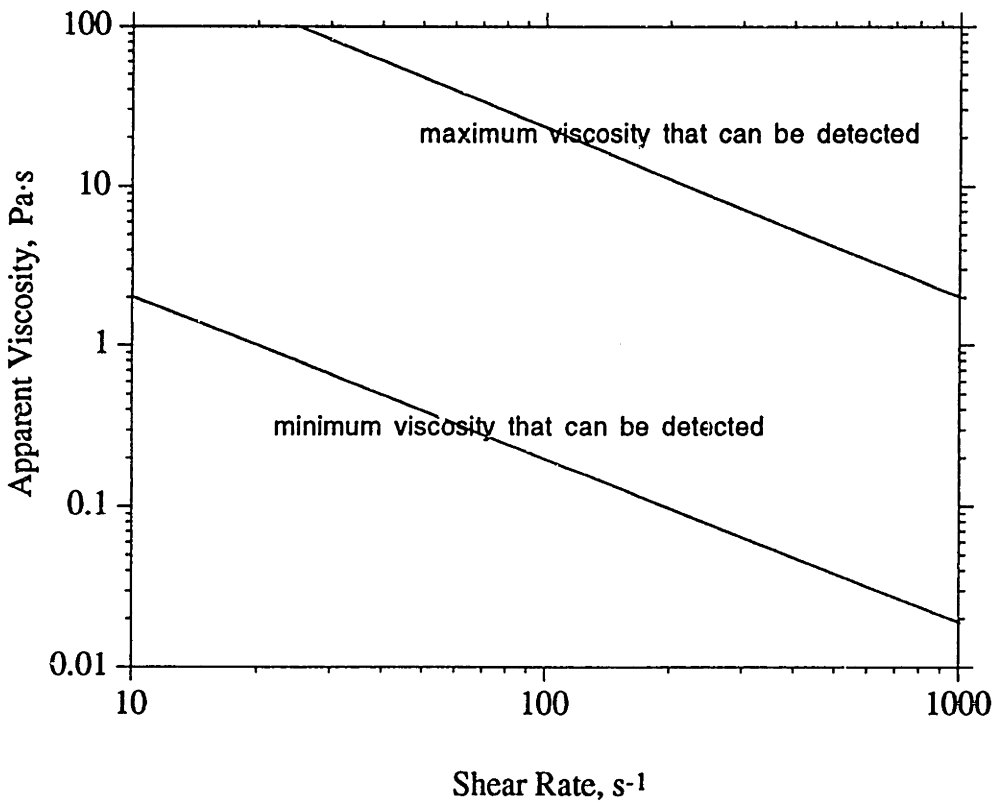

Figure 3.3 Calculated sensitivity of concentric cylinder rheometer at the configuration used in the investigation.

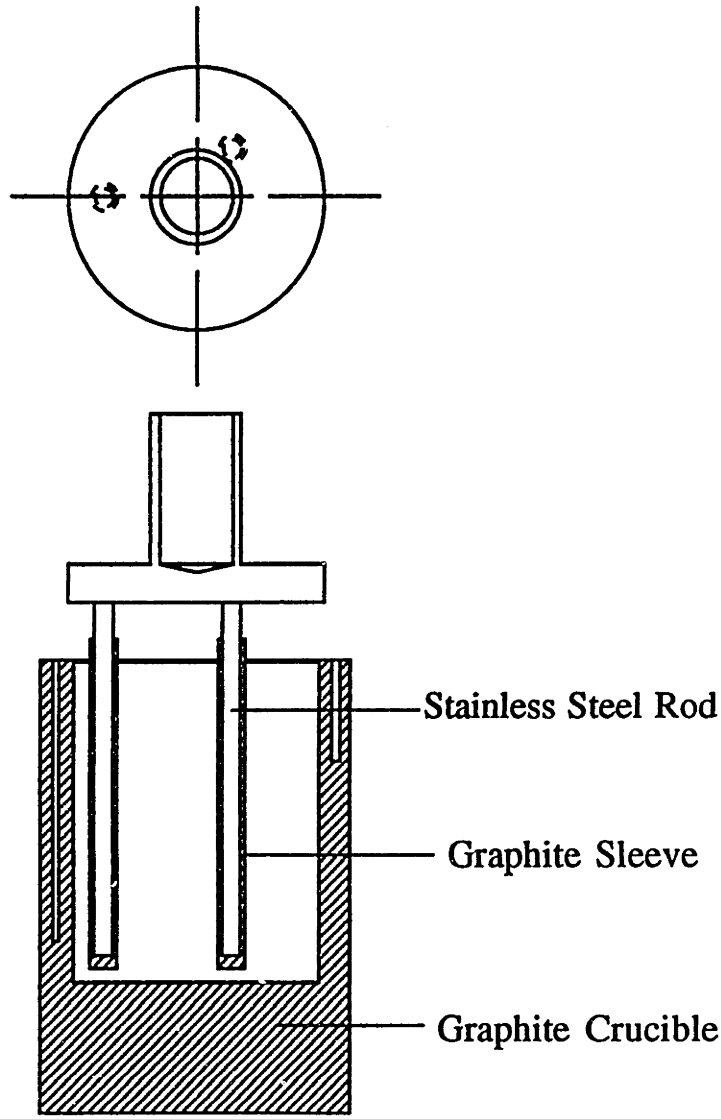

Figure 3.4 Rheocasting facility adapted from the rheometer. The rotating cylinder was replaced with a two-rod stirrer enclosed in graphite sleeves.

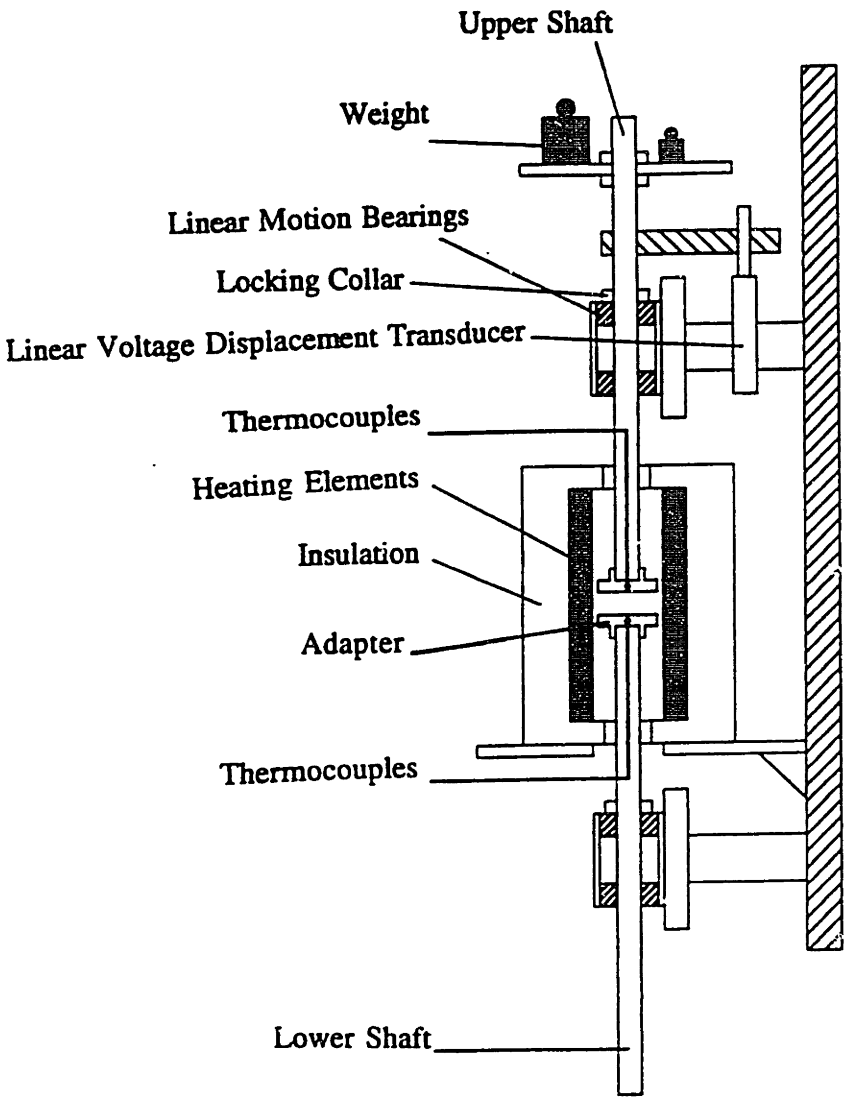

Figure 3.5 Constant-force compression apparatus.

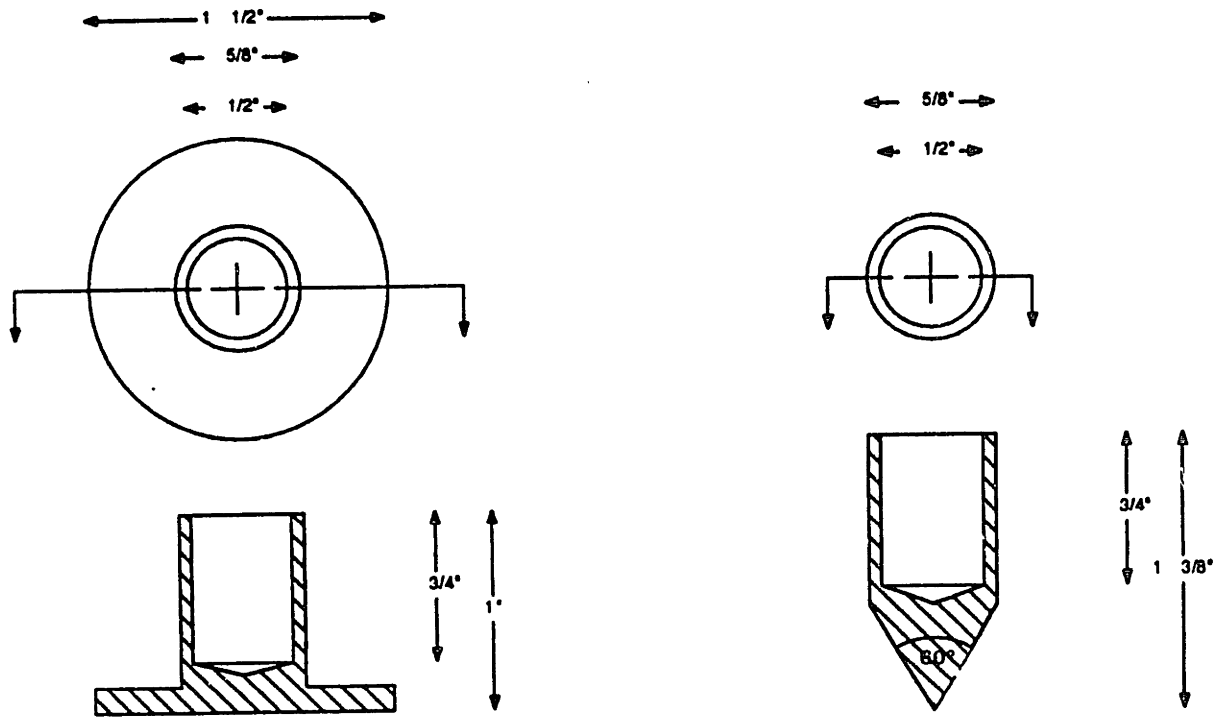

Figure 3.6 (a) An adapter for compression test between two parallel plates. (b) An adapter for cone penetration test.

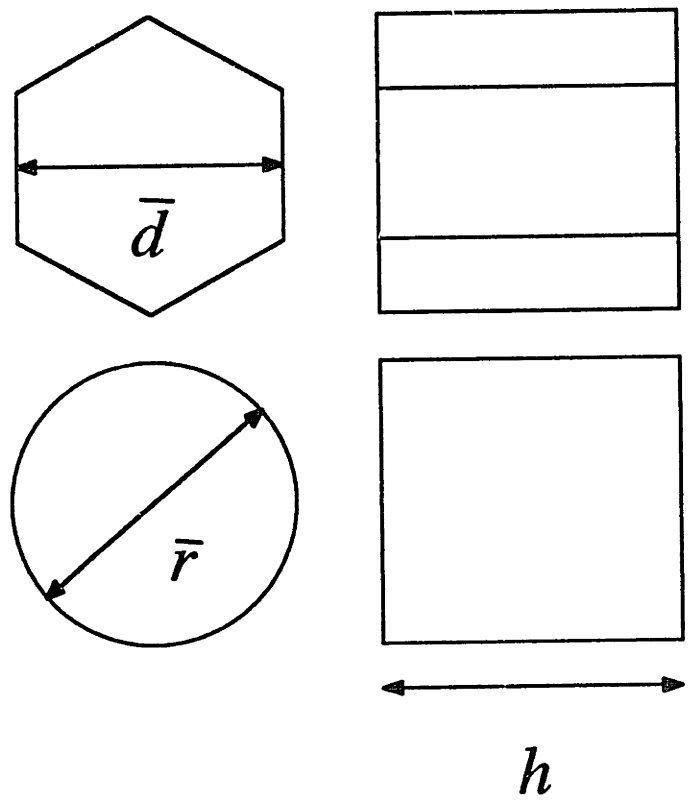

Figure 3.7 A schematic representation of a compression test specimen and an equivalent cylindrical specimen.

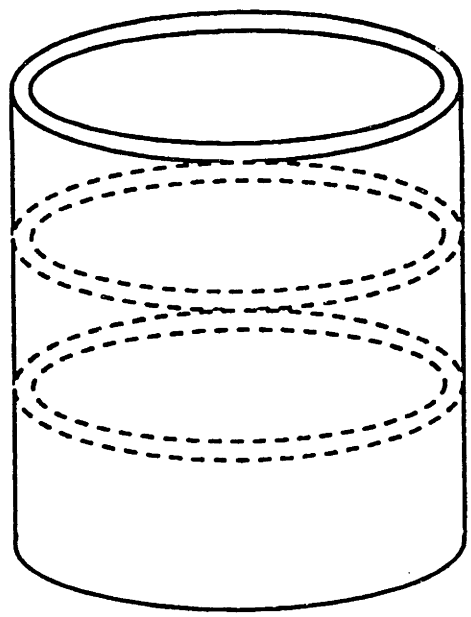

Figure 3.8 Positions where metallographic specimens are taken from concentric cylinder samples.

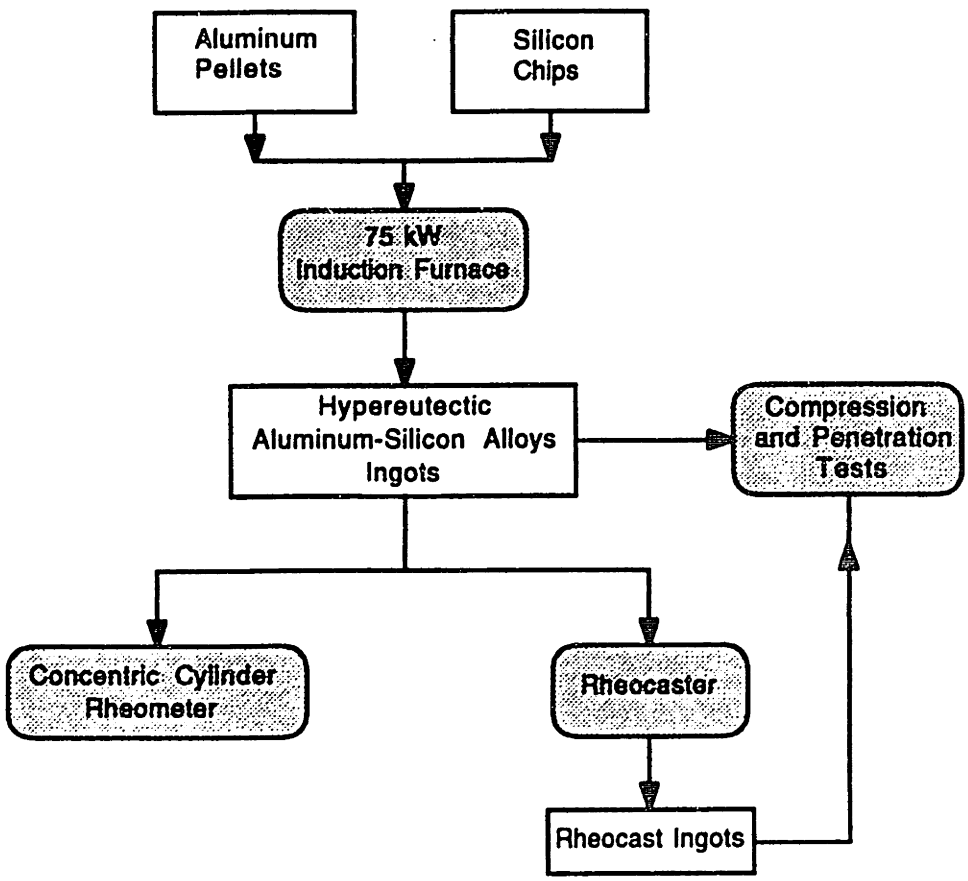

Figure 3.9 A flow chart summarizing the experiments.

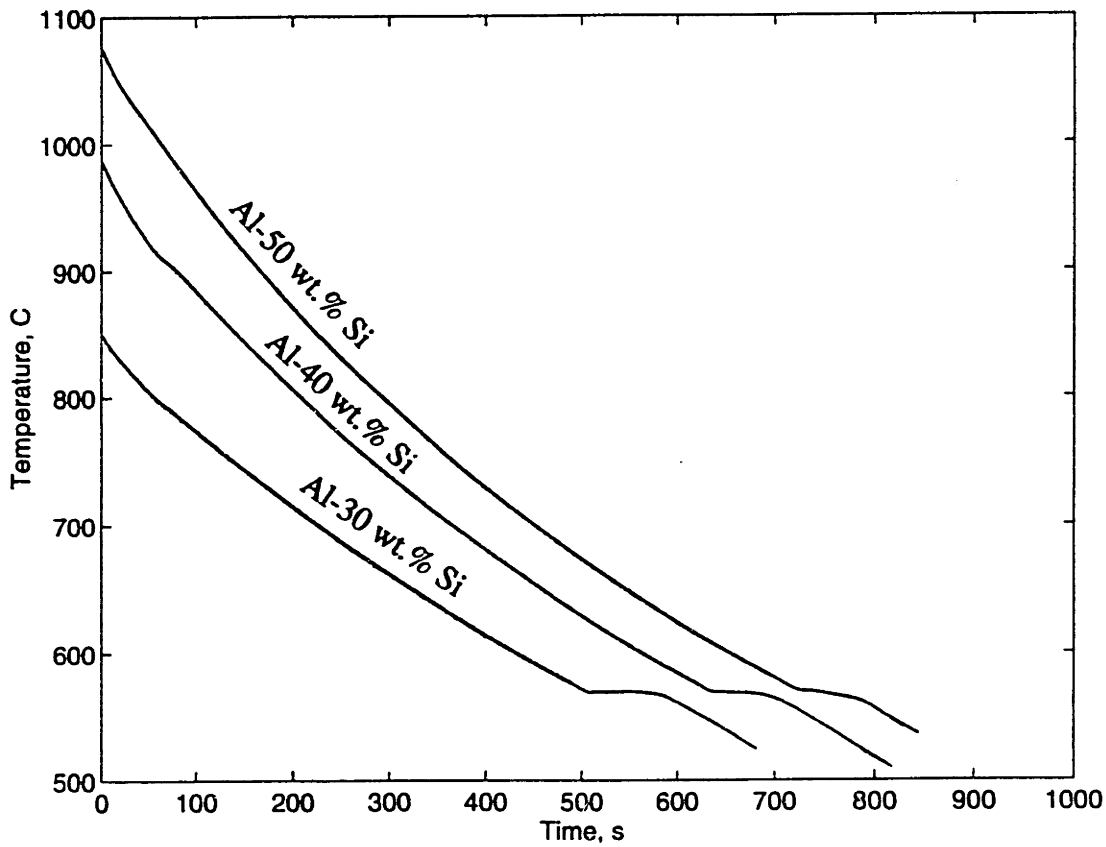

Figure 4.1 Typical temperature versus time in continuous cooling experiments for Al-30, 40, and 50 wt.% Si alloys.

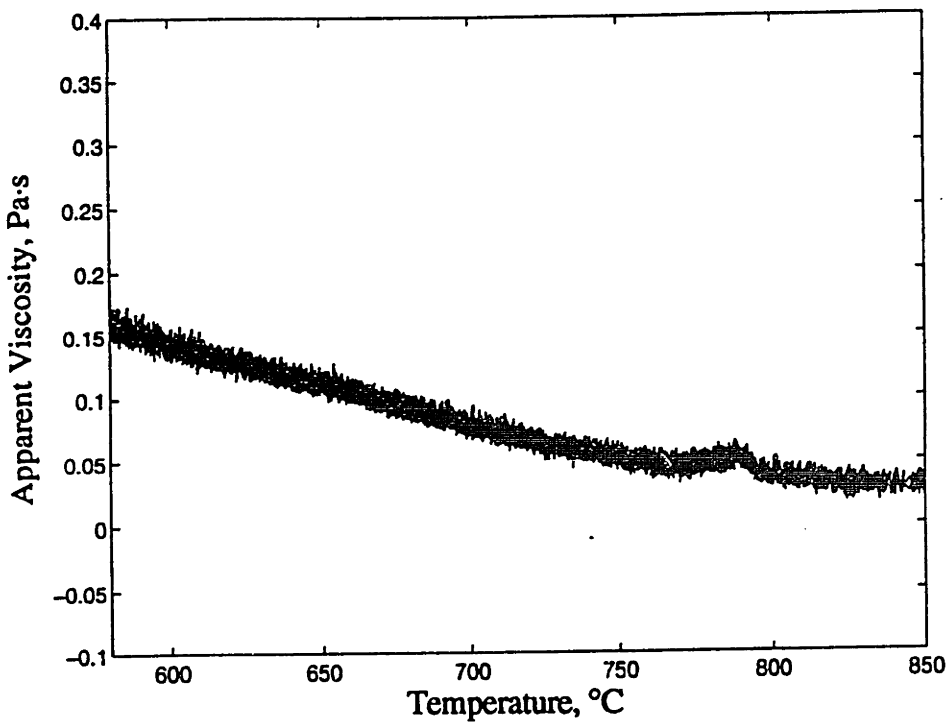

Figure 4.2 Apparent viscosity in a continuous cooling experiment versus temperature. Al-30 wt.% Si was sheared at 320 s^{-1}. The average cooling rate was 35°C/min.

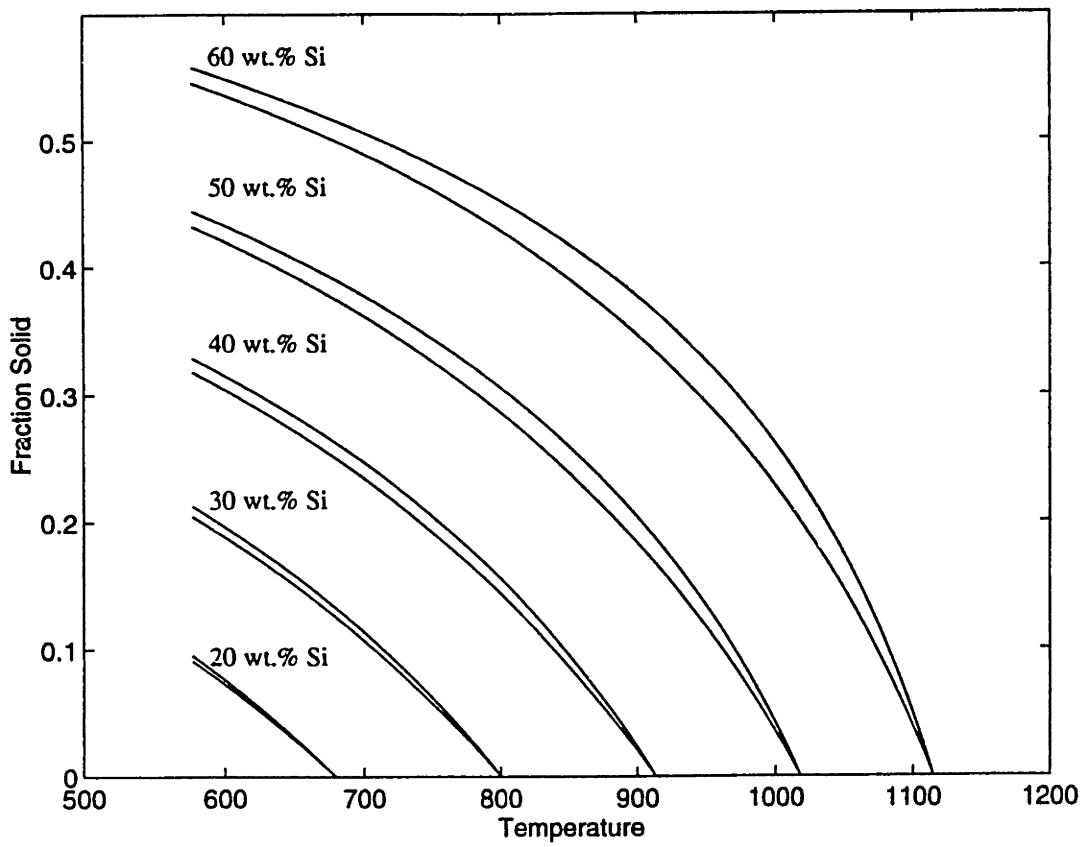

Figure 4.3 Temperature versus silicon volume fraction solid for three hypereutectic Al-Si alloys. The curves are calculated assuming equilibrium solidification condition.

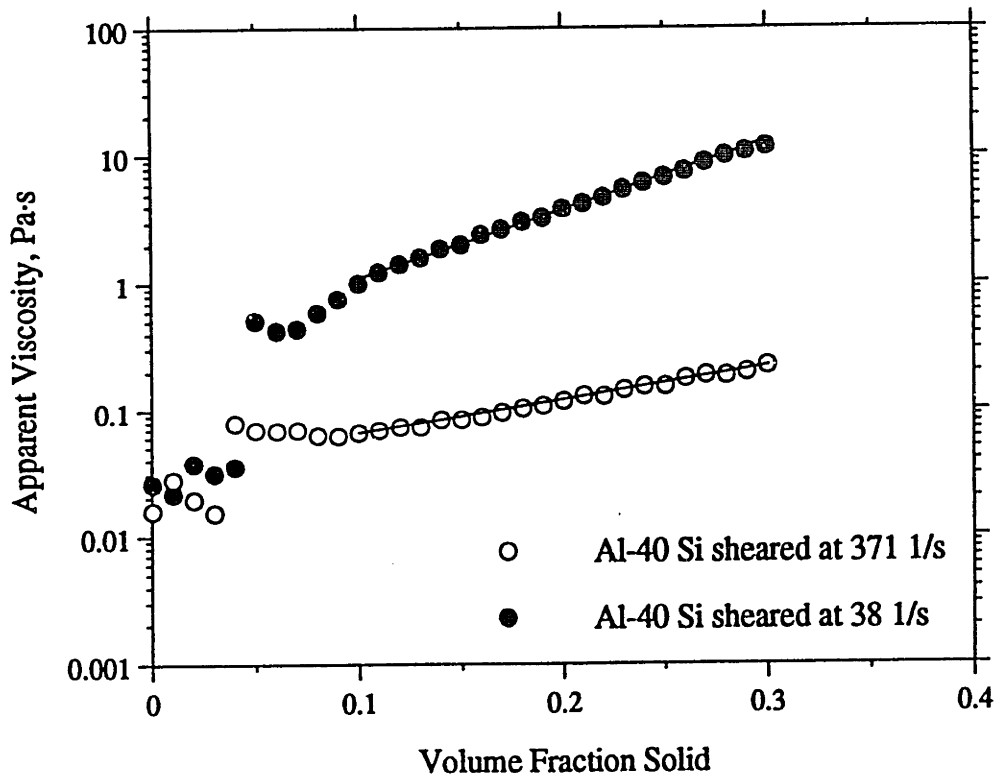

Figure 4.4 Apparent viscosity of semi-solid Al-40 wt.% Si versus volume fraction solid at two different shear rates. The cooling rates were 38°C/min for both samples.

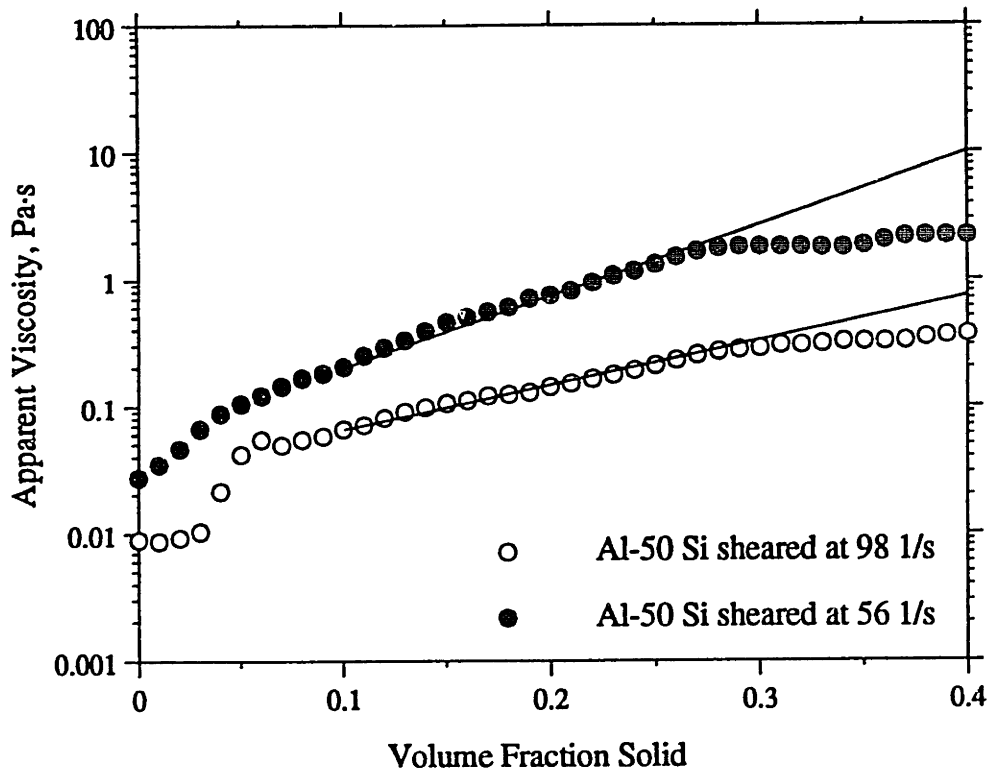

Figure 4.5 Apparent viscosity of semi-solid Al-50 wt.% Si versus volume fraction solid at two different shear rates. The cooling rates were 41°C/min for both samples.

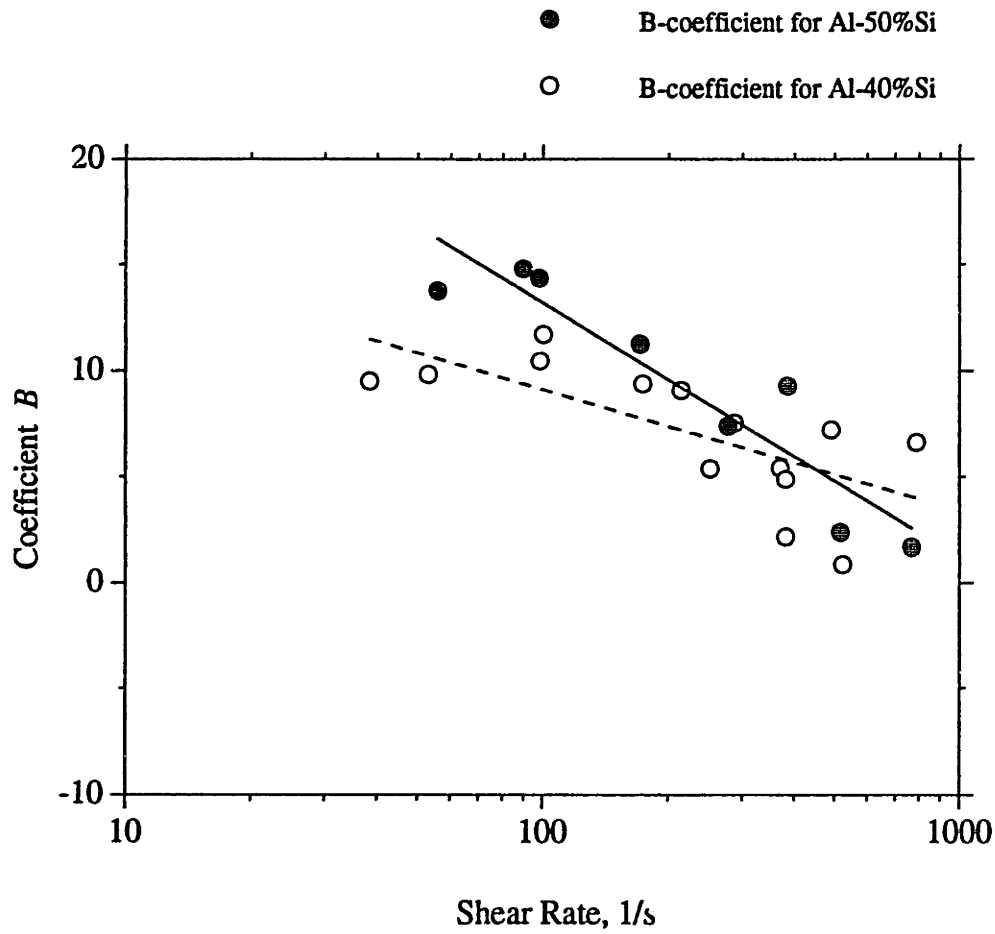

Figure 4.6 Coefficient A from equation (4.2), $\eta = A\exp(Bg_s)$, versus shear rate for Al-40 and 50 wt.% Si slurries.

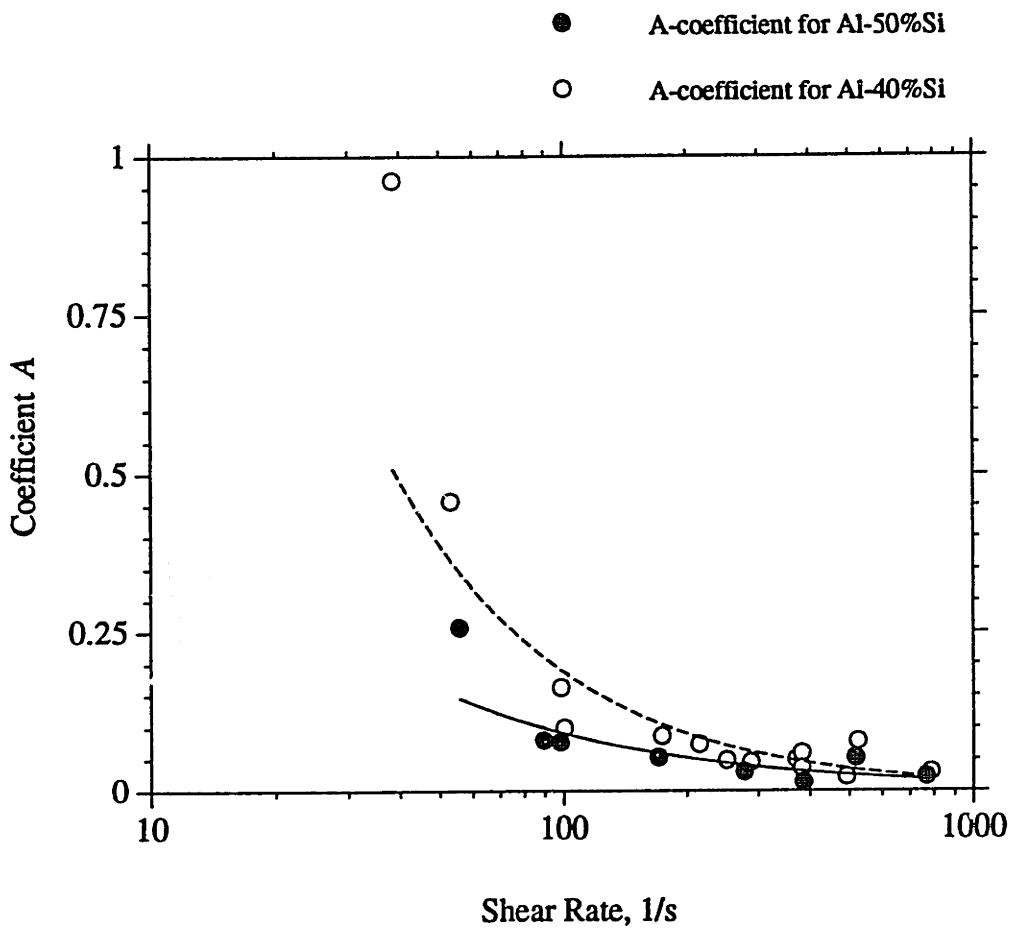

Figure 4.7 Coefficient B from equation (4.2), $\eta = A\exp(Bg_s)$, versus shear rate for Al-40 and 50 wt.% Si slurries.

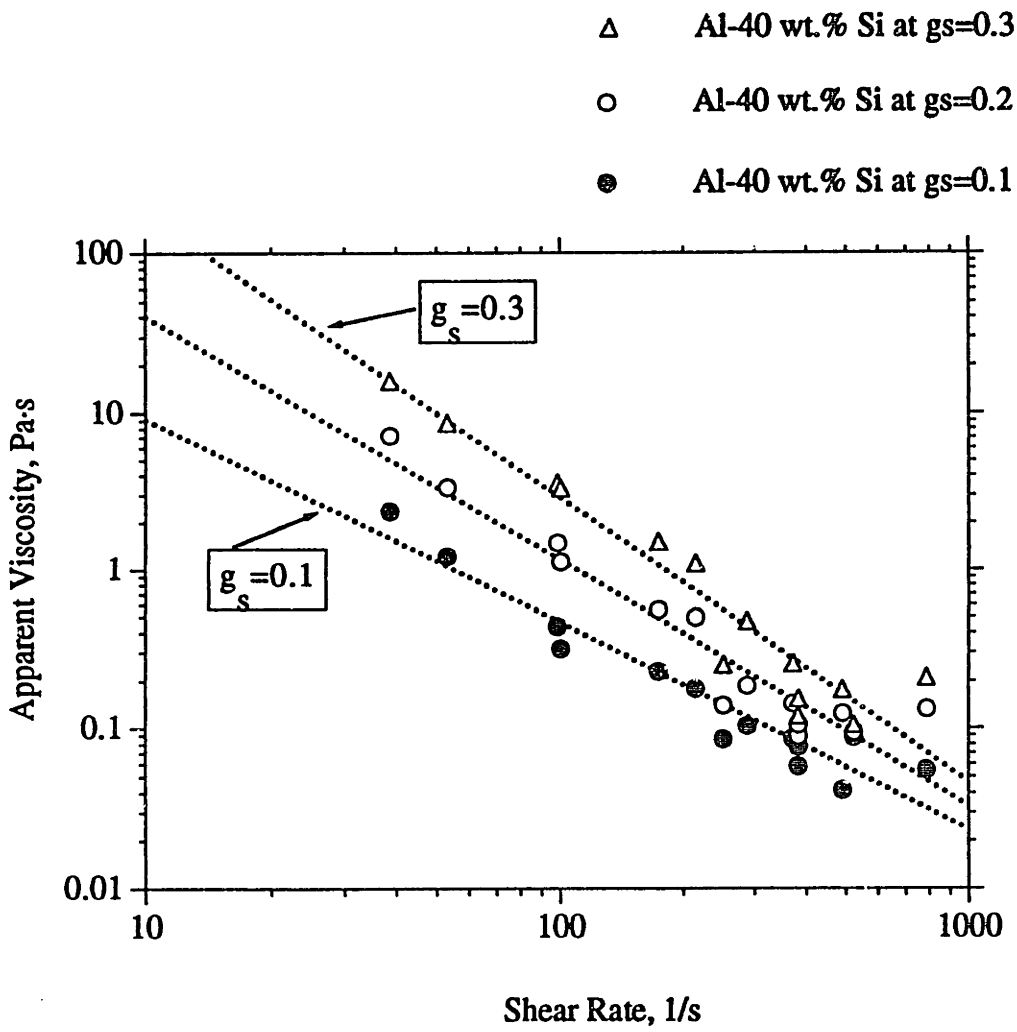

Figure 4.8 Apparent viscosity of Al-40 wt.% Si versus shear rate at volume fraction solid of 0.1, 0.2, and 0.3. Lines from equation (4.7) are included for comparison. The cooling rates were 38°C/min for all samples.

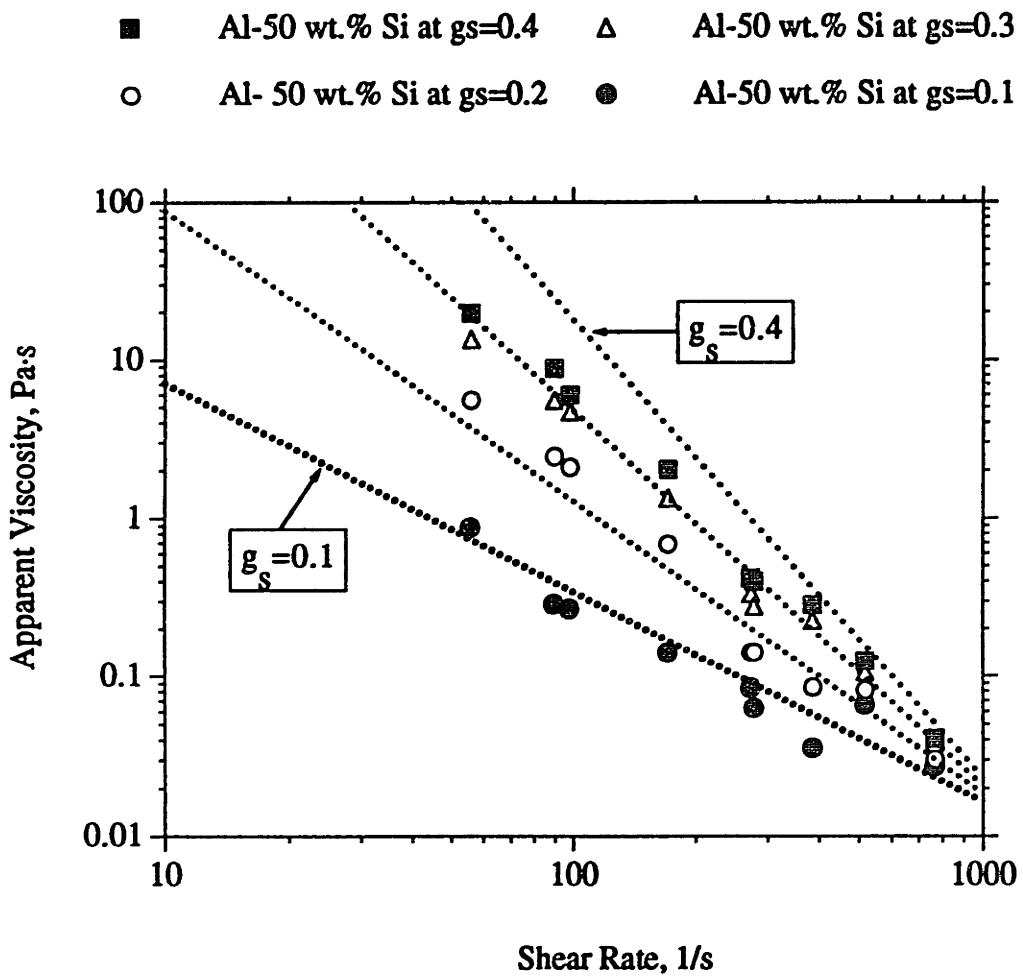

Figure 4.9 Apparent viscosity of Al-50 wt.% Si versus shear rate at volume fraction solid of 0.1, 0.2, 0.3, and 0.4. Lines from equation (4.7) are included for comparison. The cooling rates were 41°C/min for all samples.

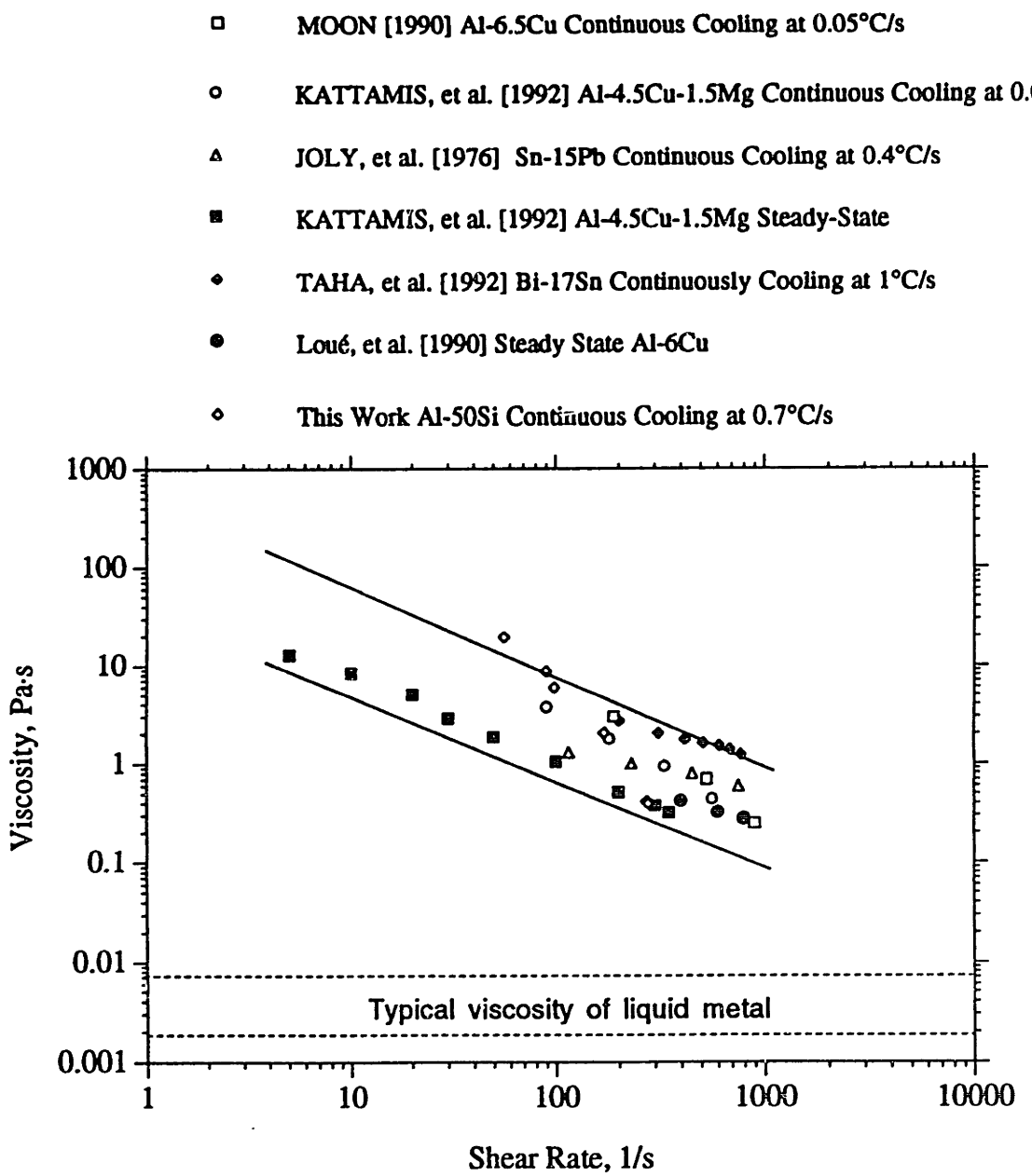

Figure 4.10 Apparent viscosity at $g_s = 0.4$ of various semi-solid alloys versus shear rate.

Figure 4.11 Photomicrograph of Al-40 wt.% Si solidified in concentric cylinder rheometer without shearing. The cooling rate is 40°C/min.

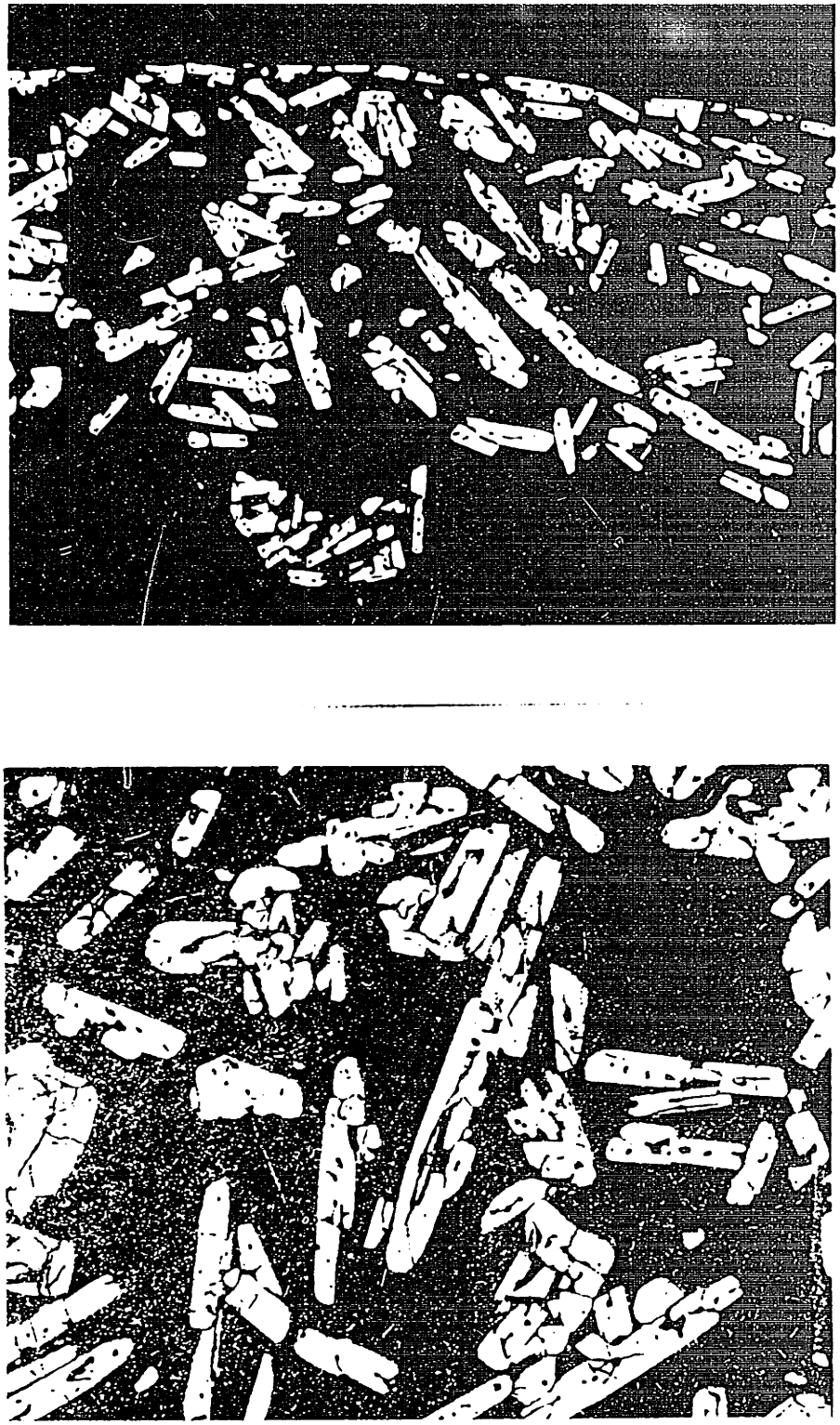

Figure 4.12 Photomicrograph of Al-40 wt.% Si solidified in concentric cylinder rheometer with shear rate of $170s^{-1}$. The cooling rate is 40°C/min.

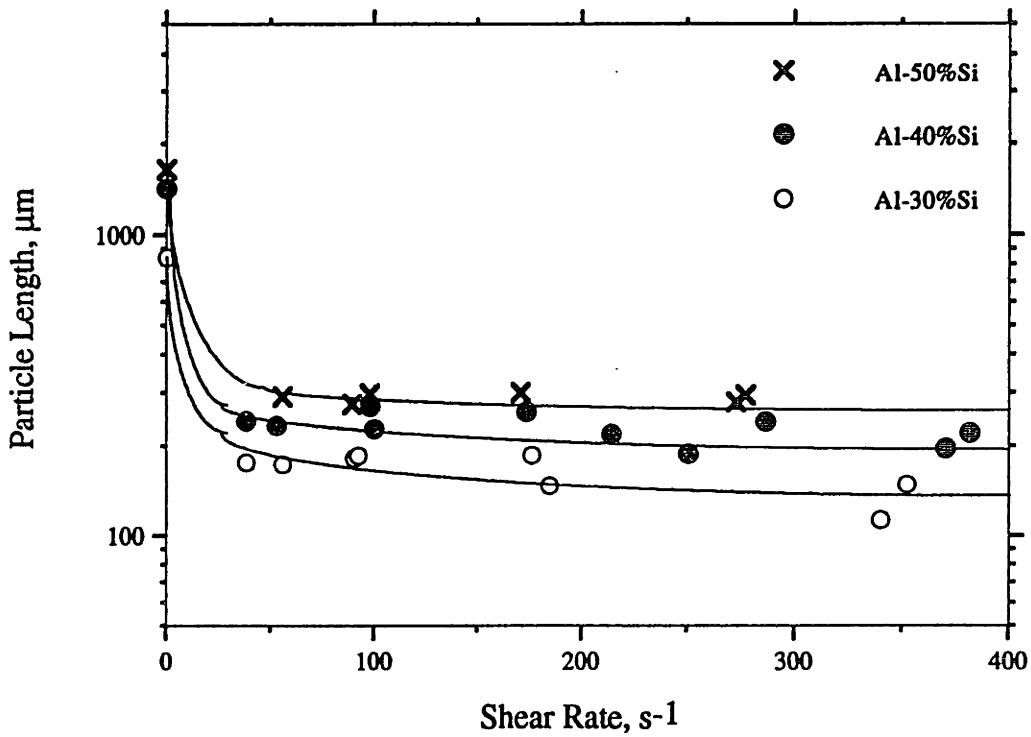

Figure 4.13 Primary silicon particle length versus shear rate for three different silicon content alloys solidified under shearing in concentric cylinder rheometer.

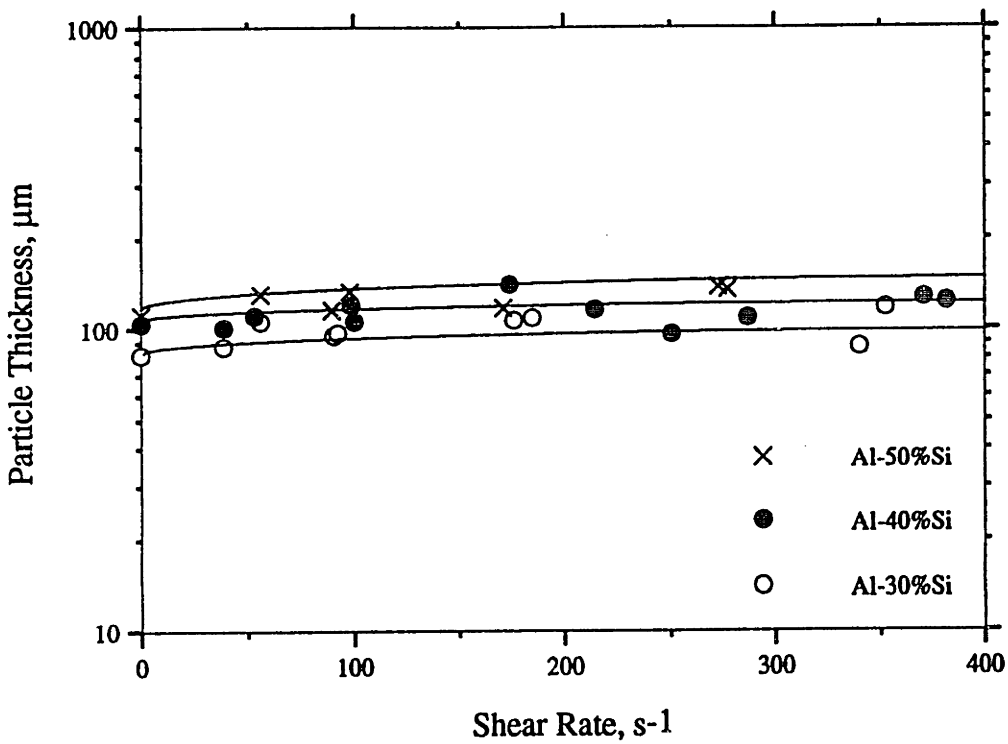

Figure 4.14 Primary silicon particle thickness versus shear rate for three different silicon content alloys solidified under shearing in concentric cylinder rheometer.

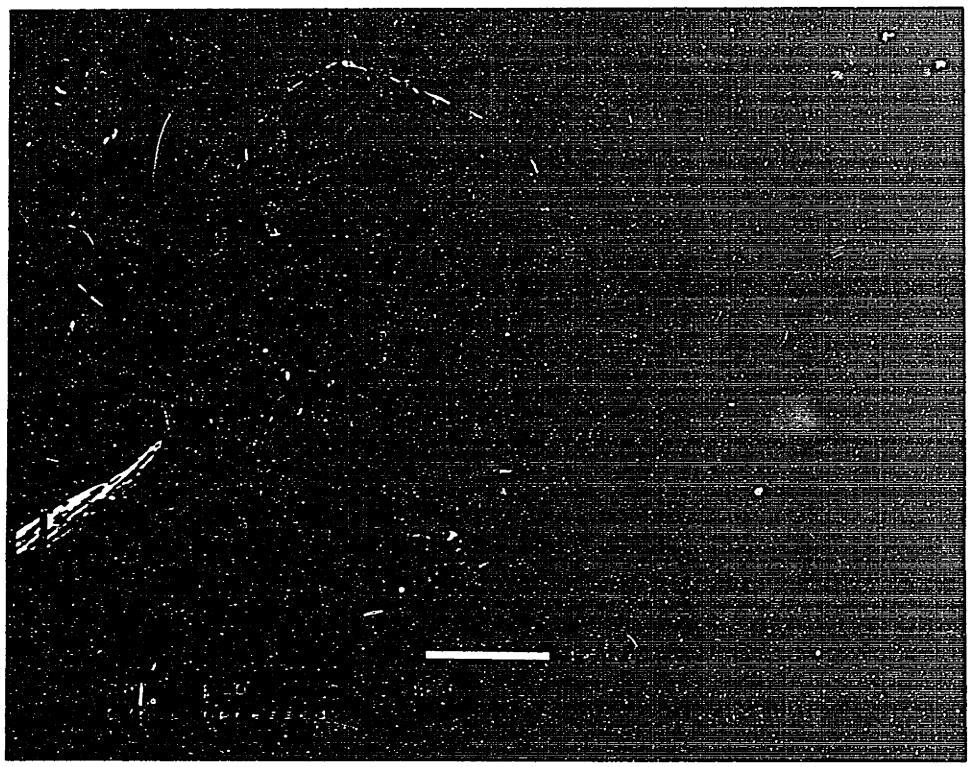

Figure 4.15 Scanning electron micrograph of Al-50 wt.% Si sheared in concentric cylinder rheometer at 380 s^{-1}. Two silicon crystals bonded together and formed an agglomerate.

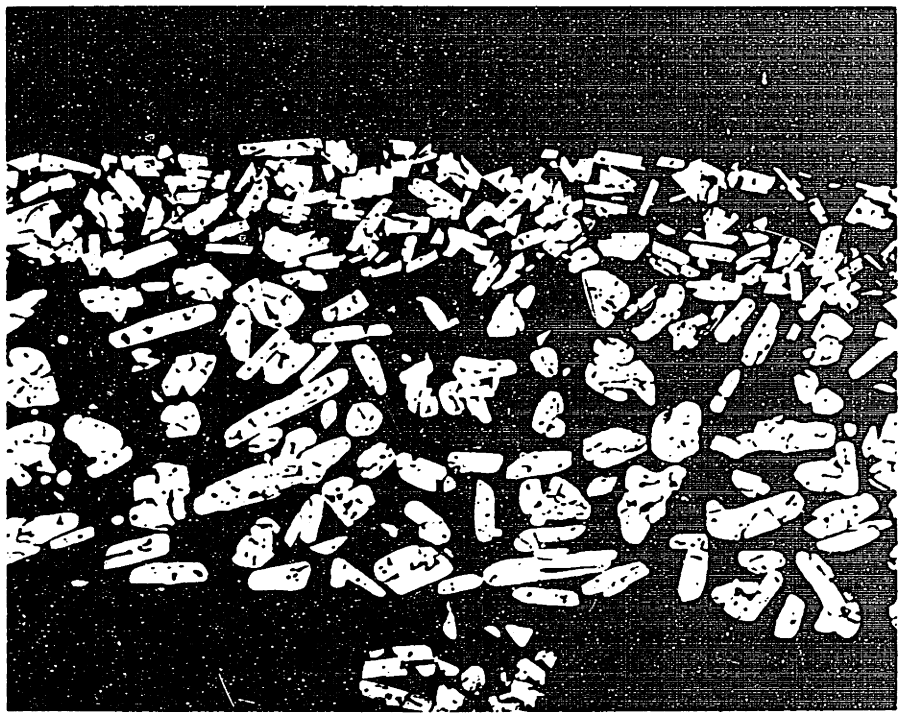

Figure 4.16 Photomicrograph of Al-50 wt.% Si sheared in a concentric cylinder rheometer at $550s^{-1}$. The cooling rate was 40°C/min.

Figure 4.17 Photomicrograph of Al-40 wt.% Si sheared in concentric cylinder rheometer at $170s^{-1}$. The cooling rate was 40°C/min. An agglomerate is indicated by an arrow.

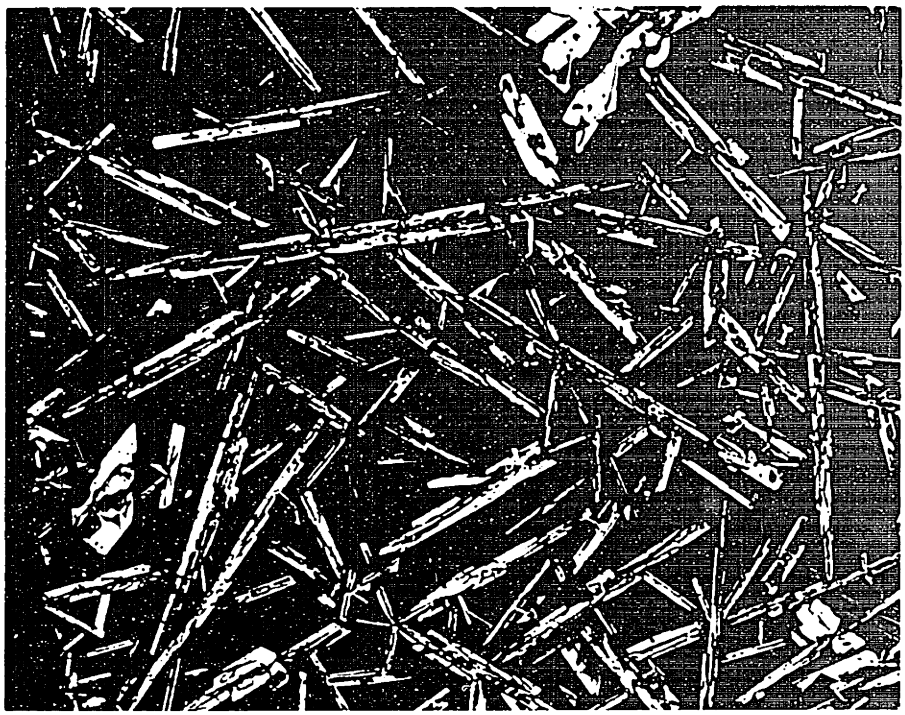

(a)

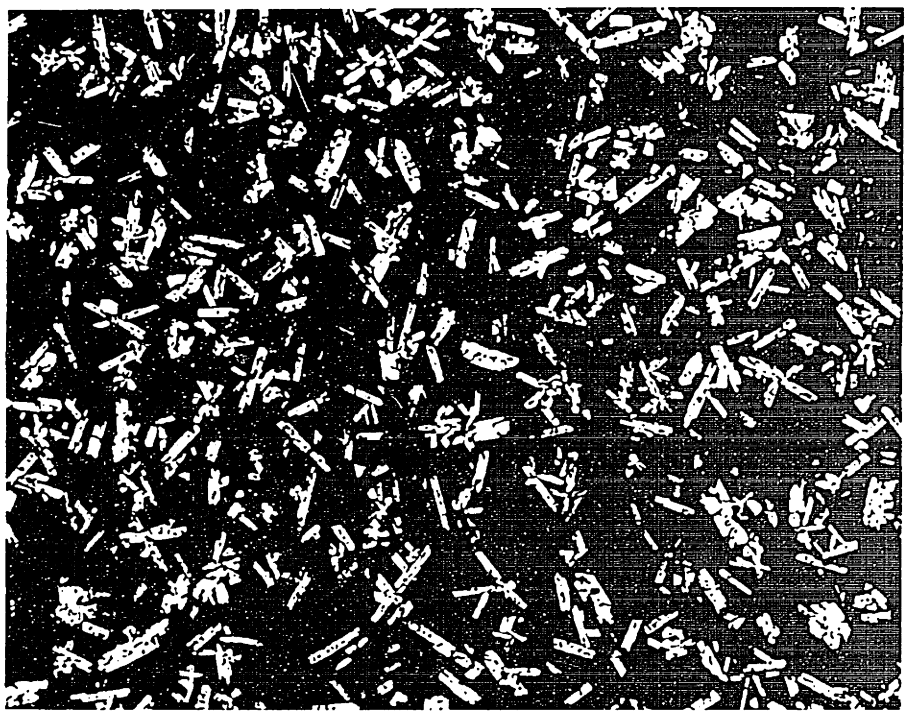

(b)

Figure 5.1 (a) Photomicrograph of Al-30 wt.% Si solidified at 36°C/min without agitation. (b) Photomicrograph of Al-30 wt.% Si rheocast with rotor speed of 550 rpm. Magnification 11.25.

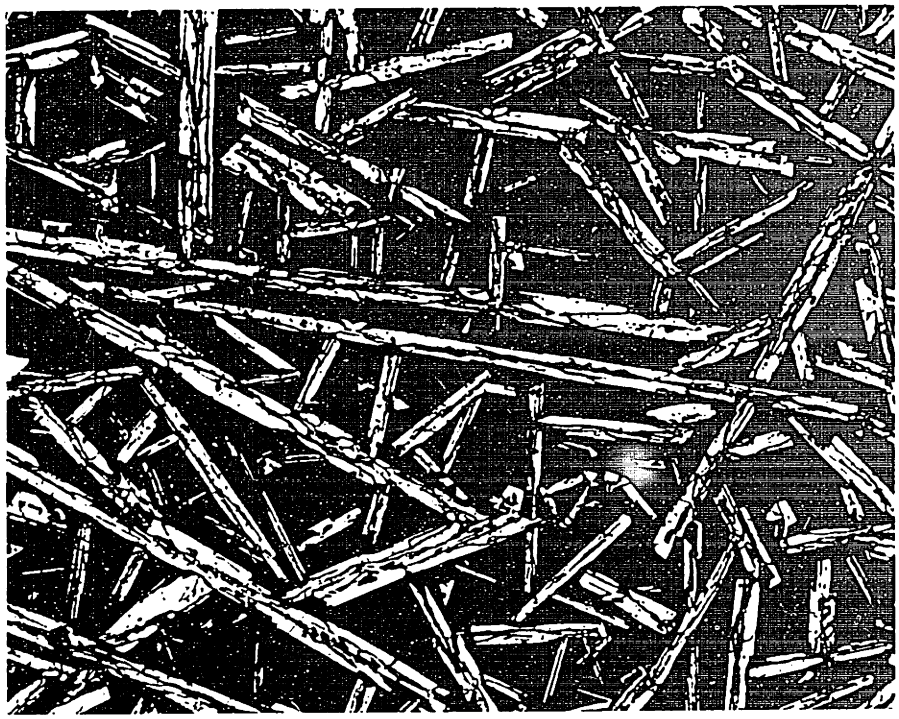

(a)

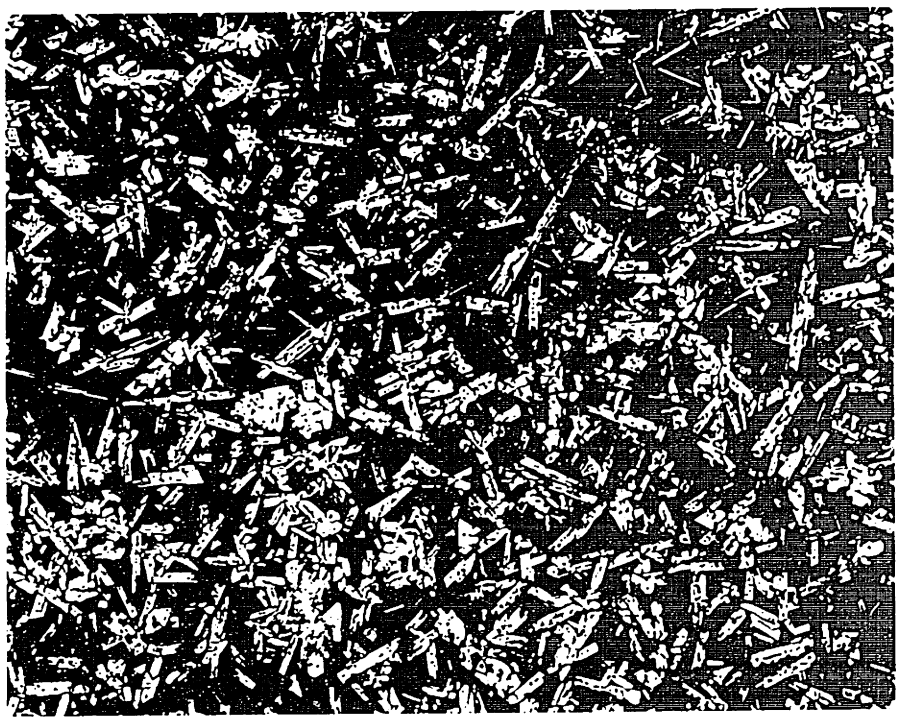

(b)

Figure 5.2 (a) Photomicrograph of Al-40 wt.% Si solidified at 40°C/min without agitation. (b) Photomicrograph of Al-40 wt.% Si rheocast with rotor speed of 550 rpm. Magnification 11.25.

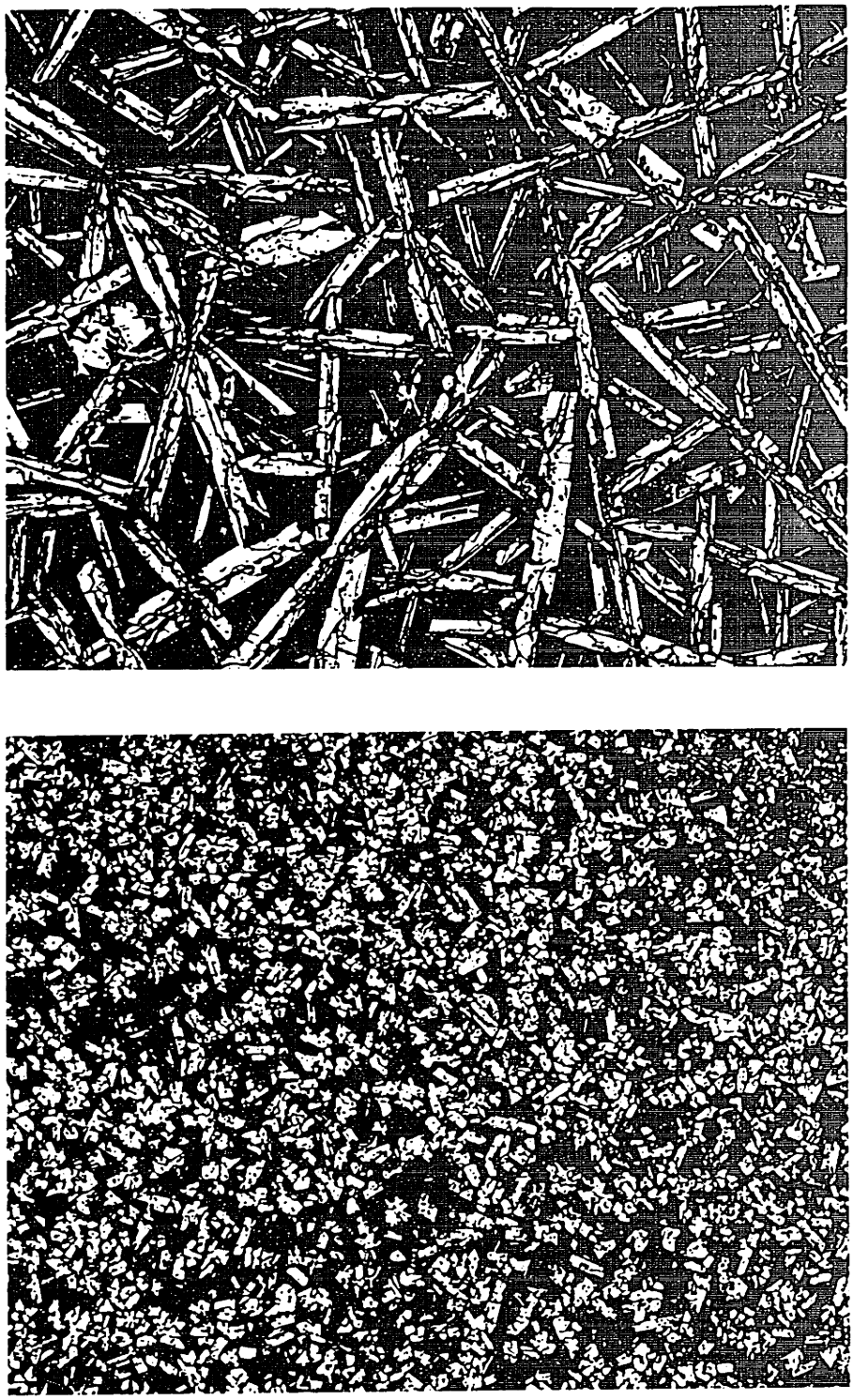

(a)

(b)

Figure 5.3 (a) Photomicrograph of Al-50 wt.% Si solidified at 48°C/min without agitation. (b) Photomicrograph of Al-50 wt.% Si rheocast with rotor speed of 550 rpm. Magnification 11.25.

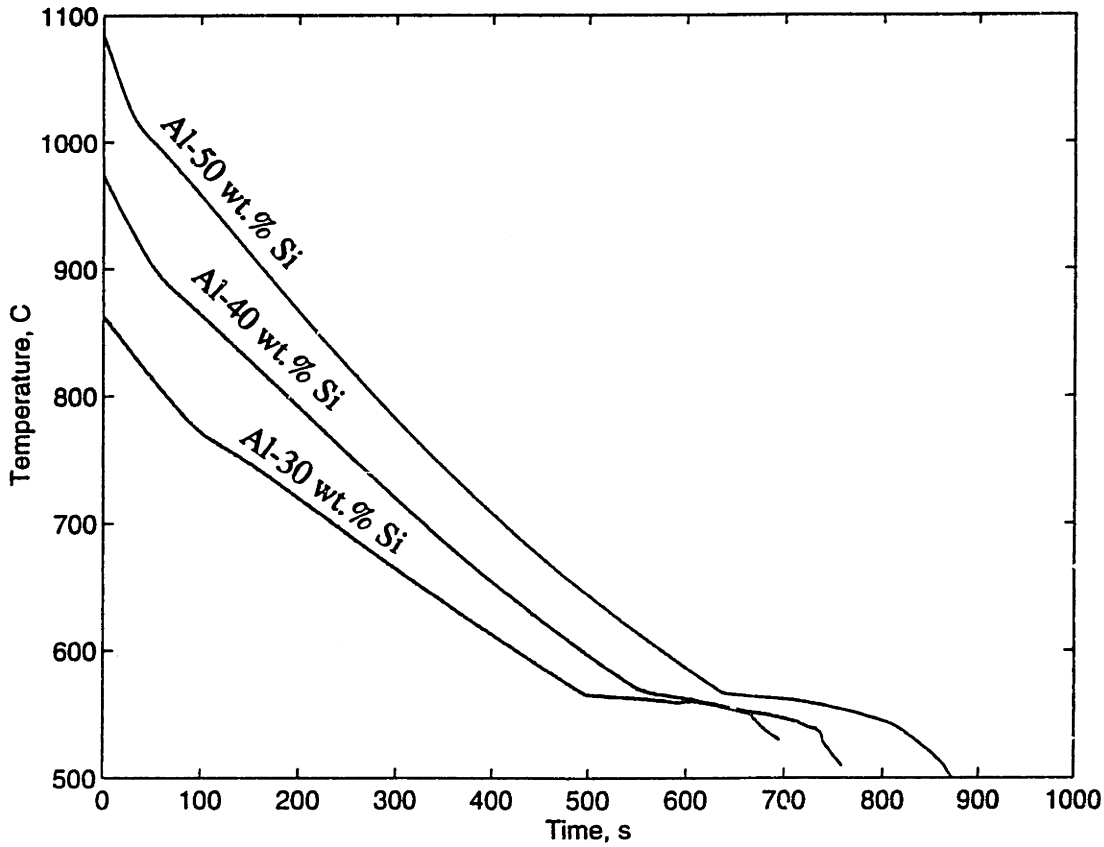

Figure 5.4 Typical temperature versus time curves during rheocasting of Al-30, 40, and 50 wt.% Si alloys.

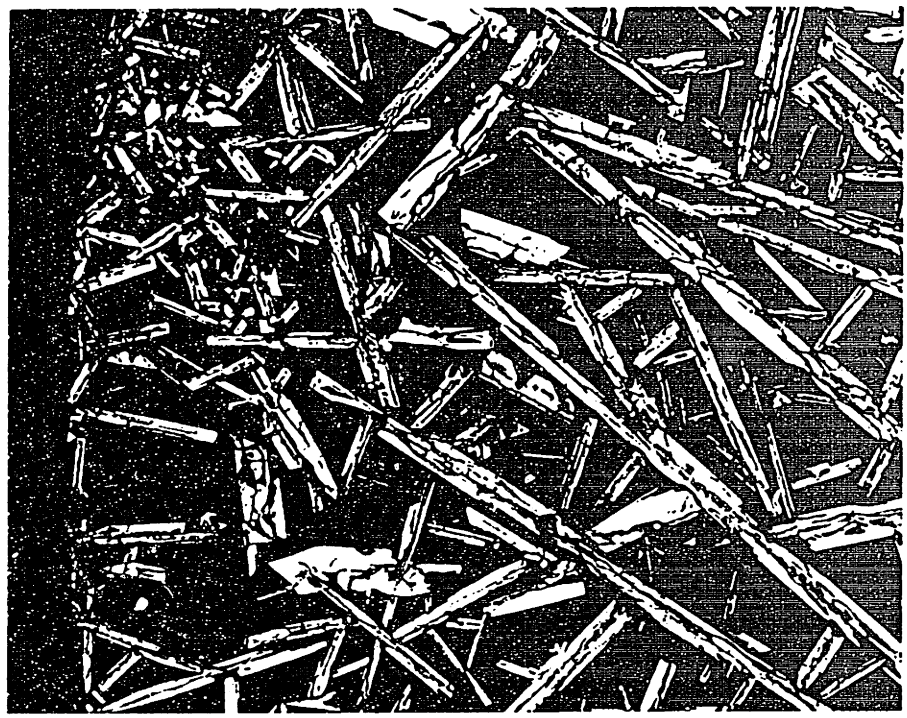

Figure 5.5 Photomicrograph of Al-40 wt.% Si solidified at 40°C/min without agitation indicating preferred nucleation on the mold wall. Magnification 11.25.

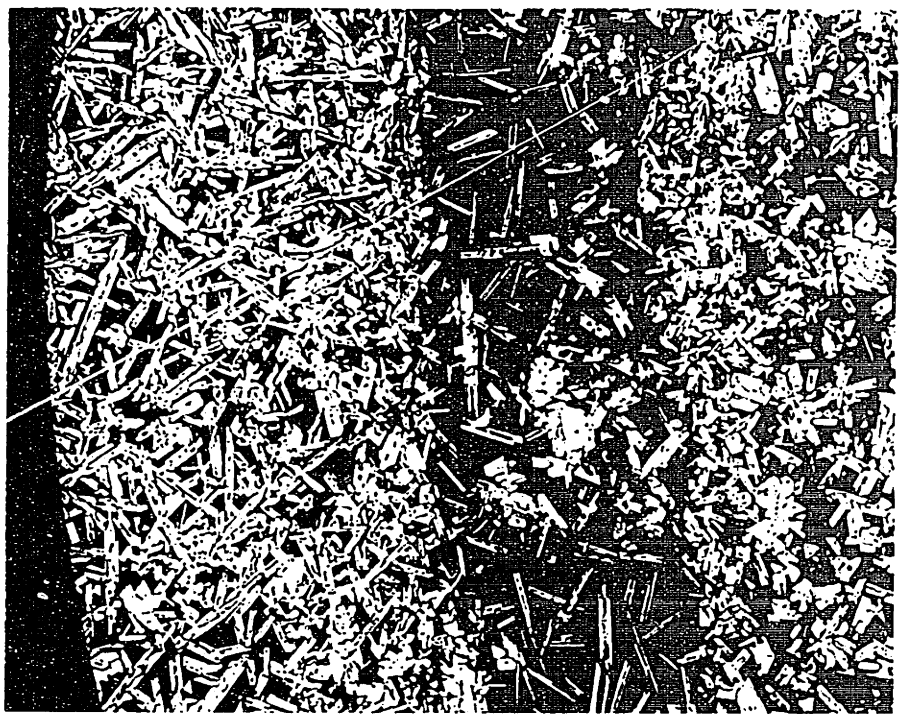

Figure 5.6 Photomicrograph of rheocast Al-50 wt.% Si indicating the segregation of silicon. The agitation was stopped at extremely low temperature ($g_s = 0.35$). Magnification 11.25.

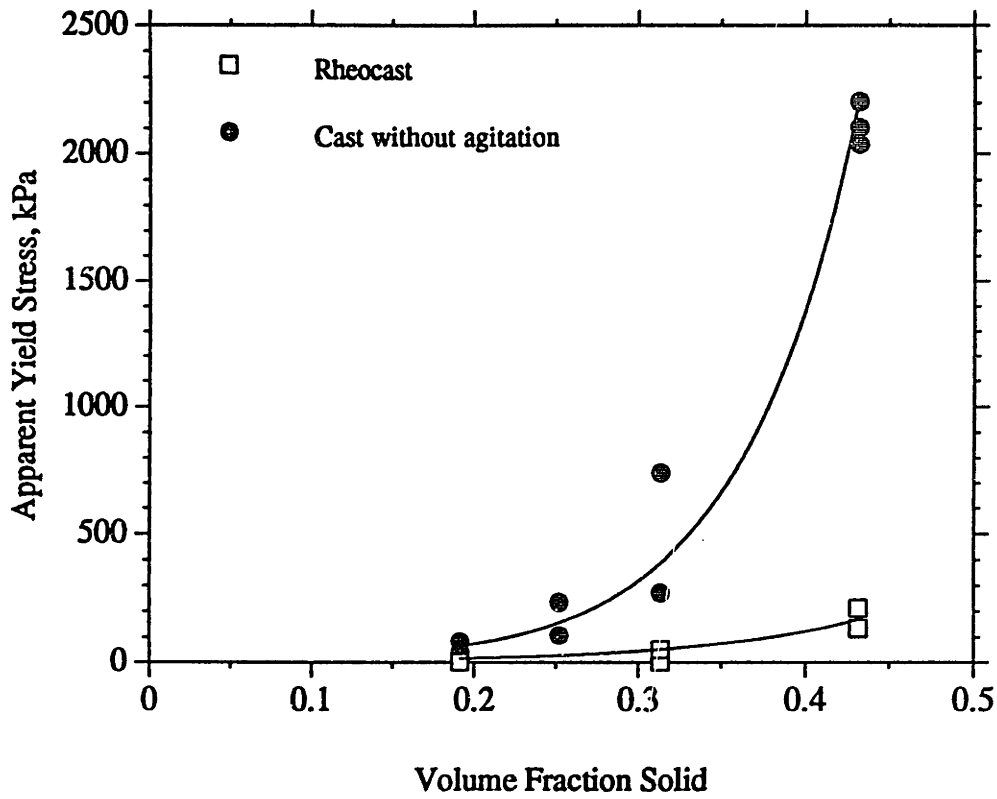

Figure 5.7 Apparent yield stress versus volume fraction solid for alloys in this work with silicon up to 50 wt.% solidified with and without agitation.

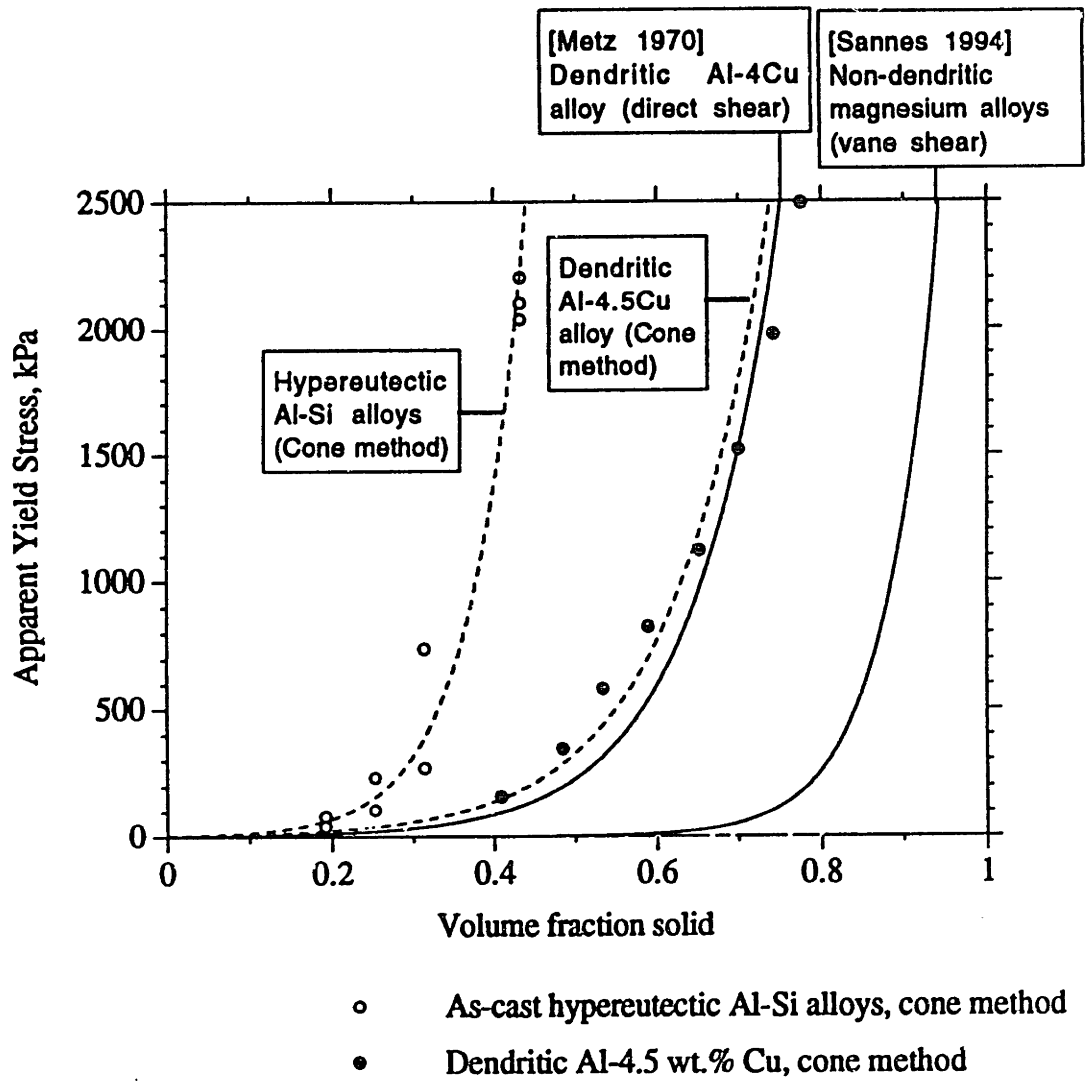

Figure 5.8 Apparent yield stress versus volume fraction solid of Al-4 wt.% Cu. Results from two different measurement techniques: cone penetration in this work and direct shear by METZ, et al. [1969] are compared.

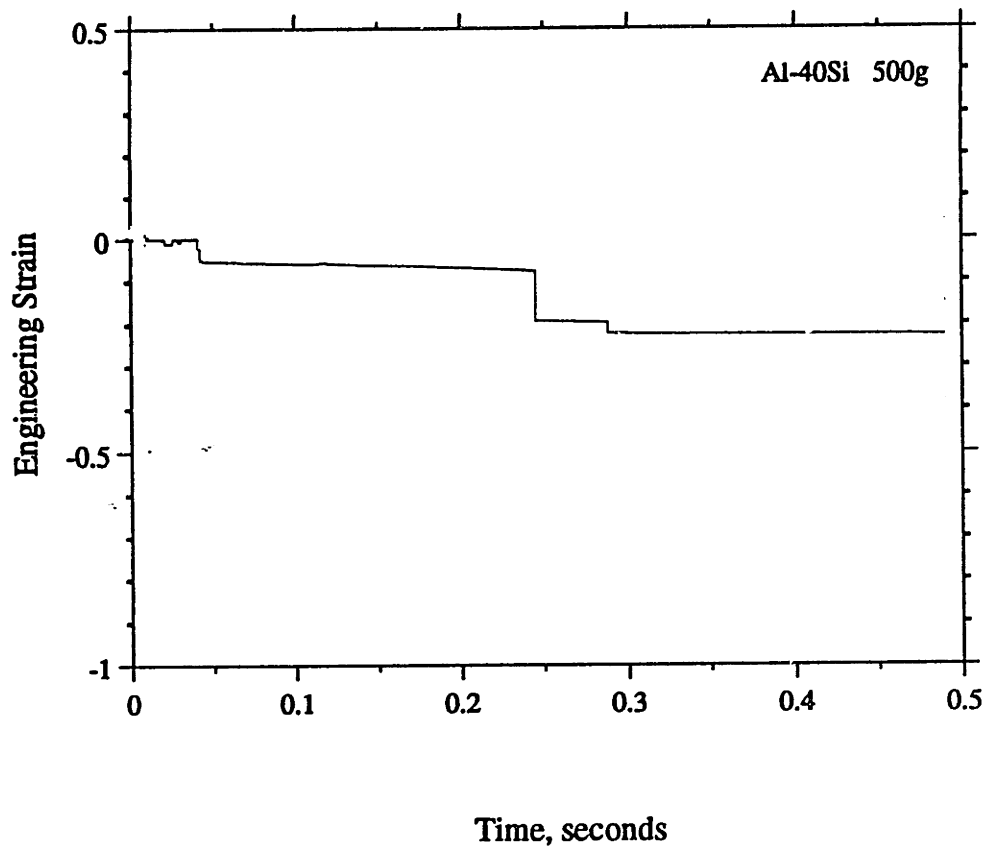

Figure 5.9 A plot of engineering strain versus time for a rheocast Al-40 wt.% Si specimen. The compression load is 500 g at $g_s = 0.31$.

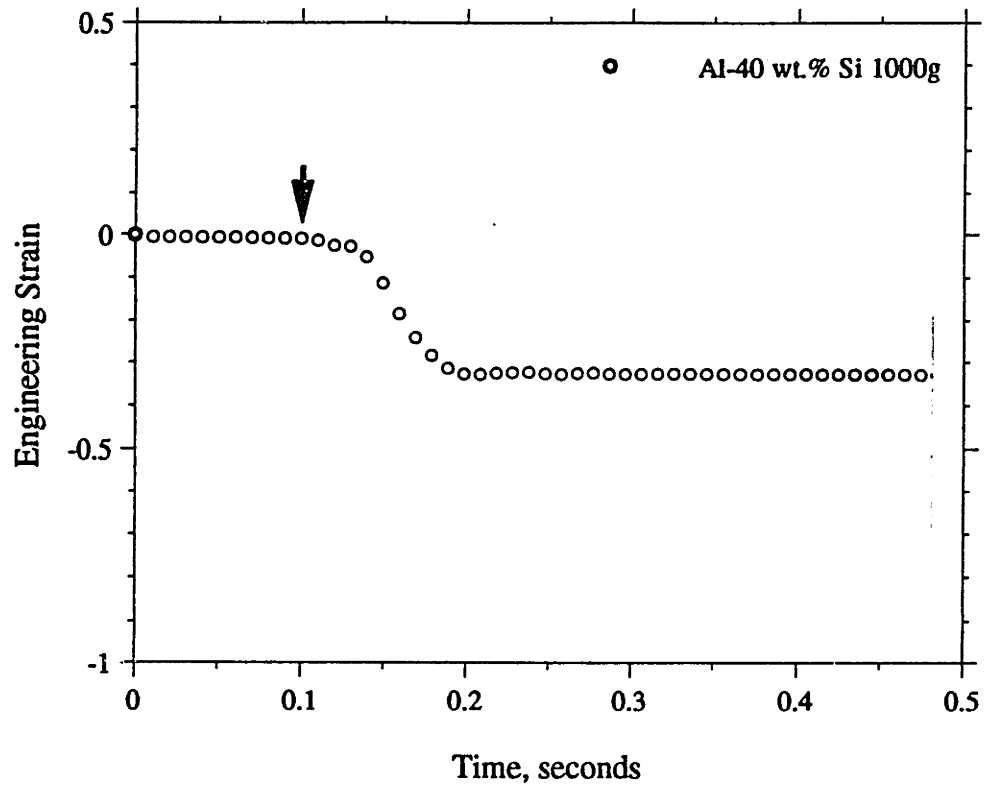

Figure 5.10 Engineering strain versus time for a rheocast Al-40 wt.% Si specimen. The compression load was 1000 g at $g_s = 0.31$.

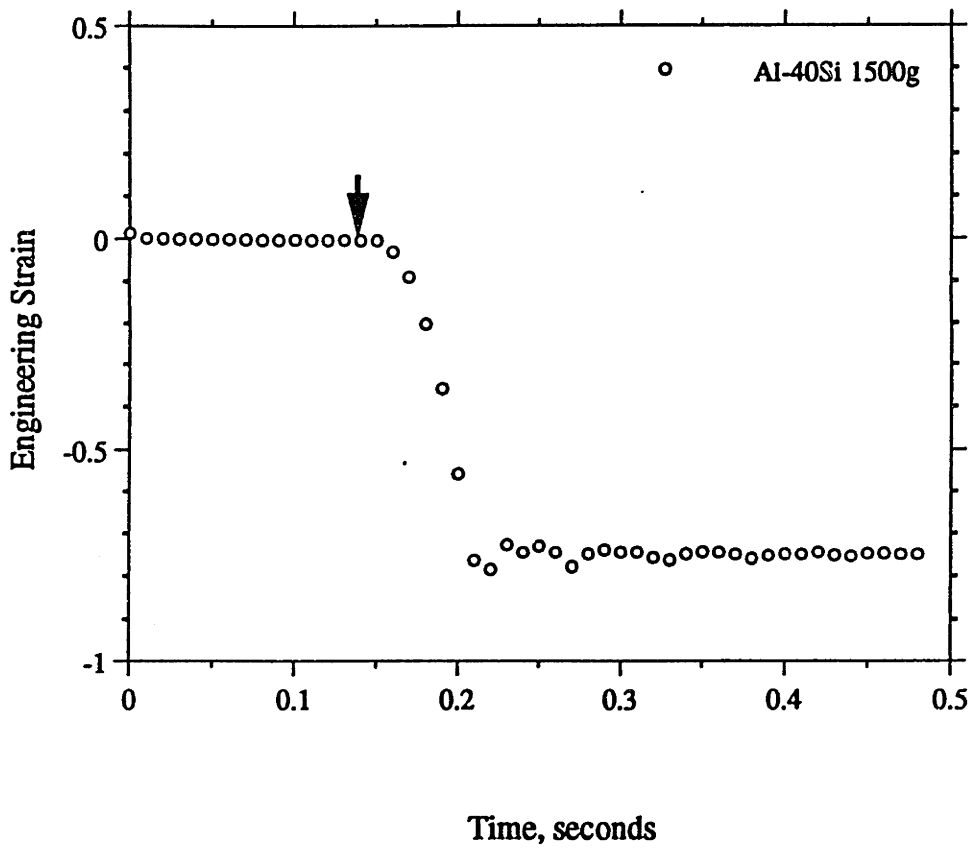

Figure 5.11 Engineering strain versus time for a rheocast Al-40 wt.% Si specimen. The compression load was 1500 g at $g_s = 0.31$.

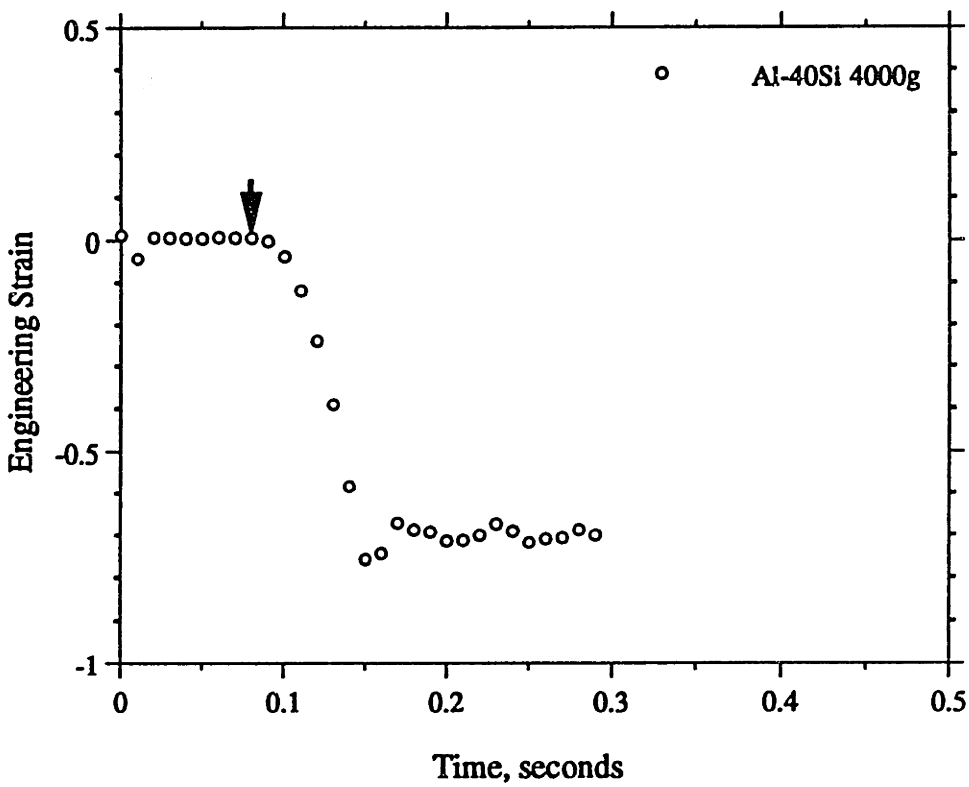

Figure 5.12 Engineering strain versus time for a rheocast Al-40 wt.% Si specimen. The compression load was 4000 g at $g_s = 0.31$.

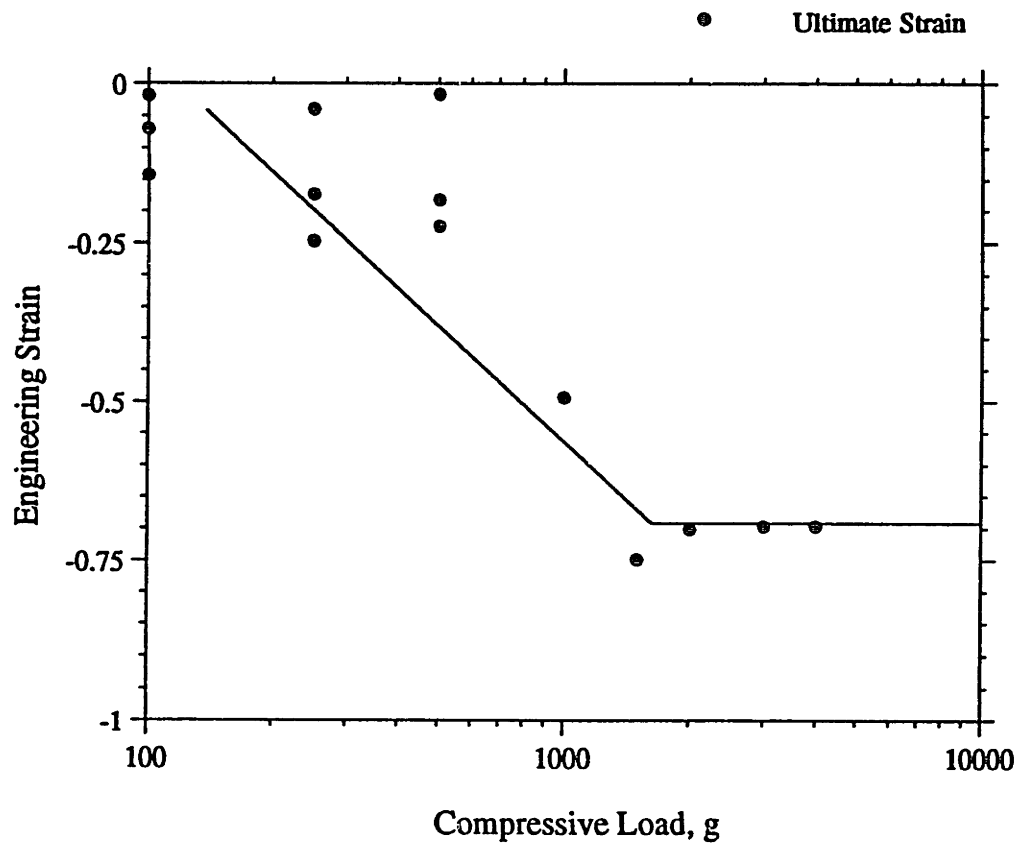

Figure 5.13 Ultimate engineering strain versus compressive load for rheocast Al-40 wt.% Si specimens under various compression loads from 100 to 4000 g at $g_s = 0.31$.

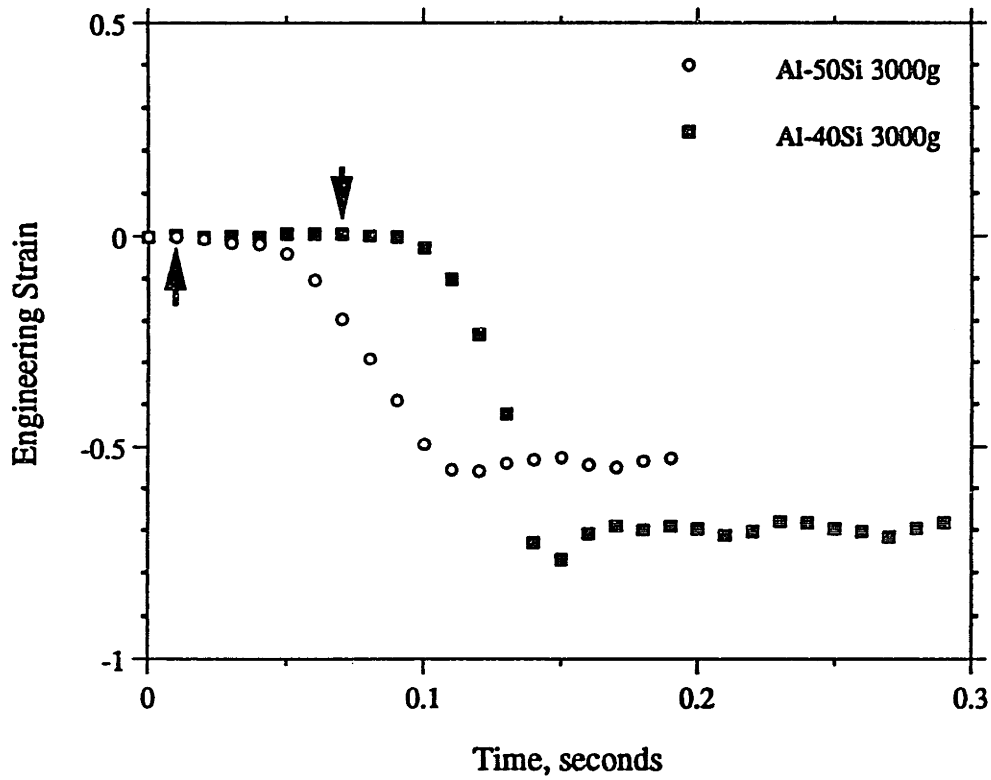

Figure 5.14 Engineering strain versus time for a rheocast Al-40, and 50 wt.% Si specimen. The compression load was 3000 g. Volume fractions solid are 0.31 and 0.42 for Al-40 wt.% and 50 wt.% Si, respectively.

CENTER

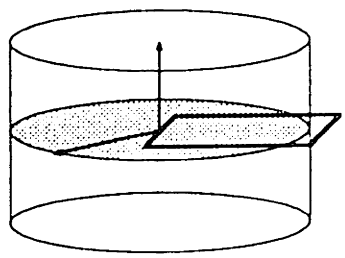

EDGE

Figure 5.15 Photomicrograph of radial and horizontal cross sections of compressed Al-40 wt.% Si specimen under 3000 g load. Magnification 11.25.

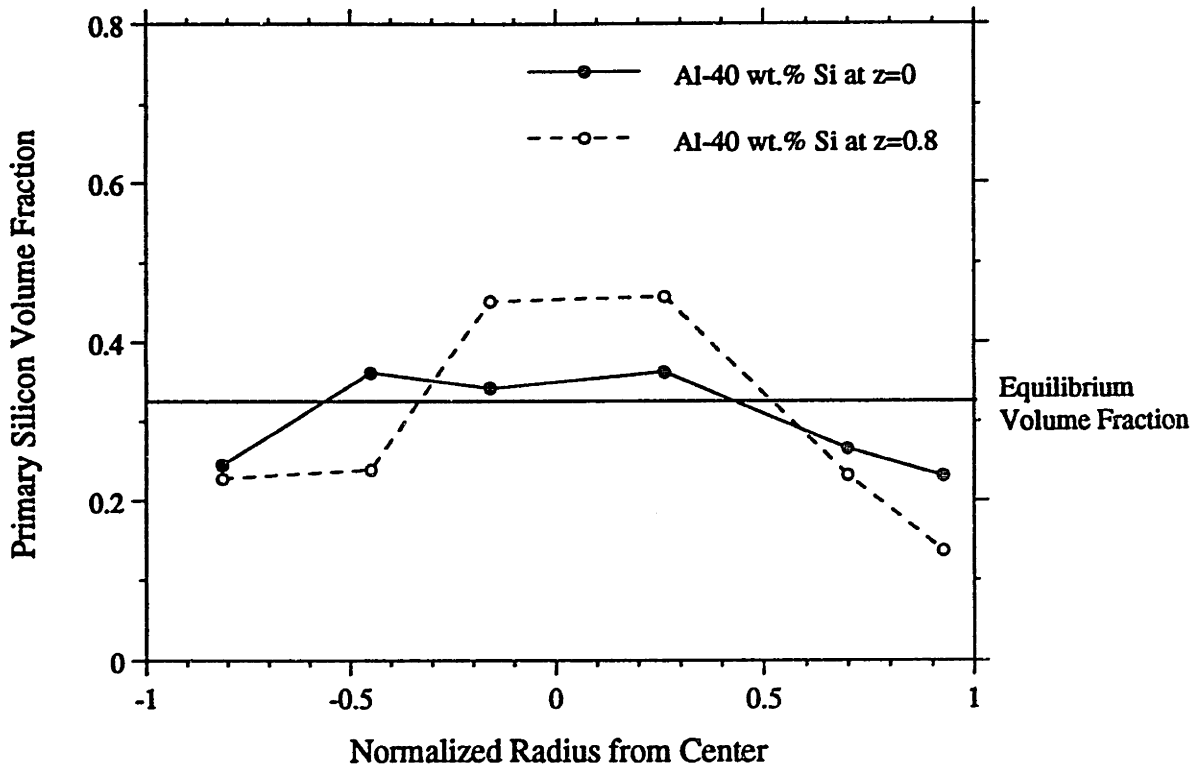

Figure 5.16 Primary silicon volume fraction versus normalized horizontal and radial distance from center. The specimen was Al-40 wt.% Si compressed under 3000 g load. The strain was -0.696.

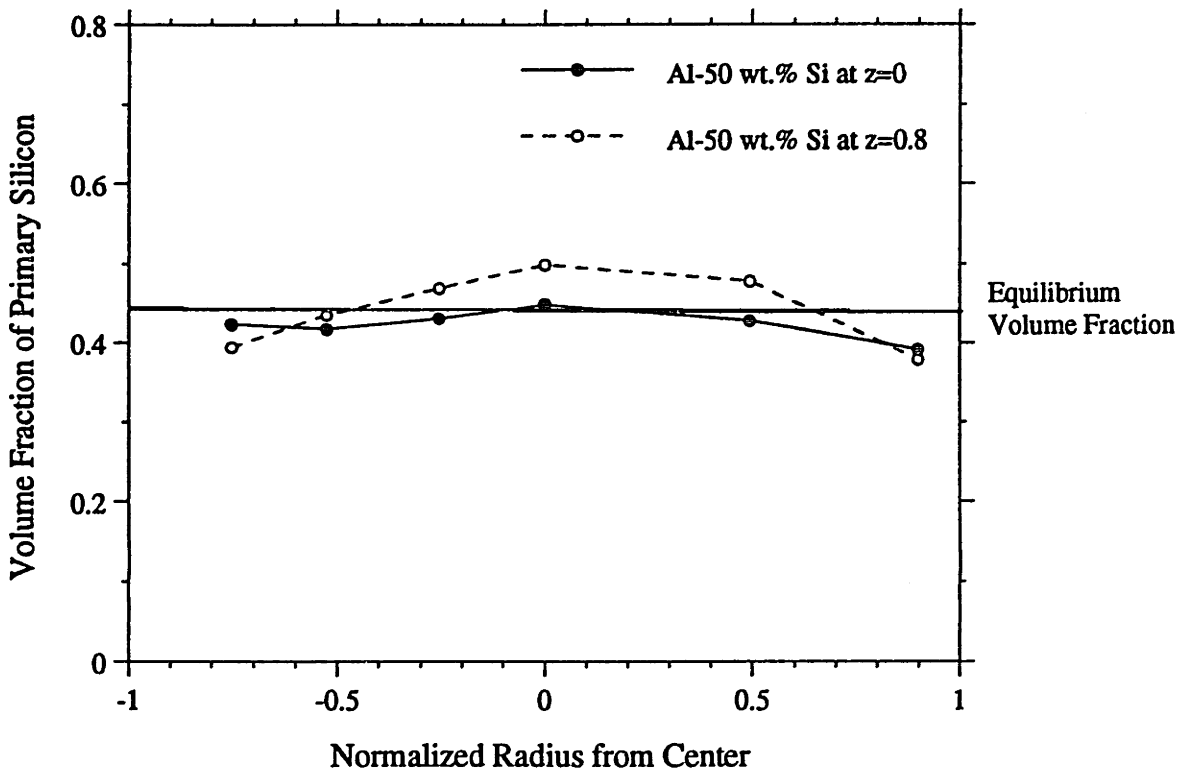

Figure 5.17 Primary silicon volume fraction versus normalized horizontal and radial distance from center. The specimen was Al-50 wt.% Si compressed under 3000 g load. The strain was -0.535.

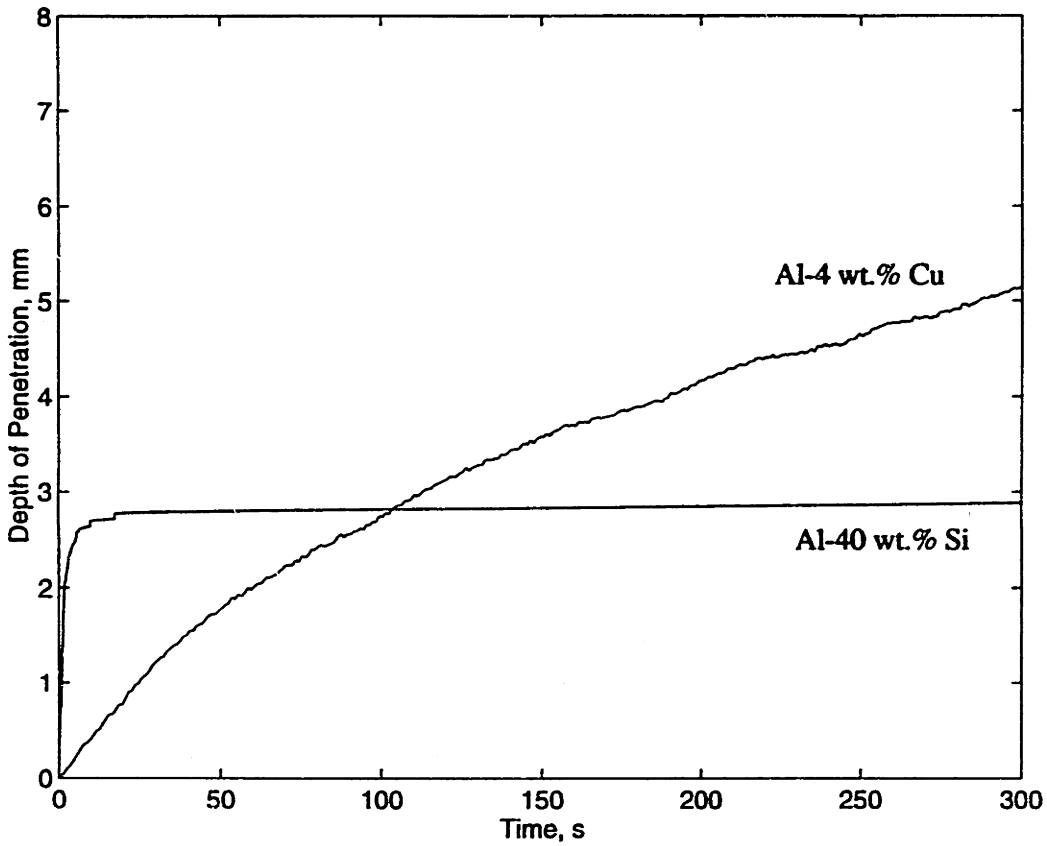

Figure 5.18 Depth of penetration during yield stress measurement by cone penetration technique versus time for Al-40 wt.% Si solidified without agitation and dendritic Al-4 wt.% Cu.

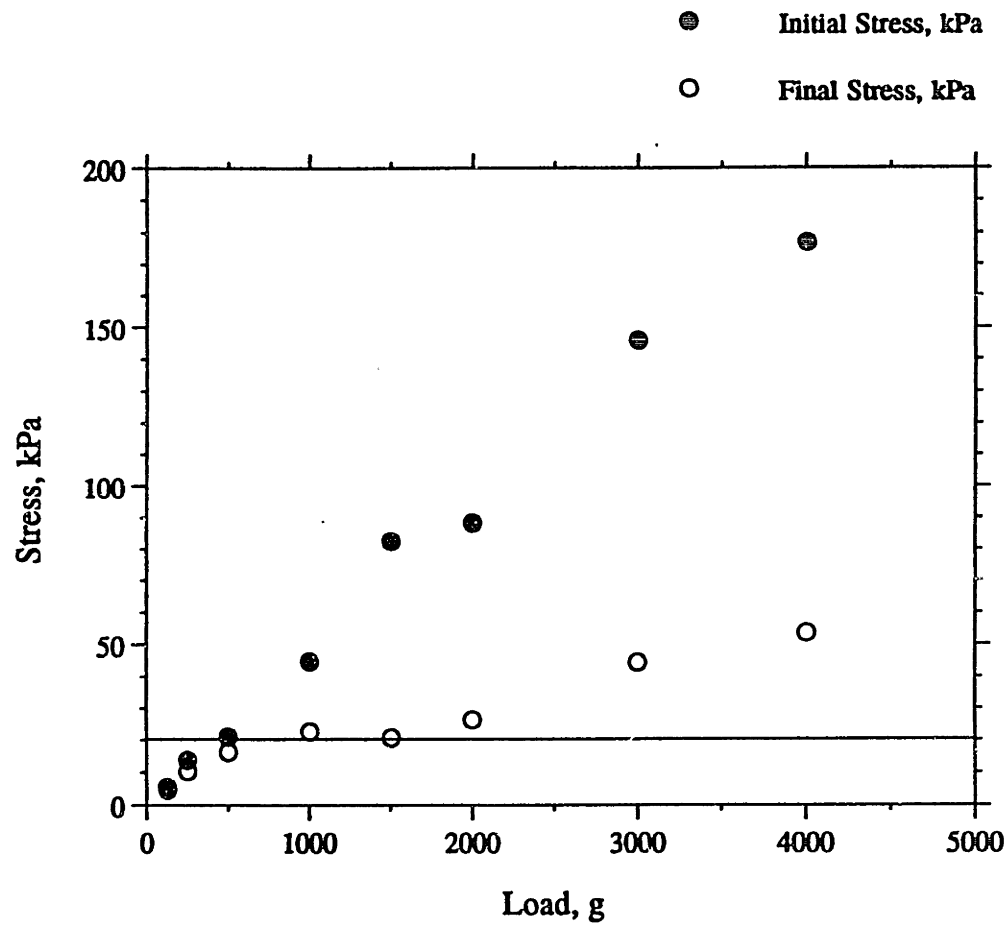

Figure 5.19 Initial and final stress versus compression load for Al-40 wt.% Si specimens.

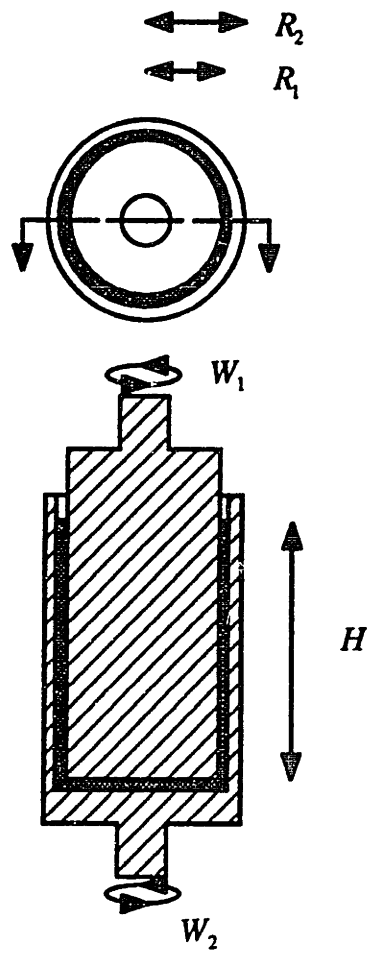

Figure A.1 Schematic representation of a concentric cylinder rheometer

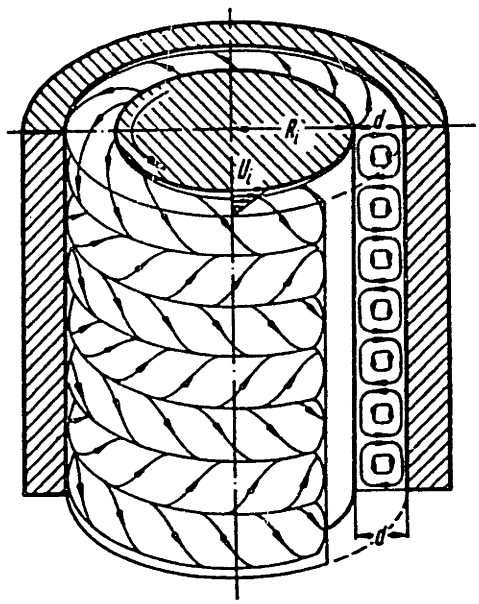

Figure A.2 Flow pattern inside rheometer indicating three dimensional velocity of the fluid

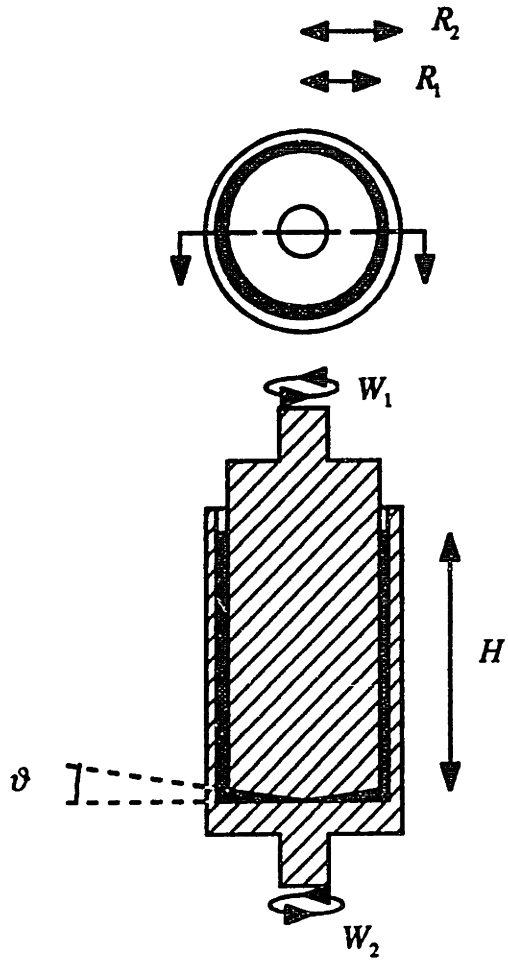

Figure A.3 Schematic representation of a concentric cylinder rheometer

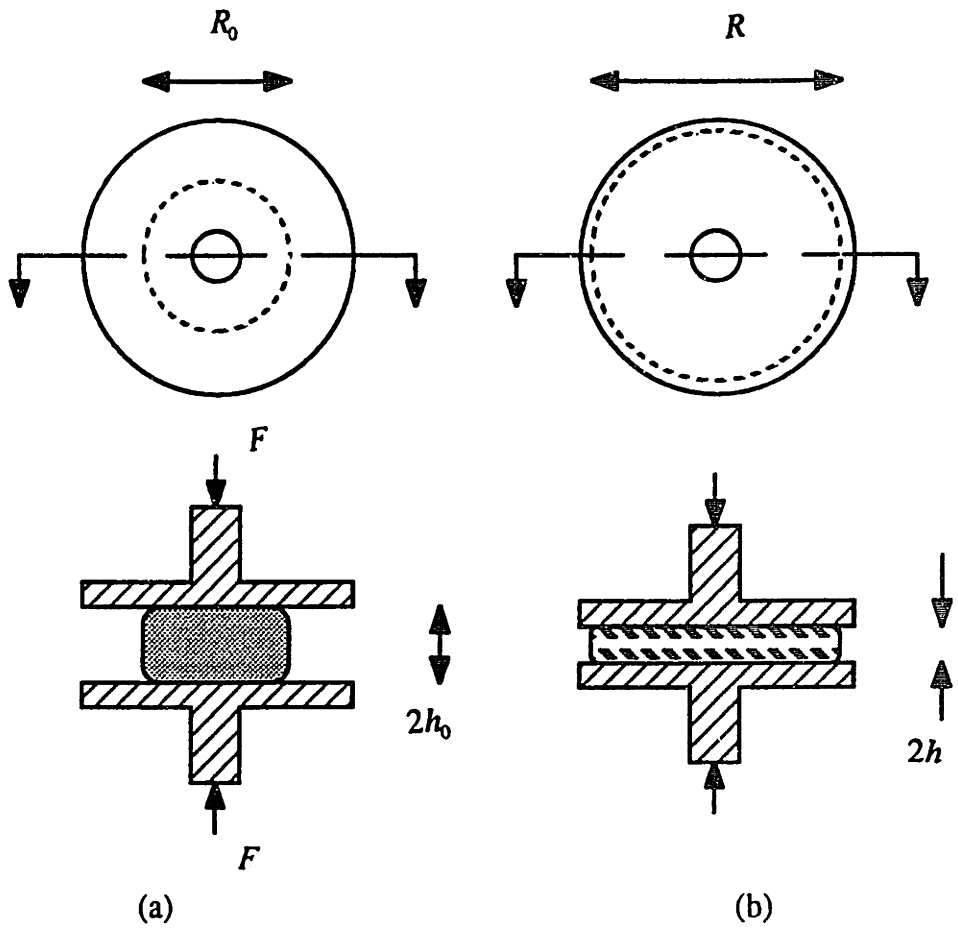

Figure A.4 Schematic representation of a compression test between two parallel plates when the specimen is smaller than the gap (a) start (b) finish

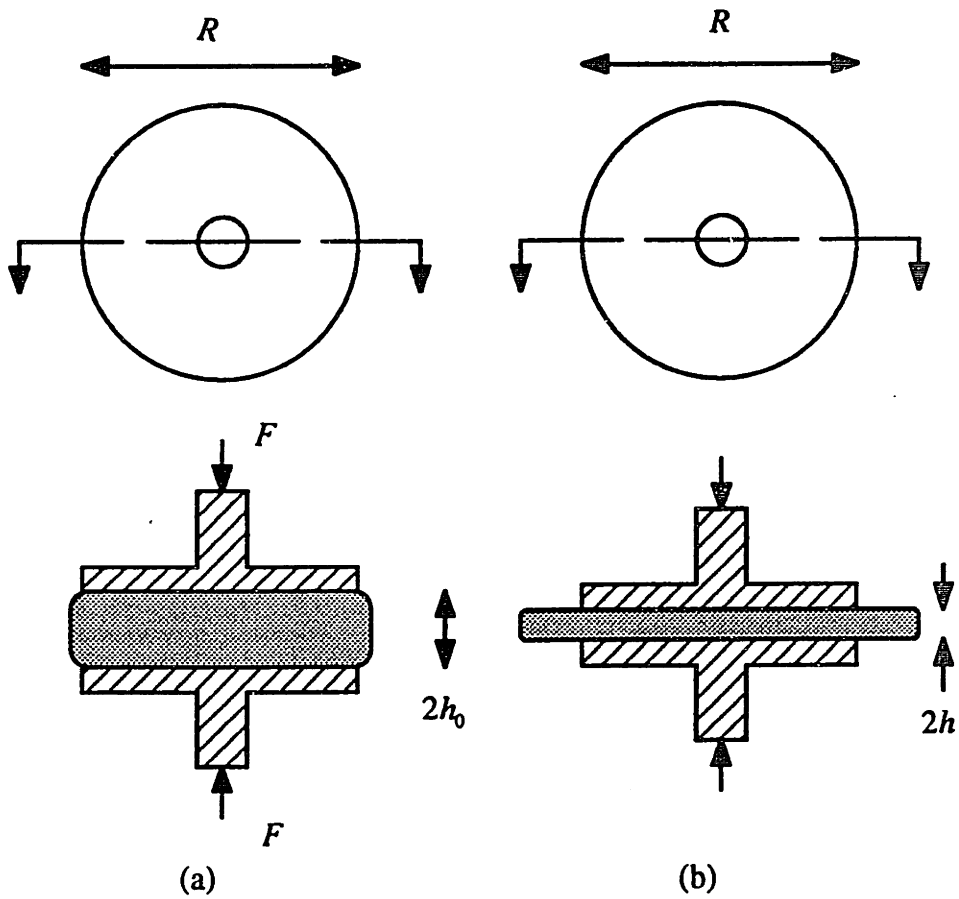

Figure A.5 Schematic representation of a compression test between two parallel plates when the specimen completely fills the gap (a) start (b) finish

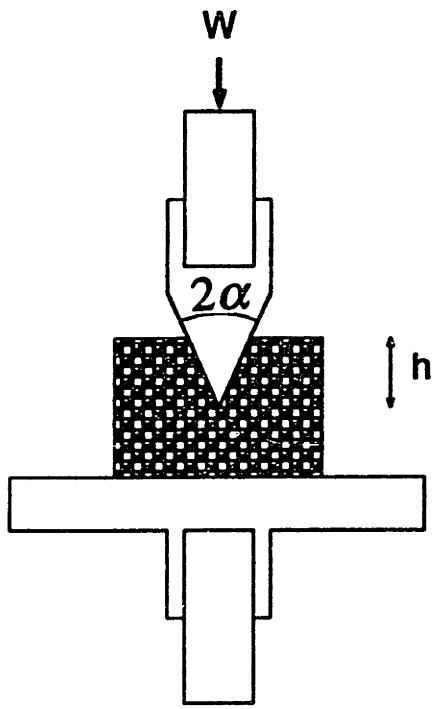

$$\tau_o = K\frac{W}{h^2}$$

$$\text{where } K = \frac{1}{\pi}\cos^2\alpha\cot\alpha$$

Figure A.6 Schematic representation of a cone penetration test

Table 2.1 The maximum packing fraction of various arrangement of mono-size spheres

Arrangement	Maximum packing fraction
Simple cubic	0.52
Minimum thermodynamically stable configuration	0.548
Hexagonally packed sheets just touching	0.605
Random close packing	0.637
Body-centered cubic packing	0.68
Face-centered cubic/ hexagonal close packed	0.74

Table 2.2 The variables which control the maximum packing fraction

Variables	Experimental observation	Theory
1. Particle		
Shape	*	**
Absolute size	*	*
Size distribution	**	**
Mass	*	*
Elasticity	**	*
Resilience	**	*
Surface properties	*	*
2. Container		
Shape	*	*
Size	**	*
Elasticity	•	•
Surface properties	•	•
3. Deposition		
Intensity of deposition	**	*
Velocity of depositing particles	**	*
Method	*	o

• no evidence
* qualitative evidence
** quantitative evidence

Table 2.3 The value of s and g_s^* for a number of suspensions of asymmetric particles, obtained by fitting experimental data to equation (2.7) (from BARNES, et al.[1981])

Systems	s	g_s^*	$s\,g_s^*$
Spheres (submicron)	2.7	0.71	1.92
Spheres (40μm)	3.28	0.61	2.00
Ground gypsum	3.25	0.69	2.24
Glass rods:			
(30×700μm)	9.25	0.268	2.48
Glass plates:			
(100×400μm)	9.87	0.382	3.77
Quartz grains:			
(53 to 76 μm)	5.8	0.371	2.15
Glass fibers:			
axial ratio 7	3.8	0.374	1.42
axial ratio14	5.03	0.26	1.31
axial ratio21	6.0	0.233	1.40

Table 2.4 Power-law constants for semi-solid metals at $g_s = 0.4$ reported by various investigators

Investigators	Alloys	n	m	Shear rate range	Condition
Lehuy 1985	Zn-27Al-2Cu	0.3	50	125 to 640	Continuous cooling at 0.05°C/min.
Taha 1987	Bi-17Sn	0.4	64	200 to 500	Continuous cooling at about 1°C/s.
Joly 1976	Sn-15Pb	0.6	9	100 to 800	Continuous cooling at about 0.41°C/s.
Kattamis 1991	Al-4.5Cu-1.5Mg	-0.2	700	80 to 600	Continuous cooling at about 0.083°C/s.
Moon 1990	Al-6.5Cu	-0.6	12000	200 to 1000	Continuous cooling at about 0.05°C/s.
Ito 1992	Al-6.5Cu	0.1	49	200 to 1000	Steady state
Kattamis 1991	Al-4.5-1.5Mg	0.1	63	5 to 350	Steady state
Kumar 1994	Al-7Si-0.6Mg	0.4	15	400 to 800	Steady state
Mori 1984	Al-5Cu	-0.8	NA	NA	Continuous cooling at cooling rates

Table 2.5 Commercial hypereutectic Al-Si alloys

Alloy Number	Si	Fe	Cu	Mn	Mg	Zn	Ti	P	Ni	Density
390	17	<1.3	4.5	<0.1	0.55	<0.1	0.2 max.	trace	...	2.74
A390	17	<0.5	4.5	<0.1	0.55	<0.1	0.2 max.	trace	...	2.74
B390	17	<1.3	4.5	<0.1	0.55	<1.5	0.2 max.	trace	0.1max.	2.74
392	19	<1.3	4.5	...	1	<0.5	...	trace	...	2.63
393	20	<1.3	0.6	...	1	...	...	trace	...	<2.62

Table 4.1 Viscosity measurements during continuous cooling of hypereutectic Al-Si alloys

Sample Number	Alloy Composition	Shear Rate, s-1
1	Al-30 wt.% Si	38
2	Al-30 wt.% Si	90
3	Al-30 wt.% Si	92
4	Al-30 wt.% Si	176
5	Al-30 wt.% Si	185
6	Al-30 wt.% Si	340
7	Al-30 wt.% Si	352
8	Al-40 wt.% Si	38
9	Al-40 wt.% Si	53
10	Al-40 wt.% Si	98
11	Al-40 wt.% Si	100
12	Al-40 wt.% Si	174
13	Al-40 wt.% Si	214
14	Al-40 wt.% Si	251
15	Al-40 wt.% Si	287
16	Al-40 wt.% Si	371
17	Al-40 wt.% Si	381
18	Al-40 wt.% Si	382
19	Al-40 wt.% Si	490
20	Al-40 wt.% Si	522
21	Al-40 wt.% Si	787
22	Al-50 wt.% Si	89
23	Al-50 wt.% Si	171
24	Al-50 wt.% Si	277
25	Al-50 wt.% Si	56
26	Al-50 wt.% Si	273
27	Al-50 wt.% Si	98
28	Al-50 wt.% Si	386
29	Al-50 wt.% Si	517
30	Al-50 wt.% Si	767
31	Al-50 wt.% Si	787

Table 4.2 Constants obtained by fitting experimental data with equation (4.7) for Al-40 wt.% Si continuously cooled at a typical solidification rate of 40°C/min.

Alloy: Al-40 wt.% Si	**Alloy: Al-50 wt.% Si**
$A' = 23.013$	$A' = 3.568$
$a = -1.045$	$a = -0.796$
$B' = -2.490$	$B' = -5.217$
$B'' = 20.580$	$B'' = 37.215$

Table 4.3 Power-law parameters of the equation, $\eta = m\dot{\gamma}^{n-1}$, for Al-40 and 50 wt.% Si continuously cooled at a typical solidification rate of 40°C/min.

Volume Fraction Solid	m	n
0.4	10400000	-1.88
0.3	250000	-1.36
0.2	6100	-0.84
0.1	150	-0.32

Volume Fraction Solid	m	n
0.3	11000	-0.79
0.2	1400	-0.54
0.1	180	-0.29

Table 5.1 Silicon particle size in rheocast specimens

Alloy Composition	Stirrer Speed (rpm)	Volume Fraction Solid when the Stirrer Stops	Silicon Particle Size (μm)
Al-30 wt.% Si	550	0.2	380±75
Al-40 wt.% Si	550	0.25	610±210
Al-50 wt.% Si	550	0.25	220±60

Table 5.2 Yield stress measurement experiment for alloys solidified without agitation

Sample Number	Alloy Comosition	Compressive Load, g
1	Al-30 wt.% Si	250
2	Al-30 wt.% Si	250
3	Al-35 wt.% Si	250
4	Al-35 wt.% Si	500
5	Al-40 wt.% Si	250
6	Al-40 wt.% Si	500
7	Al-50 wt.% Si	500
8	Al-50 wt.% Si	1500
9	Al-50 wt.% Si	2000

Table 5.3 Yield stress measurement experiments for rheocast alloys

Sample Number	Alloy Comosition	Compressive Load, g
1	Al-30 wt.% Si	250
2	Al-30 wt.% Si	250
3	Al-40 wt.% Si	250
4	Al-40 wt.% Si	500
5	Al-50 wt.% Si	250
6	Al-50 wt.% Si	500

Table 5.4 Constant-force compression between two parallel plates for alloys solidified without agitation

Sample Number	Alloy Comosition	Compressive Load, g
1	Al-30 wt.% Si	250
2	Al-30 wt.% Si	1000
3	Al-40 wt.% Si	500
4	Al-40 wt.% Si	2000
5	Al-50 wt.% Si	2000
6	Al-50 wt.% Si	4000

Specimen Number	Alloy Composition	Load, g	Initial Radius, mm	Initial Height, mm	Final Radius*, mm	Final Height, mm	Final Strain	Initial Stress, kPa	Final Stress,
1	Al-30 wt% Si	125	8.33	13.93	NA	NA	NA	5.62	NA
2	Al-30 wt.% Si	500	7.7	13.93	NA	NA	NA	26.32	NA
3	Al-30 wt.% Si	3000	7.75	13.05	NA	NA	NA	155.91	NA
4	Al-40 wt.% Si	125	8.4	13.46	9.07	11.55	-0.142	5.53	4.74
5	Al-40 wt.% Si	250	7.48	13.44	8.62	10.13	-0.247	13.95	10.5
6	Al-40 wt.% Si	500	8.6	14.58	9.75	11.33	-0.223	21.1	16.42
7	Al-40 wt.% Si	1000	8.36	14.58	11.74	7.39	-0.493	44.66	22.65
8	Al-40 wt.% Si	1500	7.53	13.39	15.01	3.37	-0.748	82.57	20.78
9	Al-40 wt.% Si	2000	8.4	13.34	15.36	3.99	-0.701	88.47	26.46
10	Al-40 wt.% Si	3000	8.01	13.92	14.53	4.23	-0.696	145.95	44.35
11	Al-40 wt.% Si	4000	8.4	13.34	15.25	4.05	-0.696	176.95	53.69
12	Al-50 wt.% Si	250	8.46	13.26	8.72	12.48	-0.059	10.9	10.26
13	Al-50 wt.% Si	1000	8.43	13.38	8.68	12.63	-0.056	43.92	41.43
14	Al-50 wt.% Si	3000	8.3	13.31	12.17	6.19	-0.535	135.93	63.22

* Final radii are calculated from final heights with an assumption of constant.

Table 5.5 Constant-force compression between two parallel plates for rheocast alloys

BIBLIOGRAPHY

A. EINSTEIN, Ann. Physik 19 (1906) 289

A. EINSTEIN, Ann. Physik 34 (1911) 591

G. I. TAYLOR, Phil. Trans., Royal Soc. London A, 223 (1923) 289

M. MOONEY, J. Rheol. 2 (1931) 210

J. R. SCOTT, Inst. Rubber Ind. Trans. 7 (1931) 169

P. A. REBINDER, Trans. Conf. Viscosity of Liquids and Colloid Solutions 361 (1941)

P. A. REBINDER, Trans. Conf. Viscosity of Liquids and Colloid Solutions 173 (1944)

I. M. KRIEGER and H. Elrod, J. Appl. Phys. 24 (1953) 134

S. THORNTON, Proc. Phy. Soc. 66B (1953) 115

I. M. KRIEGER and T. J. Dougherty, Trans. Soc. Rheol. 3 (1959) 137

H. EYRING, D. Henderson, B. J. Stover, and E. M. Eyring, Statistical Mechanics and Dynamics, Wiley, New York (1964) 460

M. M. CROSS, J. Colloid Sci. 20 (1965) 417

D. G. THOMAS, J. Colloid Sci., 20 (1965) 267

S. A. METZ and M. C. Flemings, AFS Trans 77 (1969) 329

A. CLARO F. and J. Conrads T., AFS Trans. 78 (1970) 324

S. A. METZ and M. C. Flemings, AFS Trans. 78 (1970) 453

H. M. SKELLY and C. F. Dixon, Int. J. Powder Met. 7 (1971) 47

P. J. CARREAU, Trans. Soc. Rheol. 16 (1972) 99

D. B. SPENCER, R. Mehrabian, and M. C. Flemings, Met. Trans. 3 (1972) 1925

G. A. COLLIGAN and M. A. Gunes, AFS Transactions 81 (1973) 359

P. J. LEIDER and R. B. Bird, Ind. Eng. Chem. Fundamentals 13 (1974) 336 and 342

K. KOBAYASHI, P. H. Shingu, R. Ozaki, J. Mat. Sci. 10 (1975) 290

P. A. JOLY and R. Mehrabian, J. Mat. Sci. 11 (1976) 1393

K. KOBAYASHI, P. H. Shingu, and R. Ozaki, J. Mat. Sci. 11 (1976) 399

J. M. OBLAK and W. H. Rand, Met. Trans. 7B (1976) 699

J. M. OBLAK and W. H. Rand, Met. Trans. 7B (1976) 705

R. ICHIKAWA and K. Miwa, J. Japan Inst. of Metals 42 (1978) 1023

B. D. DIXON and J. V. Parekh, J. Texture Studies 10 (1979) 421

K. KOBAYASHI and L. M. Hogan, Phil. Magazine 40A (1979) 399

H. SCHLICHTING, Boundary-Layer Theory, 7th edition, transl. by Kestin, J., McGraw-Hill (1979)

A. VOGEL, R. D. Doherty, and B. Cantor, Solidification and Casting of Metals, The Metals Society, London (1979) 479

N. APAYDIN, K. V. Prabhakar, and R. D. Doherty, Mat. Sci. Eng. 46 (1980) 145

R. BALL and P. J. Richmond, Phys. Chem. Liquids 9 (1980) 99

V. LAXMANAN and M. C. Flemings, Met. Trans. 11A (1980) 1927

H. I. LEE, R. D. Doherty, E. A. Feesr, and J. M. Titchmarsh, Proc. Conf. on Solidification Technology in the Foundry and Casthouse, Coventry, UK (1980) 119

H. A. BARNES, Dispersion Rheology: 1980, Royal Soc. of Chem., Industrial Division, London (1981)

T. MATSUMIYA and M. C. Flemings, Met. Trans. 12B (1981) 17

K. MIWA and R. Ichikawa, J. Japan Inst. of Metals 45 (1981) 853

M. KEENTOK, Rheol. Acta 21 (1982) 325

M. SUERY and M. C. Flemings, Met. Trans. 13A (1982) 1809

NGUYEN Q. D. and D. V. Boger, J. Rheol. 27 (1983) 321

O. A. ATASOY, F. Yilmaz, and R. Elliott, J. of Crystal Growth 66 (1984) 137

N. MORI, K. Ogi, and K. Matsuda, J. Japan Inst. of Metals 48 (1984) 936

J. L. MURRAY and A. J. McAlister, Bulletin of Alloy Phase Diagram 5 (1984) 74

D. A. PINSKY, P. O. Charreyon, and M. C. Flemings, Met. Trans. 15B (1984) 173

S. TAKAJO, W. A. Kaysser, and G. Petzow, Acta Met. 32 (1984) 107

H. A. BARNES and K. Walters, Rheol. Acta 24 (1985) 323

K. F. KOBAYASHI and L. M. Hogan, J. Mat. Sci. 20 (1985) 1961

H. LEHUY, J. Masounave, and J. Blain, J. Mat. Sci. 20 (1985) 105

NGUYEN Q. D. and D. V. Boger, J. Rheol. 29 (1985) 335

R. WEST and H. Fredriksson, J. Mat. Sci. 20 (1985) 1061

D. C-H. CHENG Rheol. Acta 25 (1986) 542

J. M. M. MOLENAR, L. Katgerman, W. H. Kool, and R. J. Smeulders, J. Mat. Sci. 21 (1986) 389

K. ICHIKAWA, S. Ichizuka, and Y. Kinoshita, Trans. Japan Inst. of Metals 28 (1987) 135

M. A. TAHA, N. A. El-Mahallawy, A. M. Assar, and P. R. Sahm, Solidification Processing, Sheffield (1987)

A. S. YOSHIMURA and P. K. Prud'homme, J. Rheol. 31 (1987) 699

H. A. BARNES, J. F. Hutton, and K. Walters, An Introduction to Rheology, Elsevier Science (1989)

J. P. HARNETT and R. Y. Z. Hu, J. Rheol. 33 (1989) 671

N. TENEKEDJIEV, D. Argo, and J. E. Gruzleski, AFS Trans. 18 (1989) 127

H. K. MOON, PhD Thesis, MIT, (1990)

J. SCHURZ, Rheol. Acta 29 (1990) 170

G. WAN and P. R. Sahm, Acta Met. 38 (1990) 967

G. WAN and P. R. Sahm, Acta Met. 38 (1990) 2367

M. C. FLEMINGS, Met. Trans. 22A (1991) 957

J. FERGUSON, Applied Fluid Rheology, Elsevier Applied Science, London, 1991

T. Z. KATTAMIS and T. J. Piccone, Mat. Sci. Eng. A131 (1991) 265

P. MANDAL, A. Saha, and M. Chakraborty, AFS Trans. 10 (1991) 643

L. QINGCHUN, C. Kuiying, L. Chi, Z. Songyan, AFS Trans. 85 (1991) 245

L. S. TURNG and K. K. Wang, J. Mat. Sci. 26 (1991) 2173

A. AHMED and A. N. Alexandrou, Proc. Symp. Nature and Properties of Semi-Solid Materials, TMS, Warrendale, USA, edited by J. A. Sekhar and J. A. Dantzig (1992)

S. B. BROWN, P. Kumar, and C. L. Martin, Proc. Conf. Processing of Semi-Solid Alloys and Composites, edited by Brown, S. B. and Flemings, M. C., MIT (1992) 183

N. G. HENDERSON, A. R. A. McLelland, H. V. Atkinson and D. H. Kirkwood, Proc. Conf. Processing of Semi-Solid Alloys and Composites, edited by Brown, S. B. and Flemings, M. C., MIT (1992) 349

Y. ITO, M. C. Flemings, and J. A. Cornie, Proc. Symp. Nature and Properties of Semi-Solid Materials, TMS, Warrendale, USA, edited by J. A. Sekhar and J. A. Dantzig (1992) 1

S. JABRANE, B. Clément, and F. Ajersch, Proc. Conf. Processing of Semi-Solid Alloys and Composites, edited by S. B. Brown and M. C. Flemings, MIT (1992) 223

M. KIUCHI and S. Sugiyama, Proc. Conf. Processing of Semi-Solid Alloys and Composites, edited by S. B. Brown and M. C. Flemings, MIT (1992) 47

NGUYEN Q. D. and D. V. Boger, Ann Rev. Fluids Mech. 24 (1992) 47

T. OHMI, Y. Tanaka, and M. Kudoh, J. Japan Inst. of Metals 56 (1992) 96

T. OHMI, M. Kudoh, and K. Ohsasa, J. Japan Inst. of Metals 56 (1992), 1064

D. M. SMITH, J. A. Eady, L. M. Hogan, and D. W. Irwin, Met Trans. 22A (1991) 575

P. J. WARD, H. V. Atkinson, D. H. Kirkwood, and C. M. Sellars, Proc. Conf. Processing of Semi-Solid Alloys and Composites, edited by Brown, S. B. and Flemings, M. C., MIT (1992) 440

P. KUMAR, PhD Thesis, MIT (1994)

T. OHMI, K. Minoguchi, M. Kudoh, Y. Itoh, and K. Matsuura, J. Japan Inst. of Metals 58 (1994) 1311

T. OHMI, K. Minoguchi, M. Kudoh, Y. Itoh, K. Matsuura, and K. Ishii, J. Japan Inst. of Metals 58 (1994) 324

S. SANNES, H. Gjestland, L. Arnberg, and J. K. Solberg, Proc. Conf. Processing of Semi-Solid Alloys and Composites, edited by M. Kiuchi, Tokyo (1994) 271

G. ARAKANE, S. Takamori, Y. Ohsawa, and A. Sato, J. Japan Inst. of Metals 59 (1995) 559

J.-P. PARK, K. Sassa, and S. Asai, J. Japan Inst. of Metals 59 (1995) 733